CHAPTER 2

Quantitative single particle analysis

Having introduced some trends and evolutions in instrumentation for single particle analysis, it seems appropriate to start dealing now with the main goal of the fundamental research carried out for this Ph.D. dissertation. A short introduction will give a review of the different methods used for quantitative X-ray analysis, especially for single particle analysis. Monte Carlo simulations will be dealt with in more detail, since the presented research used this kind of calculations for quantitative analysis in an iterative approach, which will be explained afterwards. In the final paragraph, the optimisation and testing of the quantification procedure will be discussed.

Table of Contents

1. Introduction

Many methods for quantitative analysis are based on the (linear) proportionality between the measured signal (I_i) and the concentration of the analysed samples (Ci), so empirical calibration curves can often be used quite easily to determine unknown concentrations, based on standard measurements.

$$I_i = \text{constant} \cdot C_i$$

However, quantitative X-ray analysis is not as straightforward, since several matrix effects affect the proportional relationship between standard and unknowns.

$$\left.\begin{aligned} I_1 &= \text{constant}_1 \cdot C_1 \\ I_2 &= \text{constant}_2 \cdot C_2 \\ &\ldots \\ I_i &= \text{constant}_i \cdot C_i \end{aligned}\right\} \quad \text{constant}_1 \neq \text{constant}_2 \neq \ldots \neq \text{constant}_i$$

Over the past fifty years, different methods have been developed to correct for these effects, either based on standard analysis or on standardless analysis (using fundamental parameters). In the discussion below, different methods will be described briefly, as well as their use in single particle analysis.

1.1 Classical corrections methods for bulk samples

A milestone in the field of electron microscopy was the thesis of R. Castaign, published in 1951, which covered all aspects of quantitative X-ray analysis by electron microscopy.[1,2,3] Castaign's approach to the quantification problem was revolutionary, and it still has a large impact on the way scientists think about X-ray analysis nowadays. His approach was based on a clear model for the physical processes involved in the diffuse penetration of electrons and the emission and absorption of X-rays in bulk samples, leading to *ZAF*-corrections and $\phi(\rho z)$ methods.[3,4,5,6,7,8,9]

- **Standard *ZAF* corrections**

Standard *ZAF* corrections try to re-obtain proportionality between the signals (characteristic X-ray intensities) for the analysed samples and bulk standards, by correcting for the matrix differences between them. So-called k-ratios take into account the atomic number, the absorption and the fluorescence matrix effects.

$$\left.\begin{aligned} C_i^{\text{unknown}} &\approx I_i^{\text{unknown}} \\ C_i^{\text{standard}} &\approx I_i^{\text{standard}} \end{aligned}\right\} \quad \frac{C_i^{\text{unknown}}}{C_i^{\text{standard}}} \approx \frac{I_i^{\text{unknown}}}{I_i^{\text{standard}}} = k_i$$

$$C_i^{\text{unknown}} = C_i^{\text{standard}} \cdot \frac{I_i^{\text{unknown}}}{I_i^{\text{standard}}} \cdot \frac{Z_i^{\text{unknown}}}{Z_i^{\text{standard}}} \cdot \frac{A_i^{\text{unknown}}}{A_i^{\text{standard}}} \cdot \frac{F_i^{\text{unknown}}}{F_i^{\text{standard}}}$$

$$= C_i^{\text{standard}} \cdot k_i \cdot k_i^Z \cdot k_i^A \cdot k_i^F$$

Figure 1 below schematically shows the escape volumes for the interaction phenomena, and could be helpful for understanding the discussion of the matrix influences below. The formula and expressions are given for bulk samples only, which means that the analyzed specimen are homogeneous, flat, polished and infinitely large in all directions (in real life this means the sample size should be at least 15 μm in all directions).

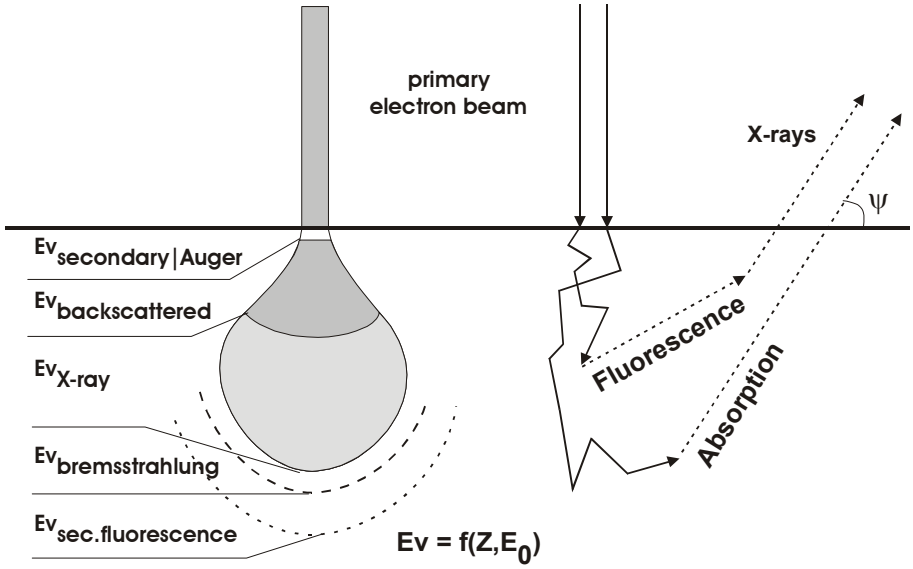

Figure 1: Interaction escape volumes (Ev) and matrix influences

The *first* k-ratio k^Z_i is related to the difference in the efficiency of X-ray production by the various elements of the standard and the unknown. A specimen consisting of mainly high-*Z* elements will show more electron backscattering compared to a low-*Z* sample, which implies that a large fraction of electrons will escape the sample before causing X-ray generation. Electrons that do propagate in the specimen will also have higher probability to travel deeper inside a low-*Z* specimen due to its lower stopping power (*S*), which is the rate of energy loss along the electron trajectory. Therefore, the electron path or trajectory is dependent on the composition of the specimen, and therefore, the atomic number *Z* determines the size of the different escape volumes. The general expression for the atomic number ratio is:

$$k_i^Z = \frac{Z_i^{\text{unknown}}}{Z_i^{\text{standard}}}$$

in which Z_i is the atomic number factor that can be expressed as:

$$Z_i = \frac{I^{\text{NO R-INFLUENCE}}}{I^{\text{R-INFLUENCE}}} \cdot \frac{I^{\text{NO S-INFLUENCE}}}{I^{\text{S-INFLUENCE}}} = \frac{1}{R_i} \cdot \left[\frac{1}{\int_{E_c \to E_0} \frac{Q_i}{S_i} \cdot dE} \right]$$

in which R_i stands for the backscattering factor, the bracketed factor is related to the stopping power S_i, Q_i is the ionization cross section (the probability function for characteristic X-ray generation of element *i*), E_0 is de incident or primary electron energy, and E_c is the critical excitation energy for characteristic X-rays of element *i*. In order to avoid complicated integral calculations, the formula above was further simplified for bulk samples, based on several approximations and on empirical expressions for R_i and S_i.

The *second* k-ratio $k^A{}_i$ is related to the difference in the absorption for X-rays. Once an electron has entered the sample and comes to a point where it transfers all of its energy to cause inner shell ionisation, the depth of the electron and the shape of the specimen will determine the absorption of the generated X-ray. The deeper the X-ray is generated, the longer the path it has to travel through the sample, the higher the absorption probability. The ratio can be expressed as:

$$k_i^A = \frac{A_i^{\text{unknown}}}{A_i^{\text{standard}}}$$

in which A_i stands for the absorption factor:

$$A_i = \frac{I^{\text{NO ABSORPTION}}}{I^{\text{ABSORPTION}}} = \frac{\int_{0\to\infty} \phi(\rho z)\cdot d(\rho z)}{\int_{0\to\infty} \phi(\rho z)\cdot e^{-\left(\frac{\mu}{\rho}\cdot(\rho z)\cdot\csc(\psi)\right)}\cdot d(\rho z)}$$

in which ψ is the take-off or exit angle of the X-ray detector; μ/ρ is the mass absorption coefficient (a measure for the absorption capacity of the specimen); $\phi(\rho z)$ stands for the distribution of characteristic X-rays as a function of depth in the sample. Again many empirical expressions of the formula above have simplified the calculations of the absorption corrections for bulk samples, based on approximations and parameterisations. Depth in the specimen is expressed as ρz, the so-called mass depth (depth z multiplied with density ρ). Mass depths are commonly used, in order to mask the effect of specimen depth when comparing specimen of different atomic number. It should be mentioned that one of the critical parameters (in any of the quantification procedures described in this work) is the density of the sample. Since the composition of the sample is unknown, its density is also unknown and should be estimated as well.

The *third* k-ratio $k^F{}_i$ takes into account the difference in X-ray generation by fluorescence. When an X-ray is generated for an element, it has to travel through the specimen. On its journey, it could also cause the generation of an X-ray from another element (so-called fluorescence), if its energy is higher than the critical excitation energy for the other element, and if the difference between both energies is smaller than 5 keV. The expression for the fluorescence ratio is:

$$k_i^F = \frac{F_i^{\text{unknown}}}{F_i^{\text{standard}}}$$

in which F_i is the fluorescence factor, known as:

$$F_i = \frac{I^{\text{NO FLUORESCENCE}}}{I^{\text{FLUORESCENCE}}} = \frac{1}{1+\sum_j \left(\frac{I_j^f}{I_i}\right)_j}$$

in which I^f_j / I_i relates the intensity of radiation from element j produced by fluorescence of element i. The summation over j is required to obtain the total correction over all of the elements in the specimen. Again, many expressions for this formula have been developed to simplify the calculation work for this correction. It should be noticed that the formula above only involves excitation by characteristic X-rays, but bremsstrahlung could also cause secondary fluorescence. The calculations for this correction are, however, quite complicated due to the required integration over a large energy range, and only few papers appeared in literature on this subject.[6]

The quantification procedure to determine the elemental concentrations within a specimen is an iterative process of reverse calculations. After carrying out the analysis (under identical measurement conditions), the ratio of the intensities for the standards and the unknowns are first determined. An initial set of concentrations is then calculated by normalization of the intensity ratios. The next step is to apply the different corrections to these initial ratios, resulting in new estimates that are evaluated as part of an iteration procedure (the calculated ratios are compared to the ratio of the measured values). A new set of normalized concentrations can be calculated in order to continue the reverse calculations until convergence occurs (within preset limits). It should be noticed that by using ratios, the influence of instrumental parameters (detector efficiency) on the intensities are cancelled out, and should therefore no longer be taken into account.

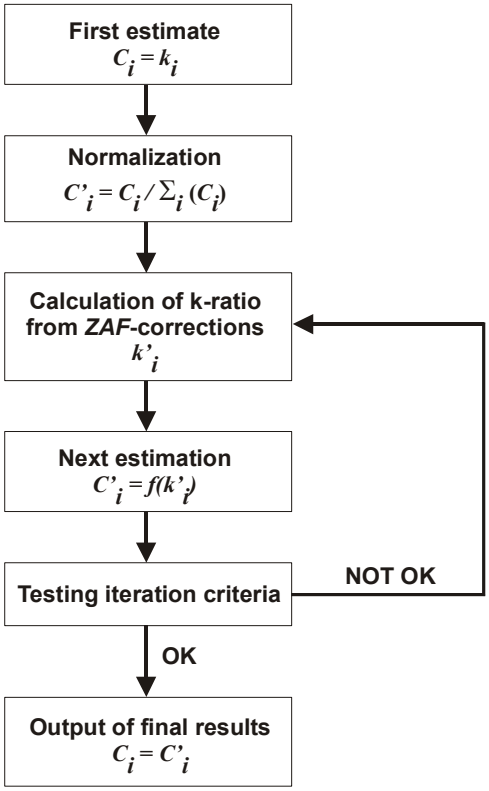

Figure 2: General flowchart for typical *ZAF*-correction methods

It is important to mention that, before the use of windowless EPMA or TW-EPMA, the intensities of low-*Z* elements like carbon, nitrogen or oxygen remained unknown, and could therefore not be taken into account in the calculations. Concentrations for these elements could only be calculated from known stoichiometry.

- **$\phi(\rho z)$ methods**

As stated above, the expressions for the standard *ZAF* corrections could be simplified and parameterized in order to fasten the involved calculations.[10,11,12,13,14,15] The most critical parameterization and simplification could be found in the absorption correction, where the integration of the $\phi(\rho z)$ function was replaced by very simple expressions as a function of the path length, the initial and critical energy, and the average atomic number and mass. This parameterisation tried to account for the shape of the $\phi(\rho z)$ curve, and although the shape was not always correct, this method showed satisfying results for higher-energy X-rays due to the relatively long absorption path lengths.

However, when dealing with low-energy X-rays, the shape of the $\phi(\rho z)$ curve became more critical and large errors were generated. Therefore, many scientists made experimental measurements of the X-ray depth distribution functions in different types of samples, and they tried to develop specific functions for integrating or fitting their shape. In these experiments, $\phi(\rho z)$ refers to the depth distribution of X-rays in a bulk sample, normalized to the X-ray intensity produced in an infinitely thin, "unsupported" film of the same composition. Castaign and Descamps developed an experimental method to measure the X-ray distribution in a bulk specimen at different depths, in which a sample is subsequently coated with thin layers after every X-ray measurement (see Figure 3).[1]

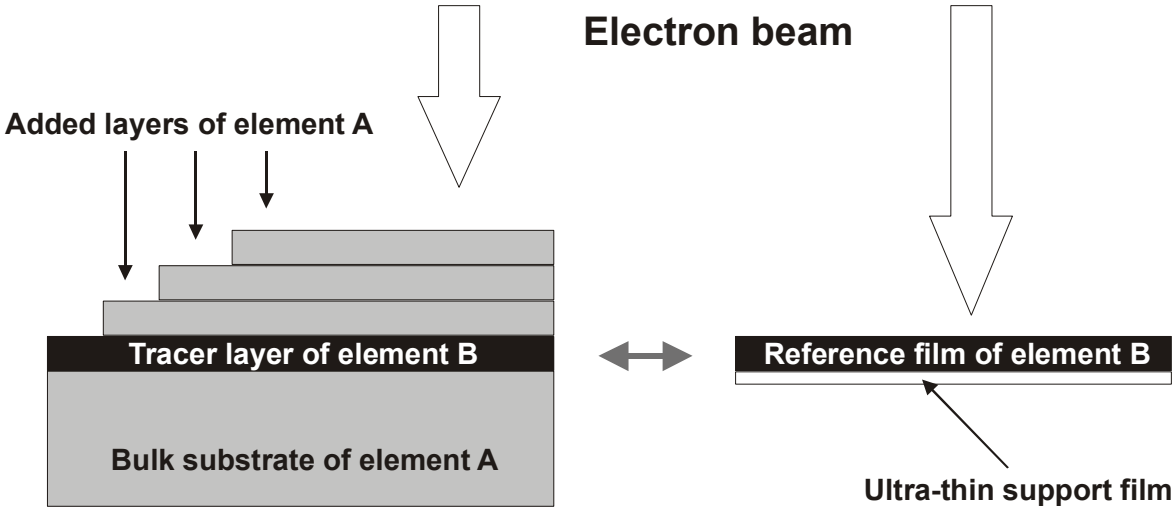

Figure 3: Experiment to determine $\phi(\rho z)$ curves

The increased knowledge of the behaviour of these curves for different materials allowed to empirically develop corrections based on the integration of $\phi(\rho z)$ curves. The critical point is still the derivation of an accurate expression for the experimental $\phi(\rho z)$ curves, which can be used in combined atomic number and absorption corrections. This combined approach could be very risky, since the thickness of the reference or tracer films should be known very accurately in the experiments in view of the atomic number correction.[3,6] Therefore, some procedures prefer to use the shape of the $\phi(\rho z)$ curve only for the absorption correction, while separate expressions are applied for the atomic number and fluorescence corrections. For low-energy X-rays, this method proved to be much more accurate than the classical *ZAF* corrections.

- **Standardless corrections**

An increasing trend in performing quantitative analysis has been the use of standardless methods instead of the traditional approach of measuring standards under identical conditions as measuring the samples.[3,16]
In so-called "true standardless" methods, standard intensities are calculated from first principles, considering all aspects of X-ray generation, propagation through the specimen and detection. A general expression for these calculations can be given as:

$$I^{\text{standard}} = \left[\frac{\rho \cdot N_A}{A} \cdot \omega \cdot \int_{E_0}^{E_c} \frac{Q}{S} \cdot dE \right] \cdot R \cdot f(\psi) \cdot \varepsilon$$

in which the bracketed term represents the excitation function (ρ and A are the density and atomic weight respectively; ω is the fluorescence yield; and N_A is Avogadro's number); R is the backscattering factor, $f(\psi)$ represents the self-absorption factor of X-rays propagating through the specimen and ε is the detector efficiency. Normalization is used to bring the total concentration of all standards to 100%.
"Fitted standard" methods are based on deriving standard intensities from a suite of experimental measurements performed remotely and adjusted for the characteristics of the local instrument that was used to measure the unknowns.
In order to be accurate, these standardless methods require precise knowledge of the occurring interaction processes, the instrumental parameters and the measurement conditions, especially in case of "true standardless" analysis.

1.2 Modified correction methods for single particle analysis

The aforementioned correction methods were developed for the analysis of bulk samples. However, quantification could get more complicated when dealing with samples of different geometry, especially in case of single particles.[8]

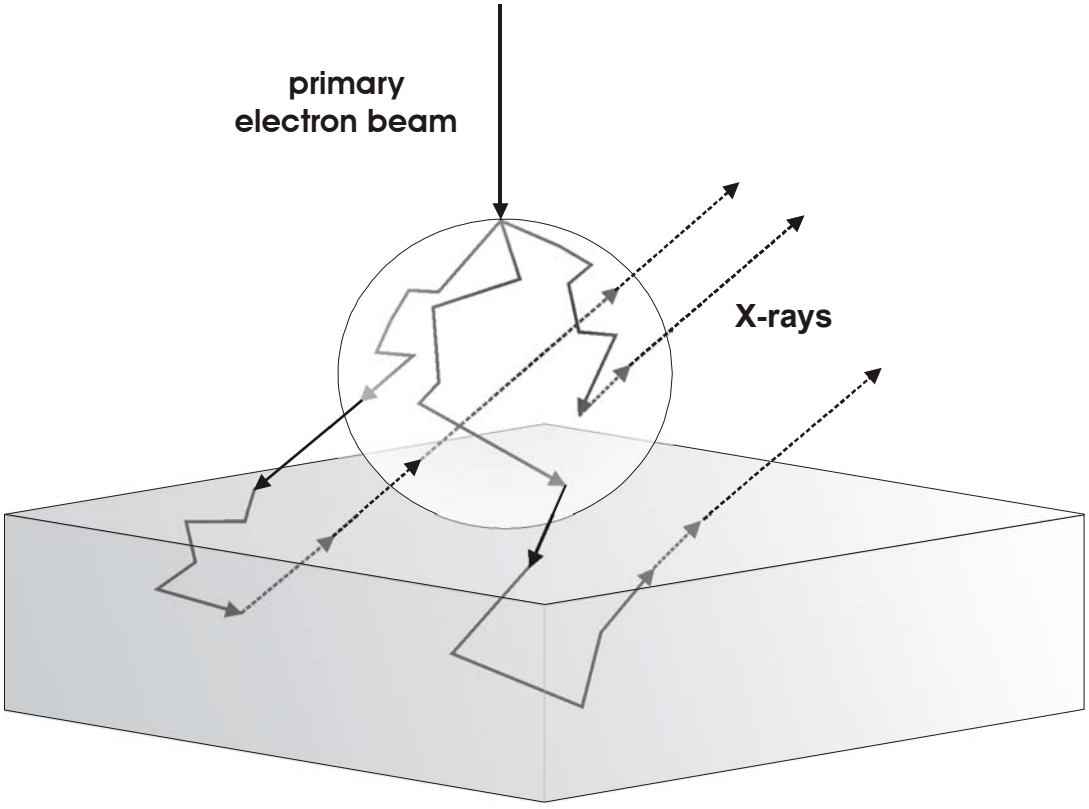

Figure 4: Electron beam analysis of an individual particle

Figure 4 shows the influence of geometry in case of the analysis of a particle mounted on a substrate. First of all, it is clear that when analysing the particle, X-rays can be generated in the substrate as well, which makes spectrum interpretation difficult. Secondly, the trajectories of the electrons in the particle and the substrate are much more complicated than in a bulk sample. A bulk sample is infinitely large in all directions and, therefore, only the z-direction (depth) is important. When the sample has more complex boundaries, the x- and y –directions should also be taken into account.

Figure 5 shows that the particle geometry has a huge impact on the *ZAF* correction factors, besides the fact that also a substrate is involved now.
When the particle dimensions approach those of the interaction volume of a bulk sample with the same composition, electrons have higher probability to escape from the sides and the bottom of the particle. In this case, escaping electrons carry their energy to the substrate, while otherwise they could have contributed to the generation of X-rays inside the particle volume. This so-called mass effect always leads to a lower intensity measured in the particle, compared to the bulk standards.
The absorption path length is dependent on the geometry as well, and this in two ways. First of all, the placement of the electron beam on the particle surface, relative to the detector position, could have a big influence on the distance to be travelled by the generated X-rays. Secondly, the morphology of the particle surface to be crossed by the X-rays also determines the absorption effects. This effect is more complex than the mass effect, since it could lead to both increased or decreased X-ray emission relative to that of a bulk standard.
Since the fluorescence generation volume is even larger than the electron excitation volume, the fluorescence effect obtained from small particles is expected to be much smaller, compared to that from bulk standards. In *ZAF* methods for bulk samples using bulk standards, the continuum fluorescence correction can often be ignored, since the effects are similar for both samples and standards and they can be cancelled out; the characteristic fluorescence is only significant if the higher-energy characteristic X-rays have energies no greater than 5 keV above the edge in question, because the efficiency of ionisation falls off rapidly as the photon energy increases above the ionisation energy. When considering small particle samples, the fluorescence radiation is almost completely lost compared to the bulk standards. For example, if the interaction volume in a hemispherical particle has a radius R_e of 1 µm, and the range for the generation of X-rays and subsequent fluorescence R_x is about 10 µm, the volume ratio of X-ray to electron production (R^3_x/R^3_e) is 1000:1 (bulk:particle). This means that only 0.1% of the bulk fluorescence is obtained in the particle, and therefore, the fluorescence effect tends to decrease the emission of characteristic X-rays compared to a bulk target.

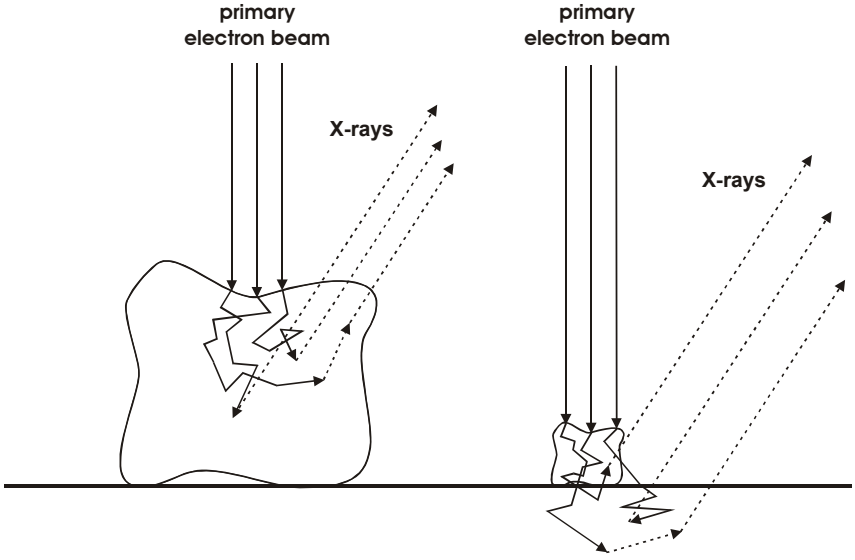

Figure 5: The effect of particle size on the correction factors

Therefore, the quantification procedures are bound to become much more complicated, and it seems almost impossible to take into account all possible effects in case of particle samples. Some possibilities exist to modify the classical quantification methods in order to deal with the complex analysis of single particles in a more simplified way.

- **Particle standards**

Similar to the classical procedure for bulk samples, some researchers tried to develop *ZAF* methods based on measurements of pure-element standards with similar particle geometry as the samples. However, since it is impossible to generate standard particles for all different elements with all kinds of shapes and sizes, this possibility is ruled out. Some analysts have used the method, but in order to estimate the magnitude of errors (due to size and shape differences), it is necessary to analyse several series of standard particles or other sets of particle standards.

- **Conventional *ZAF* and normalization factors**

Some analysts have applied classical *ZAF* corrections for particle analysis using bulk standards, ignoring the geometric differences with the particulate samples. Depending on the mass-thickness, this leads to raw concentrations that can deviate by a factor 10 or more from the true concentrations of the elements in the particle. Of course, it is impossible to compare the results for different particles in this way.
However, one could normalize the results by dividing each raw concentration with the so-called normalization factor, which is the sum of all raw concentrations (including any constituents calculated by assumed stoichiometry). The normalization factor is then considered to be a measure for the severity of the geometric effects; the larger the factor, the more likely the existence of significant errors in the normalized concentrations.

$$Normalization\ \ factor = \frac{1}{\sum_i C_i}$$

Of course, this method is only applicable to *ZAF* or $\phi(\rho z)$ methods that do not automatically force a normalization of the results, as "standardless" analysis does. Normalization is most effective in the size range below 3 μm (in case of a 20-keV beam), but it leads to inadequate, and possibly misleading results when the particle constituents and size are such that the mass effect influences the hard X-ray energies, while the absorption effect dominates the low-energy lines (resulting in severe over- and underestimations of elemental concentrations).

- **P/B ratios**

The "peak-to-background" method is based on the observation that the ratio between the intensities of characteristic and continuum X-rays *of the same energy* is much less sensitive to geometric effects. Both types of radiation are produced by different processes (inner-shell ionisation versus deceleration in a Coulombic field), but in nearly the same volume, which results in a similar scaling with the geometric mass effect (*Z*). Since both have a similar (though not identical) depth distribution, the absorption paths are also similar. By definition the energy for each radiation type is equal, so the scaling of the geometric absorption effect (*A*) must be similar as well. Therefore, the continuum intensity can be used as an automatic internal normalization factor for geometric effects, which leads to the following expression:

$$\frac{I_P^{particle}}{I_B^{particle}} = \frac{I_P^{bulk}}{I_B^{bulk}}$$

in which indices *P* and *B* denote peak and background intensities respectively; indices *particle* and *bulk* denote the different geometry for the sample and a standard respectively.

Particle intensities could be modified by the following expression, as if they were coming from a bulk sample with corresponding composition:

$$\left[I_P^{particle}\right] = I_P^{bulk} = I_P^{particle} \cdot \frac{\left[I_B^{particle}\right]}{I_B^{particle}}$$

The peak and background intensity for the particle can be determined from the measured particle spectra; however, the value for the modified background intensity is more difficult to obtain. However, Small et al. [9] have created a *ZAF* correction scheme for P/B ratios:

$$k = \frac{\left[I_P^{particle}\right]}{I_P^{bulk}} = \frac{\left[I_P^{particle}\right]}{I_P^{bulk}} \cdot \frac{\left[I_B^{particle}\right]}{\left[I_B^{particle}\right]} = \frac{I_P^{particle}}{I_B^{particle}} \cdot \frac{\left[I_B^{particle}\right]}{I_B^{bulk}}$$

The k-ratios offer an estimate of the concentration for each element *i*, from which the required modified background intensity could be calculated using pure-element bulk standards:

$$C_i = \frac{k_i}{\sum_i k_i}$$

$$\left[I_B^{particle}\right] = \sum_i C_i \cdot I_B^{\text{standard } i}$$

Some examples of P/B developments and applications for particle analysis can be found in literature.[17,18,19] The P/B method is known to result in satisfactory results, especially in case of particles with extreme geometric conditions for which simple normalization produces unacceptably large errors. The method appears to deal efficiently with the absorption effect, especially when the particle is in the size range where it plays a significant role. The biggest advantages of the procedure are probably that it is easy to calculate, and it is independent from the particle size and shape (so the analyst does not need to judge on these parameters).

However, P/B corrections have some drawbacks. First of all, it might be wrong to assume that the spatial distribution of X-ray generation is similar for peaks and backgrounds. Since different processes are involved, there is no reason why the lateral and depth distributions should be equal. Not enough research has been done to prove this basic assumption. Secondly, it is especially important that the particle spectrum does not contain large contributions from the substrate. Moreover, for the method to be correct, the background must come completely from the particle and none from the substrate, which is a condition that seems impossible to meet. Even in case of substrates with low background spectra (e.g. beryllium), there will be a particle size for which the beam penetration through the particle becomes sufficiently large that the spectral background is dominated by the contribution from the substrate. Thirdly, P/B ratios largely depend on the counting statistics and the evaluation procedure for the spectra, because the background and peak intensities should be determined quite accurately. Especially, the poor precision in determining the background measurements influences the analytical results. The bremsstrahlung background in an EDS spectrum should be truly due to continuum X-rays alone and not to artefacts produced by pulse pile-up, incomplete charge collection, etc.

- **Particle *ZAF***

As explained above, the exact elaboration of correction procedures for the analysis of particles becomes more complicated, because of the increased dimensionality of the mathematical problems. Therefore, the formulae for the applied corrections should be interpreted more strictly. Armstrong and Buseck adapted and simplified the exact mathematical expressions of the classical *ZAF* corrections for the analysis of particle samples, after which Armstrong developed a package of correction programs (CIT-ZAF) for quantitative analysis.[8,20,21,22] For example, the general expression for the calculation of the characteristic intensity of the *k* line intensity of element *A* after fluorescence by the *j* lines of elements *B* could be written as:

$$I_{f,A,k} = C_A \cdot \frac{r_A^k - 1}{r_A^k} \cdot \omega_A^k \cdot p_A^k \cdot \frac{\Delta\Omega}{4\pi} \cdot \sum_B \sum_j I_{B,j} \cdot \mu_{B,A}^j$$
$$\times \int_{\rho z=0}^{T} \frac{1}{a_0} \int_{y=\alpha_1(\rho z)}^{\alpha_2(\rho z)} \int_{x=\beta_1(\rho y,\rho z)}^{\beta_2(\rho y,\rho z)} \int_{\xi=0}^{2\pi} \int_{\theta=0}^{\pi} \int_{s=\nu_1(\rho z,\rho y,\rho x,\xi,\theta)}^{\nu_2(\rho z,\rho y,\rho x,\xi,\theta)}$$
$$\times \left[\phi_{B,j}(\rho x,\rho y,\rho z) \cdot \tan\theta \cdot e^{-\mu_B^j \cdot \sec\theta_s} \cdot e^{-\mu_A^k \cdot g(\rho z,\rho y,\rho x,\xi,\theta,s)} \right] \cdot ds \cdot d\theta \cdot d\xi \cdot d\rho x \cdot d\rho y \cdot d\rho z$$

where r_k^A is the absorption edge jump ratio for the *k* line of element *A*; ω^k_A is the fluorescence yield for the *k* line of element *A*; p^k_A is the probability of X-ray emission; $\Delta\Omega/4\pi$ is the fraction of fluorescent radiation that reaches the detector after leaving the sample; $I_{B,J}$ is the produced primary intensity of the *j* line of element *B* which excites element *A*; $g(\rho x,\rho y,\rho z,\xi,\theta,s)$ is the distance between the point of X-ray generation and the point where the secondary X-ray leaves the particle (as a function of the coordinates, the polar and azimuthal angle); $\mu^j_{B,A}$ is the mass absorption coefficient of the *j* line of element *B* by element *A*, while μ^j_B is the mass absorption coefficient of the *j* line of element *B* by the matrix.

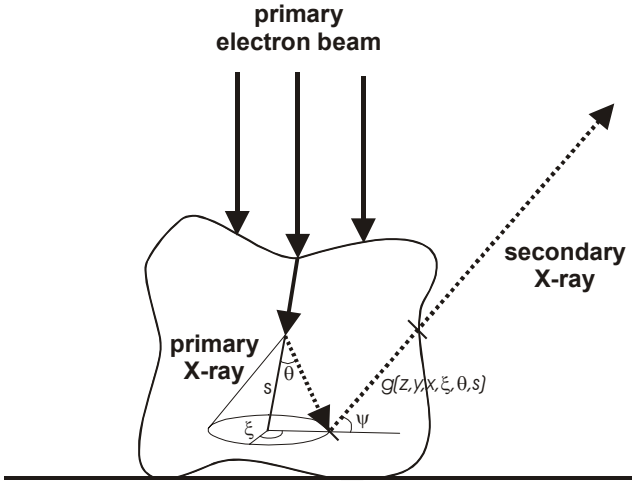

Figure 6: Schematic diagram of characteristic fluorescence in an irregular sample

It is clear that the exact analytical expressions are rather complex; therefore, Armstrong and Buseck have simplified them for specific particle types with ideal geometry, like cubes, spheres, cylinders or square pyramids. Armstrong also improved the depth distribution function in order to take into account electron transmission and side scattering more successfully. The resulting quantification procedure is based on the numerical integration of the simplified analytical expressions.

During analysis, the particles have to be irradiated with a defocused beam larger than their projected diameter, or the beam should be rastered over the projected particle surface, since the effect of particle shape on the emitted X-ray intensities could be huge using a point beam (especially for large particles). Initial *k* ratios are calculated as the intensities in the particles divided by the intensities in the bulk standards (giving a first concentration estimate after normalization to 100%). After that, the measured intensities are corrected in a typical ZAF iteration procedure, but based on a selected ideal geometry. Therefore, the choice of the model and the determination of the size parameters are very critical.
Storms et al. evaluated the quantification method and the effect of particle shape, and they found that the spherical particle model leads to intermediate absorption correction values between those of other particle types (with peak-top or top-peak shapes).[23] They found that the calculated deviations between the spherical model and the other shape models could amount to 78%. Especially in cases where the low-*Z* content of the particle cannot be estimated stoichiometrically, the model could reach unacceptable values. However, when the elemental results are normalized to a sum of 100%, the difference between the models becomes considerably smaller, and the dependence on the size is also significantly decreased (deviations less than 10%, in most cases even less than 1%). The spherical model could therefore be introduced as an average model during automated particle analysis.
In the conclusion of his evaluation of the Armstrong-Buseck particle ZAF corrections (with the implemented sidescatter and transmission corrections), Armstrong reports that the errors resulting when particle corrections are not applied, are systematic and can be as high as several hundred percent. He claims that the method is able to accurately analyse particles larger than 1-2 μm in diameter. However, for elements of greatly differing atomic number in particles smaller than 1 μm, significant errors can result in using the method, unless the particles are mounted on a substrate with similar atomic number (because the effect of backscattered electrons cannot be accounted for). Therefore, the choice of a suitable substrate is important, certainly when the particles are irradiated with a broad defocused beam. In his evaluation, Armstrong suggests that Monte Carlo calculations could be used for developing an accurate correction procedure for small particles, provided that correct expressions for the ionisation cross section and the mean ionisation potential are implemented. Zreiba and Kelly indeed used both a tracer technique and Monte Carlo calculations to determine $\phi(\rho z)$ curves for thin sphere analysis by TEM, and they indicated that electron sidescatter and transmission are not always well accounted for in the Armstrong-Buseck procedure.

- **Standardless "particle" *ZAF***

After standardless *ZAF* procedures were developed for thick polished samples, some researchers started to develop standardless methods for particle analysis.[24,25,26] The idea was not to work out exact mathematical expressions starting from theoretical formulae (like in Particle *ZAF*), but to adapt the conventional ZAF procedure using empirically obtained expressions. The electron backscatter and stopping power correction factor were calculated based on a formulae for ideal spherical particles according to Markowicz or Love, depending on the particle diameter. Simplified absorption and fluorescence correction factors for spherical particles were introduced using formulae developed by Armstrong and Small. The developers compared the method to Particle *ZAF*, and they concluded that the procedure had limited accuracy due to the high level of simplifications in the expressions of the correction factors. For accurate particle analysis, they indeed advise the use of accurate descriptions of the shape and texture of the analysed particles. However, if a large group of particles is to be analysed, they prefer a compromise between the speed of operation and the desired accuracy of the quantitative results. Their method could establish that compromise, since it requires less calculation time and no standard measurements.

1.3 Monte Carlo simulations

Monte Carlo methods could be defined as "numerical techniques to statistically simulate complex phenomena utilizing sequences of random numbers". Monte Carlo calculations (MC) have been used for many centuries, but it is only since several decades that their advantages for addressing complex applications have been recognized. Nowadays, many examples of MC can be found in different application fields like traffic flow studies, quantum mechanics, financial risk assessment or nuclear reactor design.[27] During World War II, scientists in the Manhattan project named them after the city of Monte Carlo, because of the similarities between statistical simulations and the games of chance played in the casinos of Monaco. The analogy of MC methods to gambling games is quite correct: the studied complex systems with almost unpredictable behaviour could be compared to the games, while the playing scientists win a possible solution to their questions. As for the "true standardless" methods mentioned before, the most critical aspect of MC is of course to describe the studied system with mathematical expressions.

The necessity, but moreover the difficulty to find correct expressions could be shown by considering, for example, a Monte Carlo method to predict the survival rate of people on a sinking ship. This value would not only depend on the individual 'characteristic properties' of the passengers on board (e.g. their stress resistance and swimming abilities), but also on an enormous amount of other factors and circumstances (e.g. the number of rescue boats and the weather conditions). Moreover, it would require good knowledge of the possible escape routes to predict how and where the people would try to get off the ship (e.g. people wearing a life vest on the upper deck would probably be in a better position to start, than those sleeping in a cabin). Therefore, translating all these factors into mathematical expressions is expected to be very difficult.

In case of electron microscopy, the interactions of electrons with solid matter have been studied for a long time, and many expressions have been formulated to describe the different occurring phenomena. [3,28,29,30,31,32,33] Of course, like in the example of the sinking ship, we need to know how to describe the properties of the interacting objects (electrons and atoms) and the circumstances (the measurement conditions) in order to simulate what could be the outcome (the generation of secondary electrons, X-rays, etc.). Due to the nature of electron beam interactions with solid matter, it appeared relatively easy to describe the occurring processes, e.g. compared to the difficulty that researchers have to simulate ion bombardment. Since Castaign's thesis in 1951, much research was carried out to find accurate expressions for the electron interactions and the resulting phenomena. [1]

At first, Monte Carlo simulations were only used to qualitatively check the classical quantification methods, or to assist in extending the knowledge on the shape of $\phi(\rho z)$-curves. For example, Armstrong checked the validity of some calculations in the Armstrong-Buseck procedure using Monte Carlo simulations.[21] However, nowadays the interest has risen into using MC methods directly for quantification calculations, especially for single particle analysis. Armstrong and Buseck accomplished the simplification of the exact mathematical correction expressions for some particle types with simple geometry.[20] However, finding simple numerical solutions for more complicated cases is expected to be difficult, but simulations could offer a solution.

The main goal of this thesis was to develop a standardless quantification procedure for single particle analysis by TW-EPMA (including the direct determination of low-Z elements, which could only be estimated from stoichiometry in earlier methods), based on Monte Carlo simulations that are expected to be more flexible. Paragraph 2 will describe the Monte Carlo simulation procedure that was used in this work, while paragraph 3 will discuss the evaluation of the quantification method.

2. Monte Carlo simulations for single particle analysis

2.1 From CASINO to Elementary

The Monte Carlo simulation software that was developed for particle analysis, is based on the code of another program made by the members of a Canadian research group at the University of Sherbrooke (P. Hovington, D. Drouin and R. Gauvin). The developed program called "CASINO" (Monte **Ca**rlo **si**mulation of electro**n** trajectories in s**o**lids) was described in three subsequent papers in 1997 and made available on the internet.[34,35,36] A first paper about the physics behind it already appeared in 1995.[37]

It was found that many formulae and models that were used earlier in Monte Carlo simulations or in quantification procedures, could not provide high accuracy for analysis using low-energy electron beams.[38] With the advent of FEG-SEM, it was necessary to solve this problem, since this technique performs analysis at accelerating voltages of less than 5 kV. Therefore, CASINO was especially designed for simulating electron interactions at low energies in thin films or in bulk samples. Additionally, the program could also simulate interactions for (spherical) inclusions in bulk species.

The algorithms for the simulations of the interactions in inclusions are quite similar to those needed for the trajectory simulations for single particles, which could be defined as inclusions in vacuum. Therefore, several members of the research group of Prof. Van Grieken put much effort into the modification of the CASINO code. An iterative loop for concentration calculations was added to the program afterwards. The first versions were made in Visual C++ and in Pascal, but they were either not user-friendly, or they could only access limited computer memory. For this reason, a new program called "Elementary" was developed, consisting of a Visual Basic user interface and a dynamic library file that contains the actual simulation code (made in Visual C++). Afterwards, more features were added to this program in order to integrate all available and necessary software for single particle analysis.[39,40,41,42]

The appendix at the end of this thesis will briefly discuss the features in Elementary. Although today at least one other program exists for simulating electron interactions in single particles (Electron Flight Simulator, SPI supplies Inc.), Elementary is believed to be the only one available for purely scientific purposes, containing a quantification procedure and many different features for single particles. In the next paragraphs, the simulation and quantification code will be explained in more detail.

2.2 Simulations step-by-step

The most important aspect in creating a Monte Carlo simulation program is **the generation of random numbers**. What we need for Monte Carlo calculations are uniform deviates, i.e. random numbers that lie within a specified range (typically 0 to 1), with any one number in the range just as likely as another. It is important to point out that probably every such number produced by a computer could only be "pseudo-random", since it would be impossible for a programmed, precise and deterministic machine to produce random data. For example, system-supplied random number generators are standard library routines of most program languages that are indeed able to produce a random sequence after they are initialised by an arbitrary seed value given by the user. However, the same initial value will always return the same random sequence. System-supplied generators have the disadvantage that they are not free of sequential correlation on successive calls, and not all of the numbers have the same generation probability; therefore, the use of these generators can be disastrous for MC.

However, it is possible to create other random number generators that do provide numbers with equal probability. The adapted CASINO program contains different generators published by Press et al. (1992), which provide uniform random numbers.[27] All of the implemented generators that can be selected by the user have been tested in different ways over many years and have accumulated a large amount of successful use in several applications.

During an EPMA measurement, the sample is irradiated by a beam of electrons with an initial energy proportional to the accelerating voltage. In our Monte Carlo calculations, the goal is **the simulation of electron trajectories**, so it is necessary to compute the coordinates and the energy of the electrons along their path in the sample. None of the individual trajectories produced by the simulation will represent a "real" trajectory, but a large number of trajectories will accurately describe effects that can experimentally be observed. For the calculations we need two basic pieces of information: the angles through which the electrons will be deflected as it travels through the specimen and an estimate of how far (on average) the electron will travel given some particular value of incident energy.
When an electron penetrates the sample, its interaction with the atoms in the sample will be either elastic or inelastic. In case of elastic collisions with an atom, the electron loses only a small amount of energy and the angle of collision will be quite large. Inelastic collisions have a contrary effect, i.e. severe loss of energy and small scattering angles. In the Monte Carlo simulations, we assume that only elastic scattering events are significant in determining the path of an electron moving through the specimen. However, the electrons are assumed to lose energy continuously, rather than as the result of discrete inelastic events. This simplification allows the net result of all possible inelastic scattering processes to be accounted for, without having to worry about the exact details of the individual events.
To take into account the energy loss along the trajectories, two approaches can be used. Plural or multiple scattering models calculate the total range of the electron trajectory first, after which the total path length is divided into a fixed number of segments of equal length. Single scattering models take into account each elastic scattering event suffered by the electrons as they travel through the sample. The adapted CASINO simulations are from the latter type, and the different steps in the procedure will be discussed below.

In the beginning of the procedure, the user must, of course, provide the program with information regarding the sample: the type and the composition of the different **sample regions** must be selected. In case of particle analysis, three different particle shapes can be chosen, i.e. spherical, hemispherical and cubic. Moreover, the particles could have a layered structure, which means they consist of a core surrounded by a shell. The particles are of course mounted on a substrate, which could be a thin film or a bulk solid. Depending on the selected particle and substrate type, different regions can be identified, for which a composition should be given (substrate; particle or core/shell). All regions are assumed to be homogeneous.

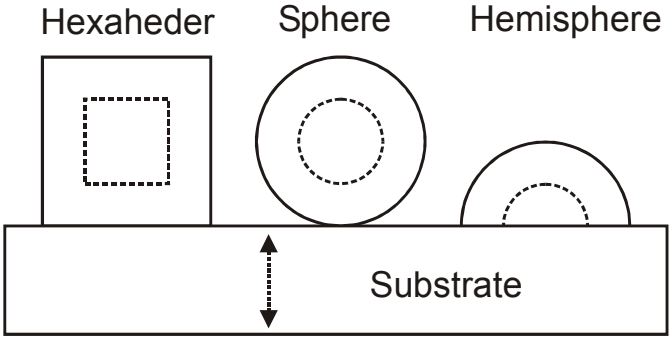

Figure 7: Different particle types

The **measurement conditions** should also be part of the input given by the user. Initially, this includes data related to the electron beam: the energy of the primary electrons (corresponding to the accelerating voltage), the beam size and the angle of incidence. The position of the electron beam with respect to the sample can also be chosen. In the current program, the specimen and the electron beam are assumed to be interacting in a vacuum chamber. Other data related to the X-ray detector will be discussed later.

Every electron starts its journey through the sample at a random position in-between the outer limits of the beam diameter (determined by a generated random number R_1). Afterwards, it propagates deeper and deeper into the sample, suffering several **elastic scattering events**. When the electron suffers an elastic collision at point P_i in a certain region of the sample, its trajectory is changed by a polar angle θ and an azimuthal angle ξ, after which it travels a distance L to point P_{i+1}, where it suffers another collision.

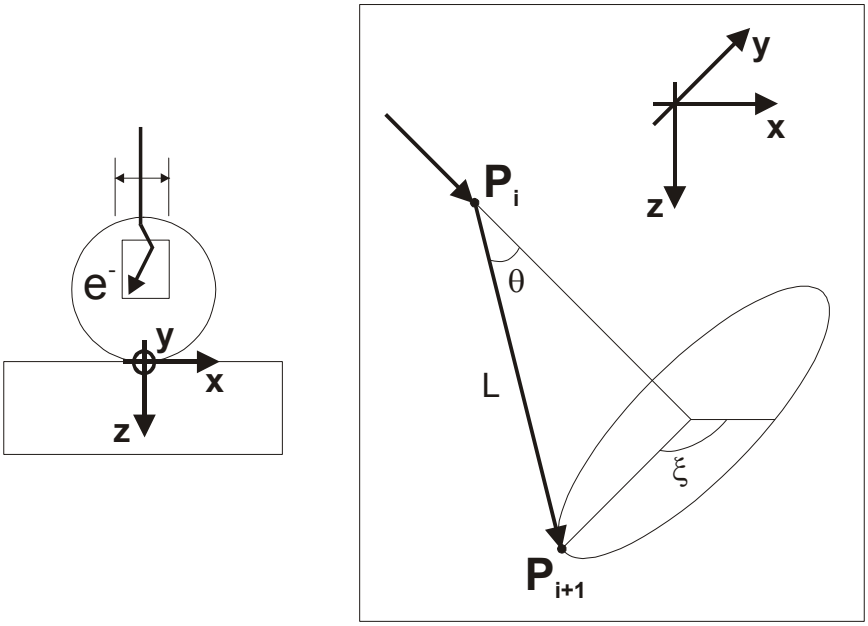

Figure 8: Coordinate system for Monte Carlo simulations

The initial step in these simulations is to determine which atom is responsible for the elastic scattering event, which is achieved by calculating a set of probabilities Π_j for each element in the corresponding sample region using the following formulae:

$$\Pi_j = \frac{\sum_{i=1}^{j} F_i \cdot \sigma_i}{\sum_{i=1}^{n} F_i \cdot \sigma_i}$$

where F_i is the atomic fraction of element i; n is the number of elements in the region. The total cross section σ_i of element i (in nm²) is a measure of the probability that an elastic scattering event (collision) will take place.

$$\sigma = 2\pi \int_0^{\pi} \frac{d\sigma}{d\Omega} \cdot \sin\theta \cdot d\theta$$

If the applied partial or differential cross section $d\sigma/d\Omega$ is simple, this equation may have a numerical solution, like in case of the Rutherford cross section. However, the Rutherford cross section is only valid for high-energy electrons; therefore, the Mott elastic cross section was also introduced in the program. The Mott cross section, however, needs numerical integration to solve the equation above, which can be done using the method by Czyzewski et al. (1990).[77] To simplify the Monte Carlo calculations, a database has been set up containing sequentially the values of the total cross section for 26 different energies between 20 eV and 30 keV. When the atomic number and the energy are given, the total cross section can be calculated by interpolating between the nearest lower and upper energies.
In order to determine the element that is causing the scattering event, we generate a random number R_2, which is uniformly distributed between 0 and 1. If the following relation is valid, the j^{th} element is selected:

$$\Pi_{j-1} \le R_2 < \Pi_j$$

To compute the polar angle θ, the following equation should be solved:

$$R_3 = \frac{\int_0^{\theta} \frac{d\sigma}{d\Omega} \cdot \sin\theta \cdot d\theta}{\int_0^{\pi} \frac{d\sigma}{d\Omega} \cdot \sin\theta \cdot d\theta}$$

Again the integrations above have to be solved numerically, and again a database was made to find the corresponding angle using the generated random number R_3. The ratio above has been computed and tabulated for 26 different energies as a function of the polar angle. For a given random number, the nearest lower and upper ratio values can be found for both the nearest lower and upper energy values. The polar angle θ_E for the actual energy E can then be calculated by interpolation:

$$\theta_E = \theta_{E\min} + \frac{(E - E_{\min}) \cdot (\theta_{E\max} - \theta_{E\min})}{E_{\max} - E_{\min}}$$

where

$$\theta_{E\min} = \theta_{E\min}(Ratio_{\min}) + \frac{(R_3 - Ratio_{\min}) \cdot [\theta_{E\min}(Ratio_{\max}) - \theta_{E\min}(Ratio_{\min})]}{Ratio_{\max} - Ratio_{\min}}$$

$$\theta_{E\max} = \theta_{E\max}(Ratio_{\min}) + \frac{(R_3 - Ratio_{\min}) \cdot [\theta_{E\max}(Ratio_{\max}) - \theta_{E\max}(Ratio_{\min})]}{Ratio_{\max} - Ratio_{\min}}$$

The azimuthal angle ξ is uniformly distributed from 0 to 2π and given by R_4, another random number:

$$\xi = 2\pi \cdot R_4$$

The angles θ and ξ are formed by the last and the new directions of the electrons, so we must recalculate the direction relative to the fixed axis. The direction cosine ($D_{x,i+1}$, $D_{y,i+1}$, $D_{z,i+1}$) can be computed from the old value ($D_{x,i}$, $D_{y,i}$, $D_{z,i}$).

$$D_{x,i+1} = \frac{D_{z,i} \cdot \sin\theta \cdot \cos\xi}{\sqrt{D_{x,i}^2 \cdot D_{z,i}^2}} + \frac{D_{x,i} \cdot D_{y,i} \cdot \sin\theta \cdot \cos\xi}{\sqrt{D_{x,i}^2 \cdot D_{y,i}^2 + \left(D_{x,i}^2 + D_{z,i}^2\right) \cdot \left(D_{x,i}^2 + D_{z,i}^2\right) + D_{y,i}^2 \cdot D_{z,i}^2}} + D_{x,i} \cdot \cos\theta$$

$$D_{y,i+1} = \frac{D_{x,i} \cdot D_{y,i} \cdot \sin\theta \cdot \cos\xi}{\sqrt{D_{x,i}^2 \cdot D_{y,i}^2 + \left(D_{x,i}^2 + D_{z,i}^2\right) \cdot \left(D_{x,i}^2 + D_{z,i}^2\right) + D_{y,i}^2 \cdot D_{z,i}^2}} + D_{x,i} \cdot \cos\theta$$

$$D_{z,i+1} = \frac{D_{x,i} \cdot \sin\theta \cdot \cos\xi}{\sqrt{D_{x,i}^2 \cdot D_{z,i}^2}} + \frac{D_{y,i} \cdot D_{z,i} \cdot \sin\theta \cdot \cos\xi}{\sqrt{D_{x,i}^2 \cdot D_{y,i}^2 + \left(D_{x,i}^2 + D_{z,i}^2\right) \cdot \left(D_{x,i}^2 + D_{z,i}^2\right) + D_{y,i}^2 \cdot D_{z,i}^2}} + D_{z,i} \cdot \cos\theta$$

where

$$D_{x,i(+1)}^2 + D_{y,i(+1)}^2 + D_{z,i(+1)}^2 = 1$$

The distance L between two collisions can be calculated using another random number R_5:

$$L = -\lambda \cdot \ln\left(R_5\right)$$

In this equation, λ represents the electron mean free path (in nm):

$$\lambda = \frac{10^{21}}{N_A} \cdot \frac{\sum_{i=1}^{n} \frac{C_i \cdot A_i}{\rho}}{\sum_{i=1}^{n} F_i \cdot \sigma_i}$$

where C_i is the weight fraction, F_i is the atomic fraction, A_i is the atomic mass and σ_i is the total cross section for element i; ρ is the density of the region and N_A it the Avogadro number. Using the distance and the direction cosine, the next position of the electron is computed. However, additional corrections have to be carried out in case the electron has moved to another region. For example, we will consider an electron moving from a spherical particle having a core region surrounded by a shell to a bulk substrate.

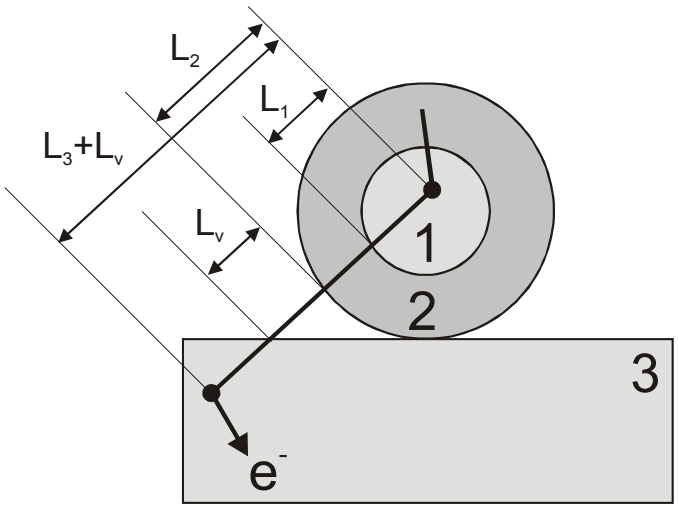

Figure 9: Electron traveling through a spherical particle on a substrate

The electron shown in Figure 9 first moves from the particle core (region 1), through the particle shell (region 2) to the substrate (region 3). The initial distance L should therefore be recalculated, since the different chemical composition of each region influences the travelled distances. This correction is done in an iterative way to correct for all of the consecutive border crossings. For example, a recomputed distance L_j would be given as

$$L_j = L_{j-1} - \lambda_j \cdot \left(\ln R_{5'} + \sum_{i=1}^{j-1} \frac{L_i - L_{i-1}}{\lambda_i} \right)$$

When leaving the particle shell, it also travels through vacuum before entering the substrate, so special care should be taken to exclude distance L_v from the calculations (in case of L_3 in the example). In order to apply the necessary corrections in the simulation procedure, the movement of each electron is continuously followed, checking if it has crossed the border of a region. All data regarding each electron trajectory are stored for later use. A trajectory stops when it has moved outside of the sample system, or when the electron energy is too small to excite any element in the sample.

Energy loss along path L (in one region) is considered to be constant, since a continuous slowing down approximation is used in this program. The energy at position $i+1$ is computed by the following equation:

$$E_i = E_{i-1} - \frac{dE}{dS} \cdot L$$

The rate of energy loss dE/dS (in keV/cm) is calculated from the following formula by Bethe:

$$-\frac{dE}{dS} = -\frac{7.85 \cdot 10^4 \cdot \rho}{E_i} \cdot \sum_{j=1}^{n} \frac{C_j \cdot Z_j}{A_j} \cdot \ln\left(\frac{1.166 \cdot E_j}{J_j^*} \right)$$

where C_j, A_j and Z_j are the weight fraction, the atomic number and the atomic weight of the element j in a system of n elements. J^*_i is the modified mean ionisation potential (in keV), calculated with the formula below, in which k and J_i are a constant and the mean ionisation potential respectively (both functions of Z_i):

$$J_j^* = \frac{J_i}{1 + k \cdot J_i / E_i}$$

Another part in the simulation procedure involves **characteristic X-ray generation**. During the simulations, a temporary database is created containing all trajectory data, from which the distances and the mean energies between successive collisions are computed. The mean energy for every two collisions is used to calculate the number of ionisation events with the ionisation cross section Q_i. Various cross sections are available in the program and can be selected by the user. The events are assumed to be uniformly distributed between two collisions, so all events are assigned to layers of constant depth in the sample. When all events for all collisions of every electron are determined, a routine is called to process the X-ray generation of each element separately. For every element, the critical ionisation energies for the K, LIII and MV shells are taken into account (if applicable).

The intensity of the characteristic X-rays that are generated between collisions while the electrons travel in the sample, is given by:

$$I_i = \frac{Q_i(E_m) \cdot \omega_i \cdot \alpha_i \cdot C_i}{A_i} \cdot \rho \cdot L$$

$Q_i(E_m)$ is the ionisation cross section of element i, calculated with the average energy of the electron E_m between collisions; ω_i, α_i, C_i, ρ and A_i are the fluorescence yield, the relative intensity factor, the weight fraction, the density, the atomic weight of element i respectively; L is the distance between collisions.
It is also possible to generate $\phi(\rho z)$ curves in the program. For the shells of every element (K, LIII or MV), the number of ionisation events at each sample layer is then normalized by the number of ionisation events produced by a single film of the same thickness.

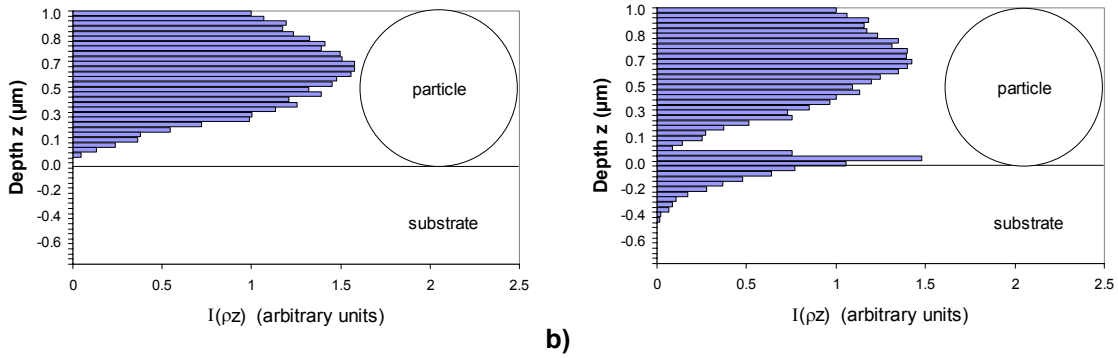

Figure 10: Distribution curve obtained for a spherical SiO_2 particle with a diameter of 1 µm on a bulk Si substrate (E_0 = 10 kV): a) O, b) Si

In addition, a procedure for the calculation of the **Bremmstrahlung background** was also implemented in the program. The background intensity at energy E is given as:

$$I_b(E) = \frac{Q_b(E, E_m, \phi)}{A} \cdot \Delta E \cdot \rho \cdot L$$

where ϕ is the angle between the axis of the detector and the trajectory of the electron; ΔE is an energy window of generated photons; E_m is the average electron energy between collisions; ρ is the density of the sample; A is the average atomic weight of the region where the electron travels. Using the parameterisation of Kirkpatrick and Weidmann,[43] the cross section for the generation of Bremsstrahlung, Q_b, can be calculated using two parameters I_x and I_y:

$$Q_b(E, E_m, \phi) = I_x \cdot \sin^2 \phi + I_y \cdot (1 + \cos^2 \phi)$$

The calculation of the background intensity at each energy value is performed every time when an electron collides in the sample and changes its trajectory, independent of the characteristic X-ray calculation.

When the generated X-ray photons travel in the sample before being detected by a detector, they suffer **absorption** by the sample itself, according to Beer's law. To calculate the attenuation of the X-rays by absorption, the distance travelled by the photons, the density of the sample and the values of the mass absorption coefficient for the X-ray photons in the sample are necessary. The calculation of the distance travelled by the photons requires taking care of various situations according to the sample geometry.

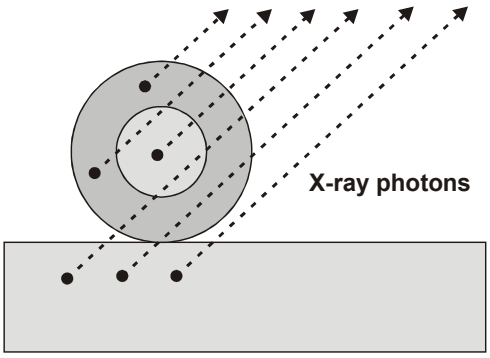

Figure 11: X-ray photons traveling through a spherical particle

Figure 11 shows the six different cases for the example of a spherical particle (with core and shell). Like for the simulation of the electron trajectories, each case should be treated differently in the calculation of the absorption of X-ray photons emerging towards the detector. Again, by calculating the distances travelled by the photons in different regions and excluding the vacuum region in the calculation, the absorbance by the sample can be correctly simulated.

In addition to X-ray absorption in the sample, measured X-ray intensities are also affected by the **efficiency of the X-ray detector**. The detector strongly absorbs photons of low energy, and in order to adapt the simulated intensities according to the detector efficiency, the user must supply the program with exact data about the composition, thickness and structure of the different parts of the detector (the protective window, the active part of the detector crystal, the dead layer of the crystal and possible contamination on the window). With the implementation of the detector efficiency function, it is possible to compare simulated with measured X-ray intensities, and even the simulation of spectra could be achieved.

2.3 Iterative procedure

From measurements by TW-EPMA, the analyst has obtained the particle geometry and the X-ray intensities for all of the detectable elements present in the sample. In order to obtain the estimated values of the concentrations of constituent elements, the quantification procedure employs reverse Monte Carlo calculations in an iterative procedure based on a robust successive approximation algorithm. A set of nonlinear equations of the mathematical relationship between the concentrations and the characteristic intensities can be given as:

$$
\begin{aligned}
&I_{1,meas} = p \cdot I_{i,sim}\left(C_1, C_2, .., C_n, d, \rho\right) \\
&I_{2,meas} = p \cdot I_{2,sim}\left(C_1, C_2, .., C_n, d, \rho\right) \quad \sum_{i=1}^{n} C_i = 1 \\
&\ldots \\
&I_{n,meas} = p \cdot I_{n,sim}\left(C_1, C_2, .., C_n, d, \rho\right)
\end{aligned}
$$

where C_i represent the concentrations of the n elements that are found in the particle; ρ is the particle density; d is the particle diameter; $I_{i,meas}$ and $I_{i,sim}$ are the measured and simulated intensities; factor p includes all proportional instrumental parameters (such as the accelerating voltage, the solid angle of the detector, etc.). Although the form of these mathematical expressions cannot be given explicitly, the set of equations is applicable to model the X-ray intensities from the particle. Practically, the aim of the reverse Monte Carlo approximations is to find an exact solution for it based on a few presumed conditions.

1. The particle material is assumed to be homogeneous.
2. All of the elements in the sample with $Z > 5$ are detected.
3. The particle is located on a flat surface having a known composition.
4. The shape of the analyzed particle is spherical, hemispherical or hexahedral.

To start the iterations, an initial set of estimated concentrations is calculated from the measured intensities:

$$C_i^1 = \frac{I_{i,meas}}{\sum_{j=1}^{n} I_{j,meas}}$$

Since the quantification routine is an iterative procedure, the obtained results are evaluated after every Monte Carlo simulation, i.e. the simulated intensities are compared to the measured intensities using two criteria:

$$\left|C_i^{(k)} - C_i^{(k-1)}\right| < \varepsilon \qquad \text{en} \qquad \sum_{i=1}^{n}\left(\frac{\left(I_{i,meas} - I_{i,sim}\right)^2}{\sigma_i^2}\right) < \delta$$

where $C_i^{(k)}$ is the k^{th} approximation of the i^{th} element; σ_i is the standard deviation of the measured intensity; δ and ε are values chosen by the user, which determine when the iteration routine should be stopped. If the criteria above are not met, a new set of estimated concentrations is calculated according to the following formula:

$$C_i^{(k)} = \frac{I_{i,meas} \cdot C_i^{(k-1)}}{I_{i,sim}^{(k-1)} \cdot \sum_{j=1}^{n} \frac{I_{j,meas} \cdot C_j^{(k-1)}}{I_{j,sim}^{(k-1)}}}$$

From the equation it is clear that the concentrations are normalized; this is based on the assumption that (practically) all the constituent elements are observed.
The existence and uniqueness of a mathematical solution obtained by successive approximation using the expression above was proven. When the iteration criteria above are indeed fulfilled, the simulations are stopped and the last set of estimated concentration values are considered to match the real elemental concentrations in the sample.

3. Testing and improving the method

Below you will find a discussion about the evaluation of the Monte Carlo simulation model, in which **two different approaches** were used. In the *bottom-up* approach, the purpose is to describe the individual parameters that have a direct or indirect influence on the final result, i.e. the different uncertainties of the input data on the quantification. Well begun is half done, so, if possible, an optimisation was carried out in order to minimize these uncertainties. The *top-down* approach gives an evaluation of the quantification after optimisation, i.e. a discussion of the quality of the final results.
Most of the experiments for evaluating the Monte Carlo method required the use of **standards**. Because we didn't have any certified standards for individual (environmental) particles, we had to find a solution. Some particle standards can be found on the market, but their purpose is mostly to test particle *size* measurements.[44,45,46,47] These particles have geometries and compositions that are not representative for the 'real' particles that we are interested in, since they are mostly spherical or too large (e.g. 10-100 µm), and since their exact composition is mostly unknown. Therefore, we generated our own particle standards starting from typical inorganic or organic salts of *pro analysis* grade.
In one method, salt crystals are solved in methanol or ethanol (with or without some additional water for better solubility) and then sprayed onto a substrate using an airbrush method. The solution is sprayed into a relatively long tube using a fine paintbrush, and during the travel through the tube, the solvent will evaporate. The other end of the tube is attached to an impactor with an appropriate low-volume pump. The sprayed particles are sampled on the stages of the impactor, so particles of different size ranges could be obtained. The advantage of this method is that the standards are created under similar conditions as for the 'real' sampling of atmospheric particles. A disadvantage is the incorrect size separation in case the solvent or water is not evaporated completely when entering the impactor. On the other hand, atmospheric particles are also known to be slightly humid, so in fact this problem occurs in real sampling as well. However, remaining solvent on the particle surface should be considered as contamination, so all samples were allowed to dry during some hours.

Figure 12: Airbrush system for generating particle standards (from left to right: Berner impactor, evaporation tube, airbrush)

In another method, a suspension in n-hexane is made of salt crystals that were crushed and ground to fine powder using a mortar. The suspension is then dropped onto the substrate using a micropipette, after which the droplets are put to dry. The advantage of this method is of course that it is applicable to compounds with low solubility. A bottleneck is the production of powder that is fine enough. A disadvantage is the use of microdroplets instead of a spray, because the suspended particles tend to 'stick together' when the solvent is evaporating, often resulting in salt crusts instead of fine particles.

In a third method, no solvent is used and the crystal powder is 'sprinkled' onto the substrate. Again, the production of fine enough powder is critical. The main disadvantage compared to solution or suspension methods is that the produced particles do not 'stick' as well to the substrate surface. The airbrush method in particular has the advantage that the particles are impacted or 'smashed' onto the surface of the substrate.
Other techniques appeared to be useful in case of sediment particles, e.g. suspension of ground particles. However, in most of the experiments for the evaluation and optimisation of TW-EPMA, the airbrush technique was preferred, because of the similarities with the real sampling of atmospheric particles.

3.1 Bottom-up evaluation and optimisation

- **Particle size, shape and density**

Some input parameters are required that describe the analyzed particle in order to calculate its elemental concentrations. Besides the measured X-ray intensities that will be discussed in another section below, the particle size, shape and density should be given to the Monte Carlo program. Three particle types are currently possible to select in the program, namely the spherical, hemispherical or hexahedral shape, but more shapes could be added in the future. For each particle shape, the relevant size parameters should be given (diameters for spheres, heights and diameters for hemispheres, rib sizes for hexahedra). The density is of course also an obligatory input value for each particle.
Particle morphology might seem very easy to determine, since we examine each particle using our electron microscopes. Nothing is further from the truth, although we must say that tests using standard particles with well-known sizes indeed showed that the size measurements by our microscopes in MiTAC are quite accurate and precise.[48] First of all, few particles have the ideal particle shapes that we can select in the simulations. Most environmental particles are irregular in shape due to the fact that they were exposed to many chemical and physical transformations before ending up in our microscope. So, this means that the analyst somehow has to determine from the 2D-image on his screen which ideal particle type matches the best to the real, irregular shape, which is not always very easy. One of goals was therefore to find out what is the influence of the selected particle shape on the quantification. Secondly, the fact that we can only see the particles in two dimensions, results in another problem. From one image we can only determine particle size parameters in the X- and Y-direction, and it is impossible to give information about the Z-direction (the particle height). This means that we also had to find a way to deal with this problem, and to estimate the uncertainty on our quantification results due to it. The particle density is even more complex to determine, since the only way to estimate a particle density would be to calculate it starting from parameters that are actually supposed to be unknown and that we would like to calculate with our simulations. So, it appears to be impossible to calculate the particle density.
To find answers to our many questions, we started with what seemed to be the easiest part: the particle sizes. A first attempt was made to determine the exact size of artificial NaCl-particles, like the one in the picture below, and this in all three dimensions using two different images. One image was taken as usual, and another was taken at a tilt angle of 60°. After measuring the visible ribs of the cubes in the two images, simple goniometric formulas were used to determine the three size parameters using this formula for each rib R:

$$R^2 = R_0^2 + \frac{4}{3}\cdot\left(R_{60}^2 - R_0^2\cdot\sin^2\theta\right) + \frac{1}{3}R_0^2\cdot\cos^2\theta - \frac{4}{3}\cdot R_0\cdot\cos\theta\cdot\sqrt{R_{60}^2 - R_0^2\cdot\sin^2\theta}$$

where R_0 and R_{60} are the measured ribs at 0° and 60° respectively, and θ is the angle (seen at 0°) between the axis perpendicular to the stage rotation axis. The formula is obtained by considering the fact that the sample stage is tilted clockwise, so the coordinates at 60° can be described by transforming the coordinates at 0°.

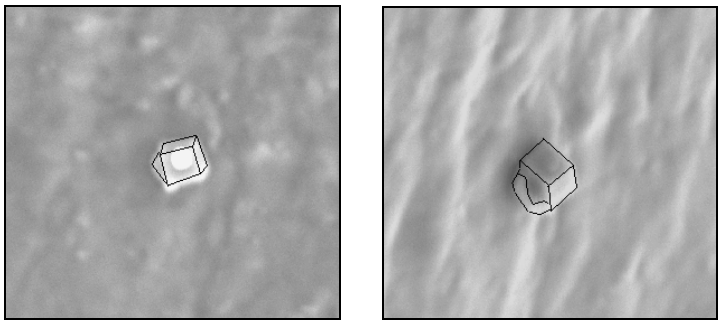

Figure 13: Measuring the sizes of NaCl-particles at 0° (left) and 60° (right) tilting angle (for clarity solid lines are added along the sides)

When the particle sits flat on the surface and only two sides of a particle can be seen, the height could also be calculated by:

$$H = \frac{H_{60}}{\sin 60°}$$

It is probably not too hard to convince the reader that determining the size parameters in such a way is not evident. First of all, we took advantage of the fact that our artificial NaCl-particles have almost ideal, cubic shapes. As was explained above, the morphology of real environmental particles is much rougher than, and not as ideal as in the case of artificial particles, which are in fact crushed crystals. Secondly, it would be very time-consuming to measure the dimensions of each particle in two different images. Our tilting device cannot be operated automatically, so each particle should be measured manually, which is utopian in case one has to measure a thousand particles. Automatic analysis of tilted samples is impossible anyway, because then the beam should be focussed after every lateral stage movement (the surface of the sample is not perpendicular to the beam axis). So at this point of our search for answers, we were back to zero.
Therefore, we saw no other option than to seek refuge in estimations and assumptions. Past research for the development of ZAF quantification models concluded that the use of the spherical shape often resulted in satisfying results for most environmental particles, and that normalization procedures were very effective in dealing with particle size effects. So it was quite obvious that we had to test if we would also come to the same conclusion with our Monte Carlo simulation model. The problem of determining the particle size is of course closely connected to our question about the particle shape. If it would be valid to predetermine the type of particle (i.e. to assign the spherical shape as the standard particle shape in our simulations), this raises questions about the accuracy with which the particle size has to be determined. If the shape selection would not be so critical, neither would of course be the size of the particle. Testing our simulations on the analysis of standard particles showed that indeed the apparent concentration of the particle elements varies only in a relatively narrow range due to the average diameter of the particle as illustrated in the figure below, which shows 5-10 % variation of the elements in a $CaSO_4$ particle over the diameter range 400-2000 nm (considering 10 kV as accelerating voltage). Although the shapes of $CaSO_4$ particles are quite fanciful, the assumed spherical shape does result in relatively nice results.

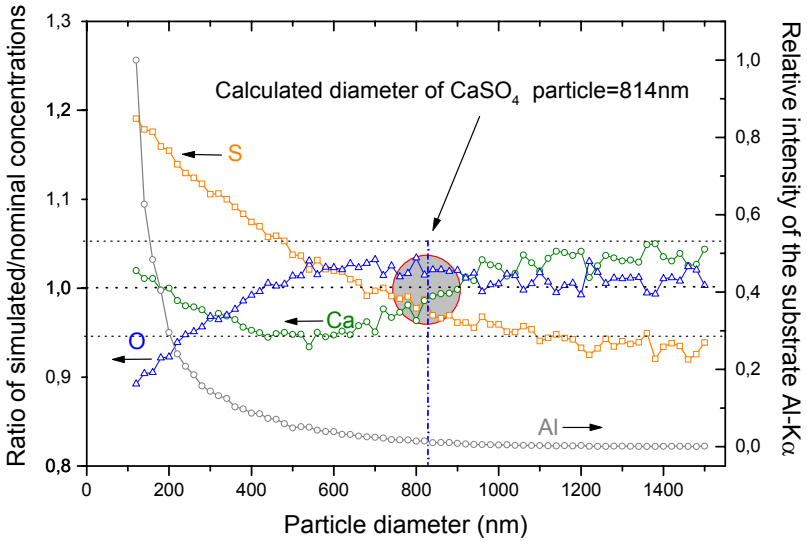

Figure 14: Successive approximation with diameter variation for a standard $CaSO_4$ particle

The reason for the conclusions above is actually very simple and can be found in a favorable property of electron-induced X-ray emission. The detected X-ray flux is emitted mostly from the volume located directly under the particle surface because of the strong attenuation of the low-energy X-ray lines. An opposite relationship is expected between the particle diameter and the intensity of the substrate lines, because of the attenuation effect in the particle volume. Increasing the particle diameter results in a lower number of electrons in the substrate volume; therefore the emitted number of X-ray quanta of the substrate lines is being decreased.

A similar dependence of the intensities on the sample density is expected, since the particle density also determines the electron penetration depth (one could also relate this to the atomic number effect). Therefore, we introduced the measured and simulated substrate intensities into the iterative algorithm. Because of the general insensitive behavior of these parameters, the diameter or the density can be varied during the iteration process in order to fit the calculated substrate intensity to the measured one, yielding more realistic result. In practice, after every iteration step of the concentration calculation, an optimization procedure for the diameter is performed based on the minimization of difference between calculated and measured substrate intensities. The obligation that also the substrate intensity should be correctly simulated, is expected to compensate for the improper determination and the uncertainty of the particle density.

With regard to the particle shape, the spherical form appears best to fit into the above conclusions. Most standard particles do not have spherical shapes, since they originate from ground crystals, however, as will be shown in many discussions below, the assumption that the analyzed particle is spherical, does indeed lead to quite satisfying results. It is interesting to note that the reported particle size in automatic analysis is in fact an equivalent geometrical diameter corresponding to a ‘spherical’ particle, i.e. the diameter corresponds to that of a disc with the same area as the 2D-surface of the analyzed particle in a backscattered-electron image (see also previous chapter). Since the automatic analysis procedure also provides a shape factor that expresses the roundness of the particle surface as a relationship between the surface and the perimeter of the analyzed particle, we tested the possibility to link it to the choice of the particle shape. However, we experienced that the shape factor is not always a trustworthy measure for the particle shape, and therefore we abandoned the idea. We set the spherical shape as the standard particle type, unless we had reason not to (e.g. in case of NaCl-cubes).

- **Substrate quality**

The substrate plays an important role in particle analysis, since it has a high influence on electron imaging and X-ray acquisition. Therefore, the first step in the optimization of TW-EPMA was to find a suitable substrate for sampling and analyzing the particles. Besides financial or other non-analytical aspects, the most important analytical criteria that describe the 'ideal' substrate are: 1) high image contrast for efficient particle recognition, 2) high sensitivity for (low-*Z*) elements, and 3) limited or no contribution to beam damage effects.
Beam damage effects will be dealt with in the next paragraph, but this paragraph discusses the comparison of several typical substrates for particle analysis in view of the other aspects. The investigated substrates are polycarbonate filters, silver and aluminium foil, silicon wafer, beryllium discs, carbon tape and TEM grids. The polycarbonate filters that are produced by etching thin polymer films, will be referred to as 'Nuclepore' (the well-known commercial name). The metal foils are commercially available from different manufacturers, except for the aluminium which is especially produced for use in Berner impactors. The silicon wafers were obtained from the Interuniversitary Micro-Electronics Centre (IMEC, Belgium). Two types of beryllium were studied, i.e. thick discs by Goodfellow Inc., and thin planchets distributed by SPI Inc. that are especially produced for electron microscopy. The investigated TEM-grids (Ted Pella Inc., Carbon grid type A) consist of a copper grid, on which an ultrathin carbon layer was deposited (3-4 nm).

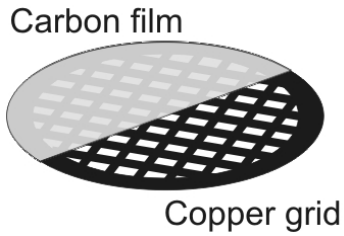

Figure 15: Structure of the investigated carbon grid

The topography or **surface roughness** is critical for the visual recognition of particles in secondary electron images (SEI). If the surface of a substrate is very rough, it will be difficult to distinguish microparticles from topographical microstructures on the substrate's surface.
The table and the figures below already give an overview of what to expect from the investigated substrates.

Table 1: Basic substrate properties

	Nuclepore	C	Al	Be	Ag	Si	TEM-grid
Thickness (mm)	0.02	0.5	0.2	0.5	0.3	2.0	0.02
Roughness (nm)	≈ 1-5	≈ 1000	≈ 500	≈ 500	≈ 100	≈ 1-5	≈ 1-5
Cost	medium	Low	low	high	medium	high	medium
Major elements	C,O	C,(O,…)	Al,(O)	Be,(O)	Ag,(O)	Si,(O)	C,(O)/Cu
Purity level (%wt)	99.99	> 95.00	99.89	99.85	99.89	99.99	99.99

Nuclepore filters, silicon wafers and TEM grids have very flat surfaces. Of course, polycarbonate foil contains filter holes, but these are well-recognisable and do not cause any identification problems. The TEM carbon layer is of course divided in different square areas by the copper grid, but if a large enough mesh size is chosen, this shouldn't provide any problems for the analysis. Of course, the larger the grid size, the more brittle the thin carbon film will be; the layer could then be damaged during sample manipulation (tweezers, etc.).

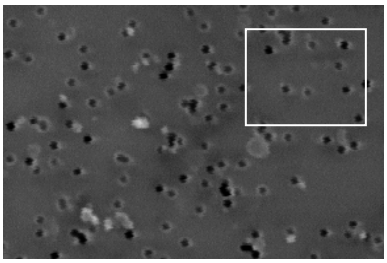

a) Nuclepore

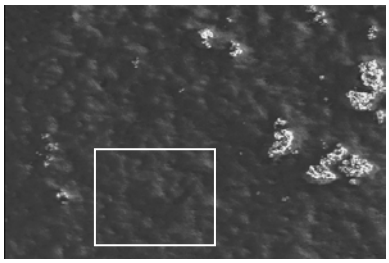

b) carbon tape

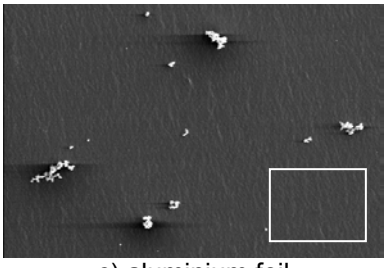

c) aluminium foil

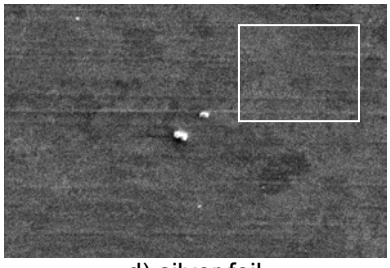

d) silver foil

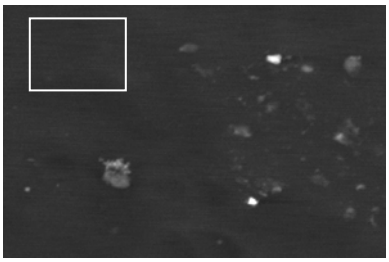

e) beryllium disc

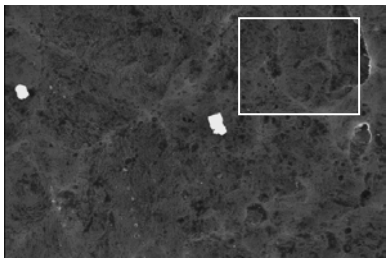

f) beryllium planchet

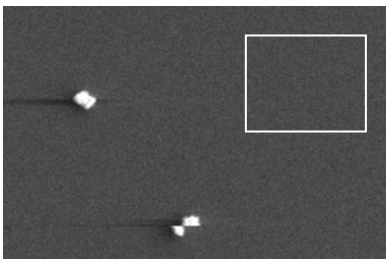

g) silicon wafer

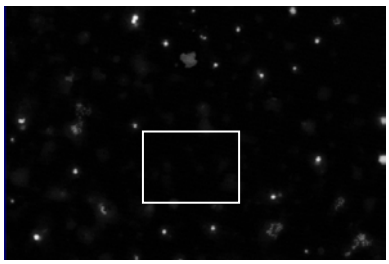

f) TEM grid

Figure 16: Surfaces of typical substrates (the rectangles indicate pure substrate areas)

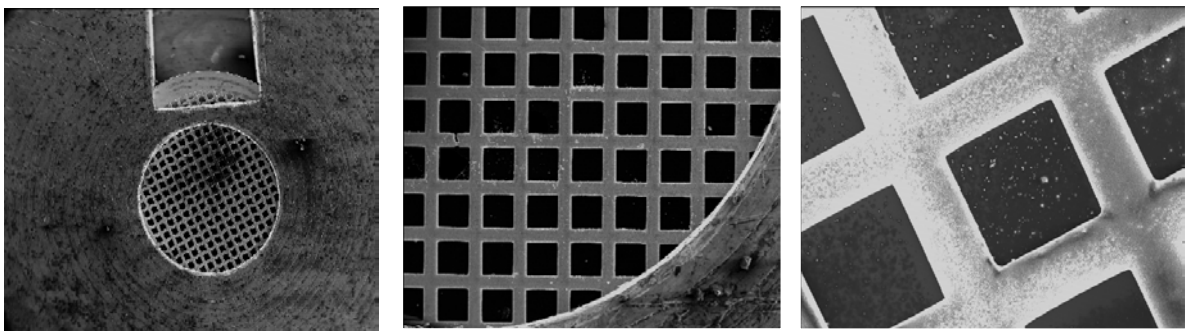

Figure 17: TEM grid (specimen holder - left; grid structure - middle and right)

We encountered many quality problems with beryllium discs or planchets. It is well-known that pure beryllium is difficult to produce, so all substrates contain a high amount of beryllium oxide, which is very brittle. During the production of the discs or planchets, the surface could be damaged very easily, since the different (thermal) treatments introduce rough structures. After several complaints to the distributor, we were told that the manufacturer could not assure 100% contamination-free surfaces; the product, however, is still described as 'high quality substrate for electron microscopy'.

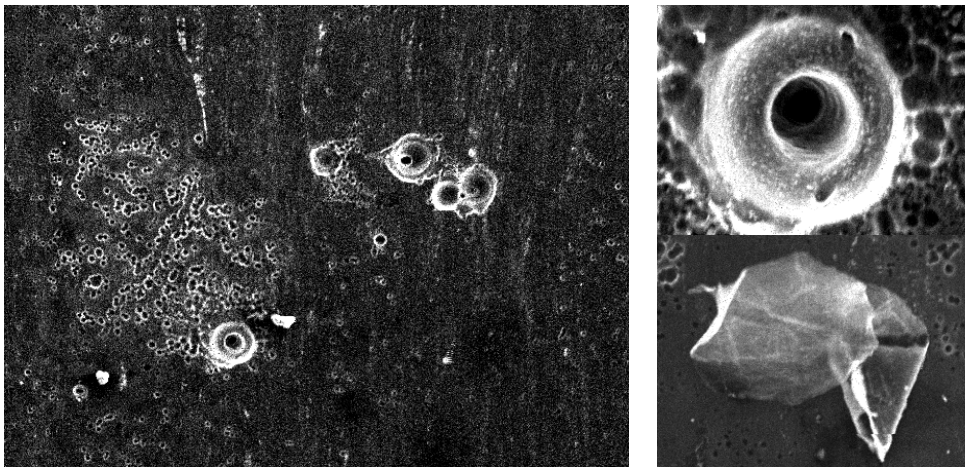

Figure 18: Brittle surface of beryllium (detail pictures on the right, roughness 1-10 µm)

Silver foil is quite flat, except for some line patterns that could also be caused by the manufacturing process. Aluminium foil also shows manufacturing patterns, but these are much finer and it is often difficult to distinguish particles from substrate roughness.
It is obvious that carbon tape is not useful for the analysis of small particles, since the structure of the tape is very rough. So, in view of surface structure, we decided not to retain carbon as an option for the analysis of atmospheric particles.

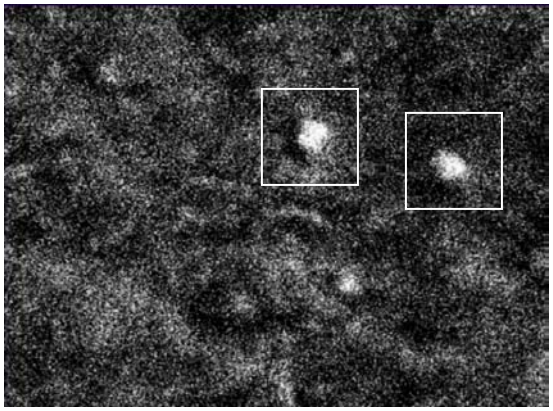

Figure 19: SEI of particles collected on aluminium (real particles indicated, ~0.5 µm)

Electron charging affects imaging as well as X-ray acquisition, because the charged sample deflects incoming electrons from the electron beam. Most environmental, particulate samples are electronically non-conductive, so the strategy for conventional SEM to avoid sample charging consists of coating the particles with a very thin layer of a conductive material like carbon. Although coatings offer an ideal solution in conventional SEM, this is not the case in TW-EPMA due to X-ray absorption and spectral interference effects.

The absorption of X-rays emitted from heavier elements (Z > 10) is low enough not to influence EDX-analysis in conventional SEM. However, the attenuation length of low energy X-rays (100-700 eV) is much shorter, and conductive coating of samples is therefore not desirable in TW-EPMA. Coatings of carbon or metals also introduce large inaccuracies in the quantitative determination of these elements in the particle. Most of the metallic coatings, e.g. silver and gold, are also not recommended due to the overlap of L and M X-ray lines of the coated material with characteristic lines of light elements in the particle. Although flat polymer foils like Nuclepore showed to be ideal substrate materials for conventional SEM, they cannot be applied for low-Z analysis, because the main elements in the filter are carbon and oxygen. Purely based on its composition, the same conclusion could be made for TEM grids, but it will be shown that this is not the case (see later). The metal grid and the carbon layer of this substrate also allow for good electron conductivity. For all substrates, charging was never observed to be critical for our analysis, except in the following cases: 1) when the semicondive substrate silicon was cooled down with liquid nitrogen to -193°C to reduce beam damage, as will be explained later; 2) when big particles (>10 μm) showed local charging on top of their surface (this could cause the particle to 'jump away' during irradiation).

As was explained in the previous chapter, our automated particle analysis software uses the **backscattered electron signal** for particle recognition, based on the contrast in mean atomic number *Z* between the substrate and the particles. Therefore, the next step in our substrate investigations was to test the particle-substrate contrast in backscattered electron images (BEI) of the remaining substrate candidates. This was done by making BEI of calcium carbonate particles on the different substrates (Al, Si, Ag, Be, TEM grids). For $CaCO_3$ particles of about the same size (1-2 μm), a signal profile was made along a line over the BEI. Calcium carbonate was selected for this experiment, because its average atomic number (10) is of the same order as the atomic numbers of the common atmospheric particle types (e.g. ammonium sulphate 6.6, sodium nitrate 8.4, sodium sulphate 11.9).
The figures below show the SEI (left), the BEI (right) and the BEI line profile (middle) for the different substrates. The images were made using an accelerating voltage of 10 kV, a beam current of 1 nA and identical image settings for all images. The backscattered electron signal was inverted for making the BEI of the particles on silver, since this substrate has a higher atomic number (47) than most of the particles on its surface. In normal mode, the obtained images would be negative (i.e. particles would be observed as valleys or negative peaks).
The line profile for the TEM grid appears to be better than those for the other substrates, since the particle peak is sharp and the substrate baseline is almost flat. The reason is the fact that the TEM grid is only a thin carbon layer, while the other substrates are considered to be infinitely thick. Therefore, the generation yield for backscattered electrons (and X-rays, see later) in the TEM grid will be much smaller, and the contrast with the particles will be higher.
The baseline for beryllium and silver is quite rough, but it is clear that the line profiles for aluminium and silicon are much worse. The signal-to-noise or particle-to-substrate contrast is much lower, because their atomic number (13 and 14 respectively) and therefore also their backscatter yield is similar to the average atomic number of the calcium carbonate particles. The figure below shows that the backscatter coefficients for atomic number $Z < 30$ steeply increase, so the influence of the substrate's atomic number could indeed be high.

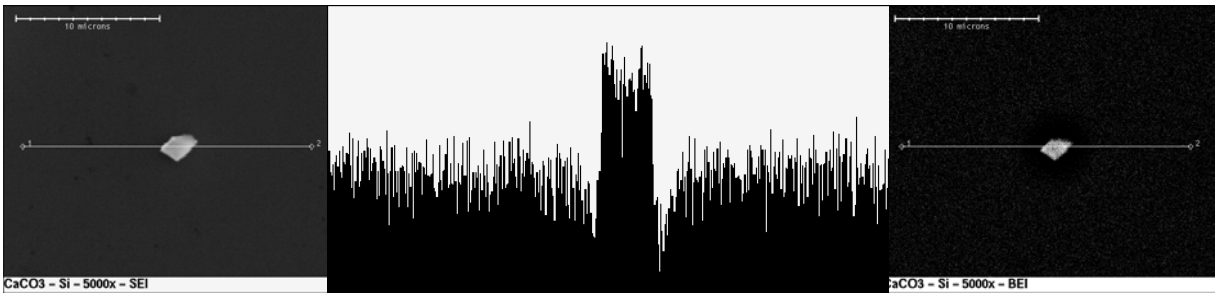

a) silicon

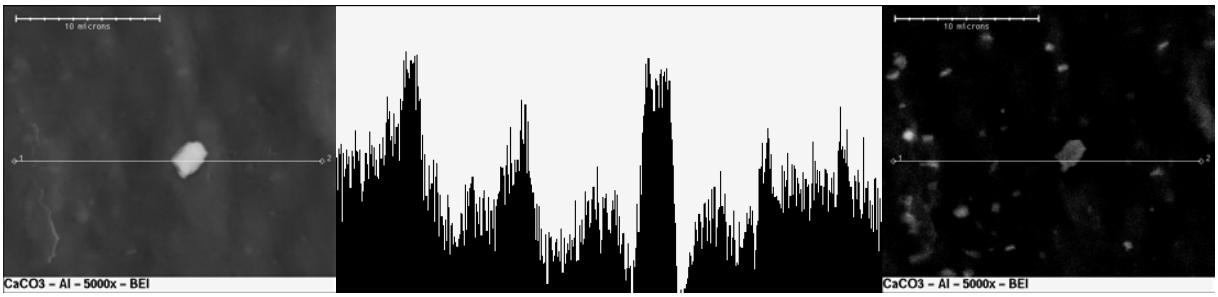

b) aluminium

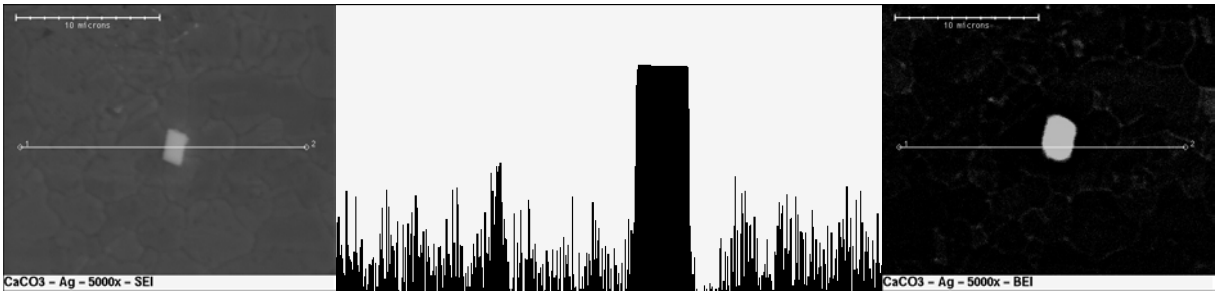

c) silver - inverse BEI signal

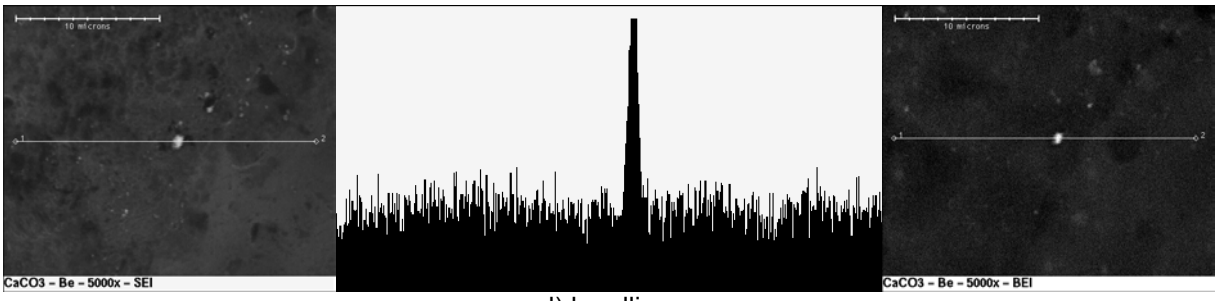

d) beryllium

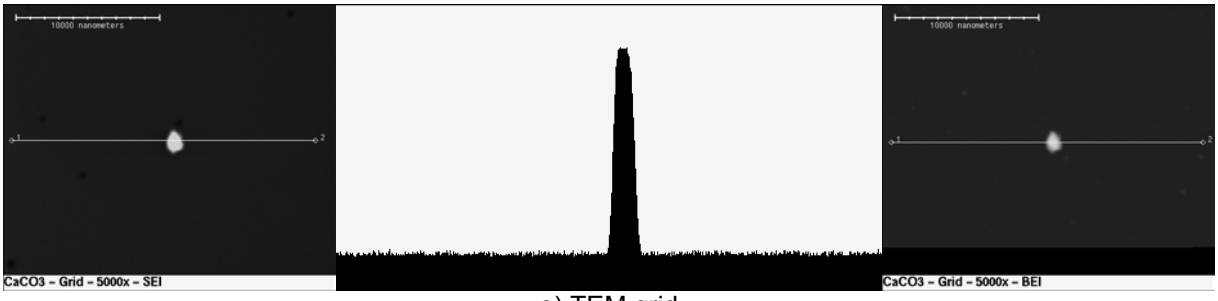

e) TEM grid

Figure 20: SEI, BEI line profiles and BEI of $CaCO_3$ particles

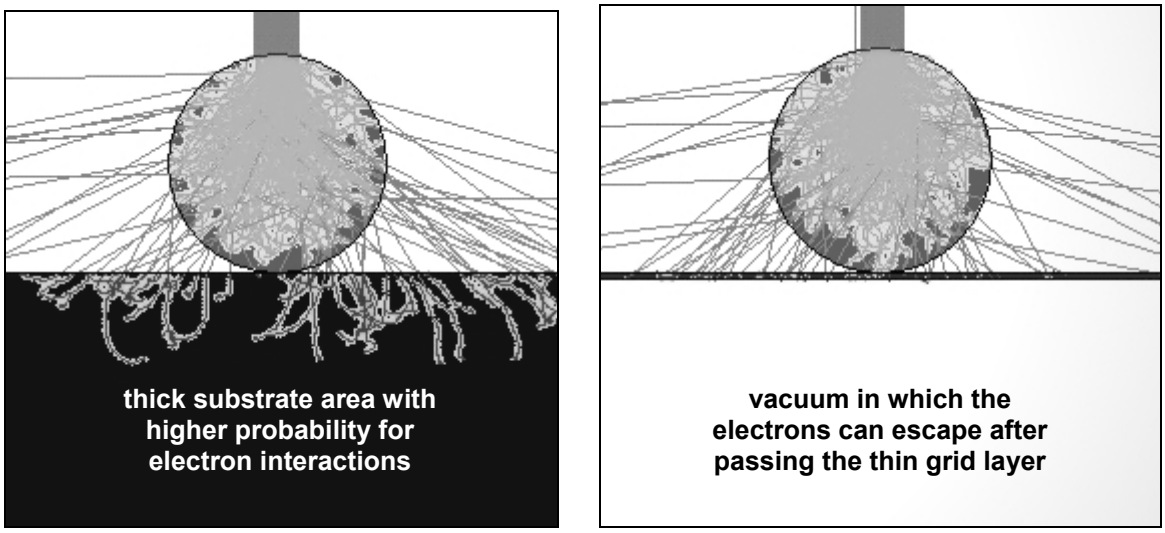

Figure 21: Simulated trajectories for a thick bulk (left) and a thin grid (right) substrate

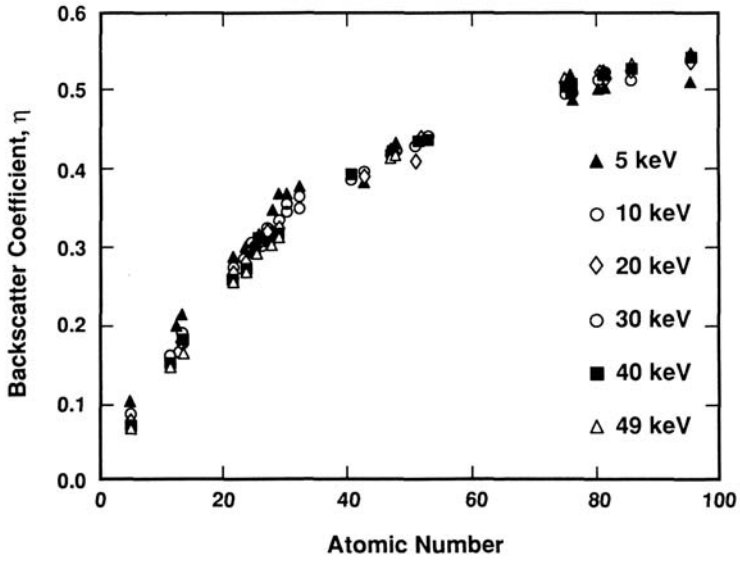

Figure 22: Backscatter coefficients as a function of primary energy and atomic number [3]

Earlier research on computer-controlled single particle analysis (SPA) determined that the **detection limit for the particle diameter** is typically around 0.2 µm. This value is of course dependent on the electron beam diameter, the particle-substrate contrast, the spatial image resolution and the magnification. The first aspect implies that the particle signals are overpowered by the substrate signals, if the irradiated particle is smaller than the electron beam. However, in case of TEM grids, the substrate signals are considerably lower than those for bulk substrates, resulting in much sharper particle signals. Therefore, the threshold value could be set much lower, and it should be possible to recognize particles with diameters < 0.2 µm. Indeed, we experienced that the SPA software was able to detect smaller particles (at least down to 0.05 µm). However, except for some images, we could not provide any evidence, because we did not dispose of suitable particle standards (in that size range).

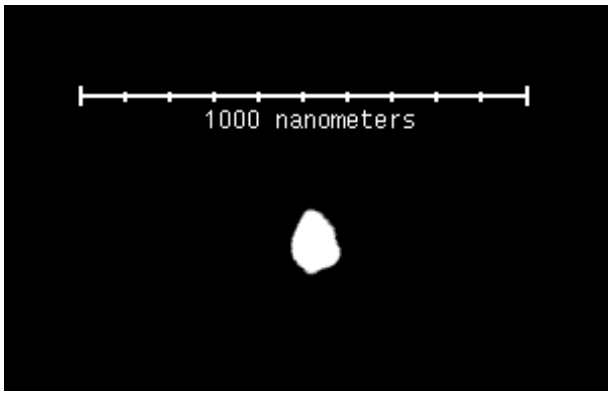

Figure 23: Particle ~0.1 µm on TEM grid (SEI left, BEI and line profile right)

Another option which was not discussed before is the use of the **secondary electron signal** to locate particles. This signal is much less related to the composition of the irradiated sample, but more to its topography. Therefore, in case of a very flat substrate, like silicon wafer, this option might also be considered. SEI could also be used in case of TEM grids, since the yield for secondary electrons in the thin layer is again very low compared to the particle, because most of the electrons of the electron beam pass through it before additional generation can take place. However, we experienced that the particle-substrate contrast in secondary electron images (SEI) is very sensitive to slight changes in electron beam current or to minor charging effects, so huge errors could be introduced compared to BEI, which appear to be more stable. It is also not easy to set a threshold value for particle recognition using the secondary electron signal, since the baseline or substrate signal is very rough.

The composition of the substrate is of course not only important for imaging, but also for **spectrum evaluation**. Although more aspects of spectrum analysis will be discussed later, the role of the substrate will be discussed here. The figure below shows the spectra for silver and aluminium foil, beryllium, silicon wafer and a TEM grid at an accelerating voltage of 10 kV and a beam current of 1 nA. The spectrum of carbon tape was also added to show the contrast with the TEM grid, which also contains carbon; both their spectra have been plotted with thick lines. The beryllium spectrum was plotted with a dashed line, while the spectra from the other substrates can be distinguished based on the indicated characteristic peaks.
It is clear that the TEM grid shows a smaller carbon peak than that of carbon tape, again because most of the primary electrons pass through it before generating any X-rays. The carbon peak height for the TEM grid is around 50 counts, while that of the carbon tape is 5000 or 100 times higher. The grid background is almost flat (no signal), except for some very small peaks which can be identified as coming from oxygen and copper. The latter peak originates from interactions of scattered electrons with the copper grid itself or with other parts of the specimen holder in which the grid is positioned during analysis.
Among the other substrates, beryllium clearly has the lowest background, followed by aluminium, silicon and finally silver. The background is related to the (average) atomic number, as described by Kramers.[49] The spectra of these metals clearly show a relatively small oxygen peak due to the presence of their corresponding metal oxide(s). Moreover, aluminium, silicon and silver have their own characteristic peaks. Especially the use of silver might be problematic, since it has a series of L-lines and M-lines, which might overlap with peaks of e.g. potassium and carbon respectively. Aluminium and silicon each show only one characteristic peak, but typical environmental particles like soil dust and sediments also contain aluminium and silicon, so it would be very difficult to quantify their concentrations.

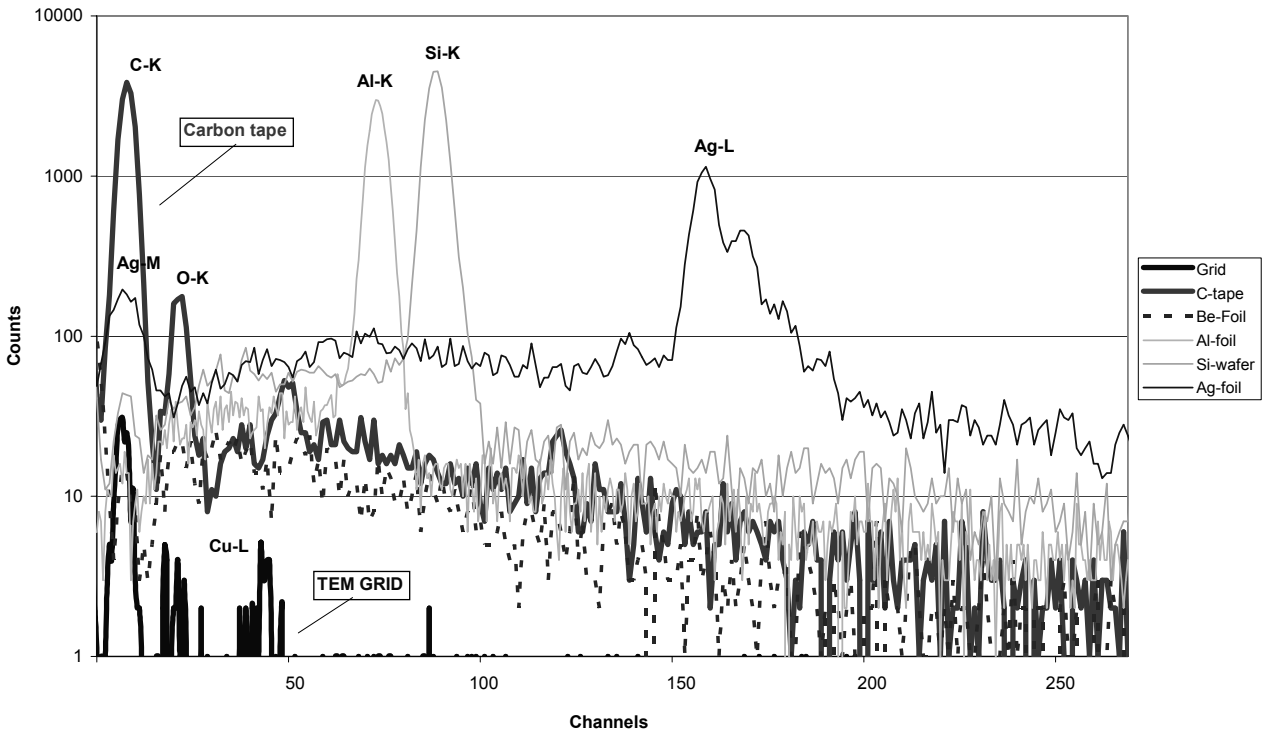

Figure 24: Comparison of substrate spectra

It must be pointed out that the spectral contribution of the substrates will be dependent of the size of the analyzed particles, the applied voltage and beam current. The spectra above were taken of pure spectra at an accelerating voltage of 10 kV and a beam current of 1 nA. Our next step was to evaluate the relation between the characteristic intensities of the substrate and the analyzed particle. Therefore, we have analyzed calcium carbonate particles of different sizes, prepared on the investigated substrates, using different voltages and currents.

The spectrum background and the characteristic peak intensities are known to be linearly proportional to the beam current. The higher the beam current, the more electrons will interact with the specimen, and the higher the absolute intensities will be. However, we never experienced that beam current variation resulted in huge relative differences in the influences of the substrates on the spectra. It is fair to say that beam current doesn't change the situation as explained above, so we decided to use a beam current of 1 nA for all our measurements. However, it might be useful to change the beam current in case of possible charging effects, of course on the condition that the same current is used for all measurements that are to be evaluated together.

On the other hand, the accelerating voltage and the beam diameter do cause different relative outputs. When a huge particle (> 10 μm) is bombarded with electrons, most of the interactions will take place inside the particle volume, so the influence of the substrate on the spectrum is expected to be low. When a small particle (< 1 μm) is irradiated, the number of interactions in the substrate will be increased. High accelerating voltages cause primary electrons to be much faster and to have a higher initial energy than electrons produced with lower voltages, so they will travel deeper into the substrate. This is shown for the different substrates in Figure 25, made from simulation data for calcium carbonate particles. The calculated, characteristic intensities for the different substrate and particle elements were plotted against the diameter (0.2-10 μm), and this for three different voltages (5, 10 and 20 kV). The Ag curves for silver represent the Ag-L intensities. The graph for beryllium substrate doesn't show any beryllium curve for obvious reasons; the carbon data in the graph for the TEM grid represents both the substrate as the particle intensity.

When looking at these graphs, it should be noticed that the intensity behaviour for the elements is similar for all **bulk substrates** (Be, Al, Si and Ag) at a certain voltage. For example, the trends in the graphs for 10 kV are similar for these substrates, since all curves appear to be parallel to each other. The huge advantage of beryllium is of course that there is no characteristic substrate signal, which simplifies the evaluation of the particle spectra. The substrate signal in case of Al, Si and Ag decreases for larger particle diameters, since electrons have to travel deeper to generate signals in the substrate. At a certain particle size (2-3 μm at 10 kV), the intensity suddenly even drops to zero. The influence of the substrate increases at higher voltages, resulting in the extension of the curve to the right, because the diameter at which the substrate signal drops to zero also increases. So by choosing relatively low voltages, the influence of high-*Z* bulk substrates could be reduced.
The higher the atomic number *Z* of the substrate, the lower is the substrate signal at 5 kV due to its higher backscattering coefficient. The higher amount of backscattered electrons results in additional interactions in the particles. The effect is less visible at 20 kV.
In the graphs we can also see the effect of the so-called overvoltage, which is the ratio of the primary electron energy (proportional to the accelerating voltage) over the critical energy for the generation of characteristic X-rays of a certain element. Since the critical energies for the all elemental peaks are known, the overvoltage is only determined by the primary electron energy, which is in return dependent on the accelerating voltage. If the voltage is set too low, peaks with higher critical energies will not be generated, since the beam electrons do not have sufficient energy to excite the atoms of the element in question. Therefore, in order to generate characteristic X-rays of a certain element, the overvoltage should be at least 1. The higher the value, the more substantial the X-ray generation will be. Therefore, all intensities are much lower at 5 kV, compared to its intensity at 20 kV. The intensities of calcium at 5 kV are relatively lower than those of carbon and oxygen, while at 20 kV the intensities are comparable (dependent of absorption effects). So the choice of the accelerating voltage not only determines the influence of the substrate on the spectrum, it also determines the analytical range, since the relative intensities of all characteristic X-ray peaks are dependent on it. On the other hand, the presence of high-*Z* peaks that interfere with low-*Z* peaks could be avoided by setting the voltage at a lower level. Therefore, a compromise should be found between the desired elemental range and possible interference effects. We decided that a voltage of 10 kV was ideal for the analysis of atmospheric particles, since the influence of most bulk substrates would be limited and the analytical range would extend to Fe based on the overvoltage for K-lines (though elements with higher atomic numbers could also be detected from their L- and M-lines).

As can be seen from Figure 25, the situation for **TEM grids** is different from that for bulk substrates, since the carbon curves obviously change towards lower particle diameters. This can be explained by the fact that this line represents not only the signal from the particle, but also that from the substrate. This has implications for spectrum evaluation and quantification. Recent papers by Laskin and Cowin suggest that TEM grids could be used for semi-quantitative single particle analysis of sub-micrometer particles when ignoring the carbon intensity coming from the grid itself.[50] These authors did not apply iterative Monte Carlo simulations, but a simple normalization method without particle size and shape corrections. However, they report relative errors of 15%, which is indeed not so bad taking into account the fact that they also analyzed very small particles down to 0.1 μm. Although the authors claim to have achieved results that are surprisingly better than their own expectations, they weaken their statements by saying that particles with a size of 0.1-2 μm can be 'reasonably' determined with their method. Therefore, their research raises some questions, which led us to do some more investigations on the subject.

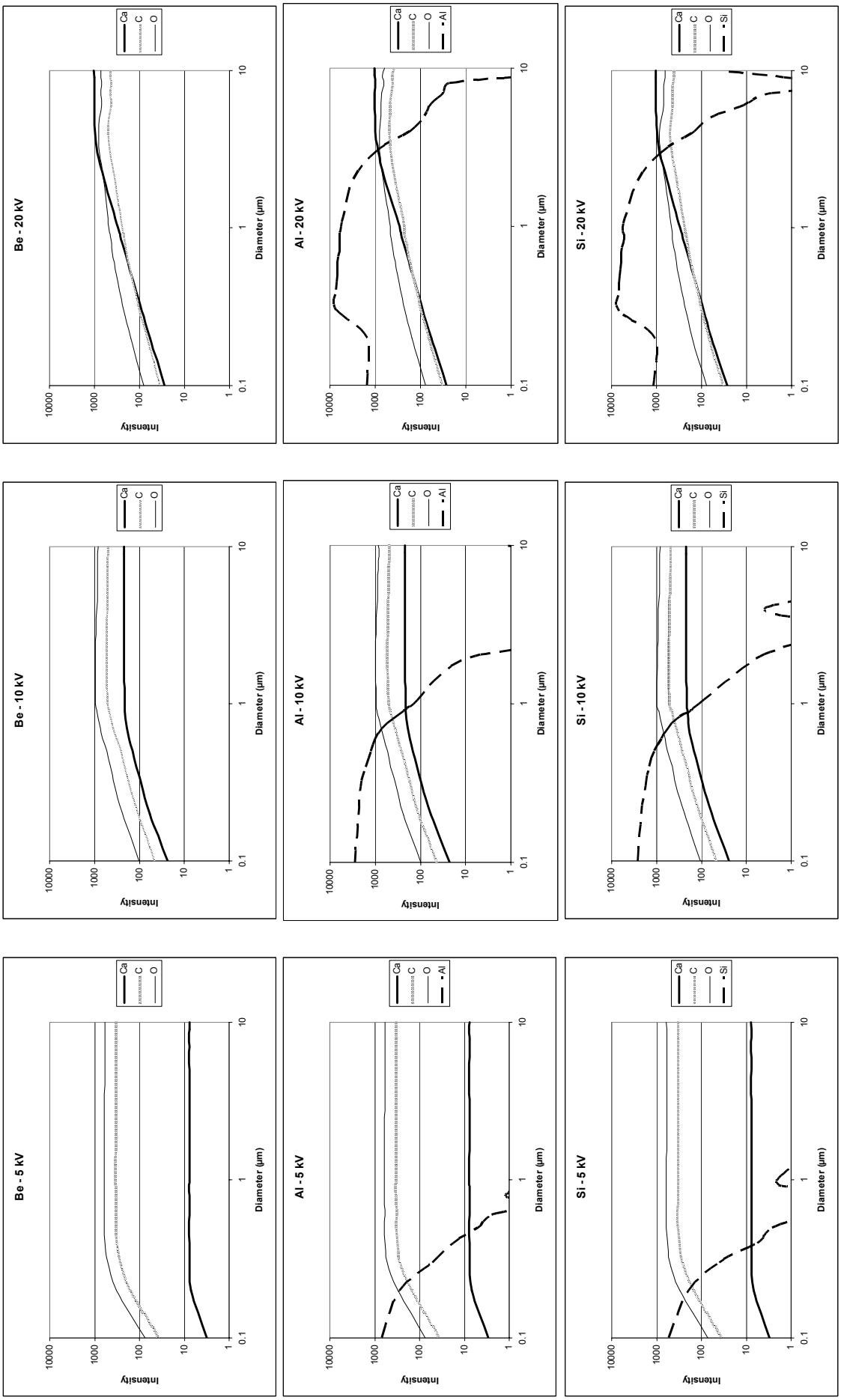

Figure 25: Simulation of X-ray intensities for $CaCO_3$ particles on different substrates at different voltages

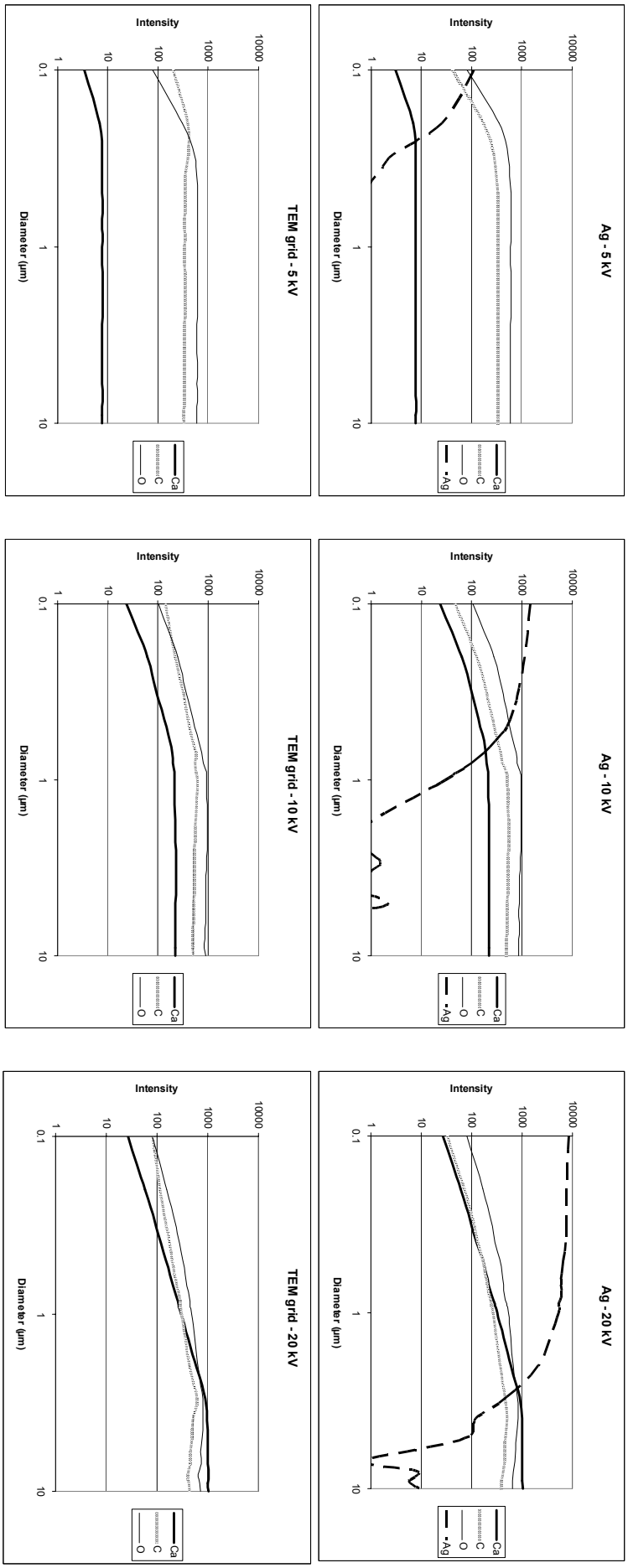

Figure 25 (continued): Simulation of X-ray intensities for $CaCO_3$ particles on different substrates at different voltages

From the spectra in Figure 24, we already concluded that TEM grids show very low characteristic and continuum contributions to the particle spectra; however, it is obvious from Figure 25 that the carbon intensity still increases for smaller particle diameters and higher voltages due to the influence of the substrate. So, is it indeed justified to ignore the carbon intensity of the grid?
The substrate contribution could of course be obtained from the Monte Carlo simulations, since it records which photons are generated in the substrate when calculating the carbon intensity. Therefore, we can split up the calculated carbon intensity into a substrate and a particle fraction. The graphs below show the carbon intensities at different voltages as a function of the particle diameter.

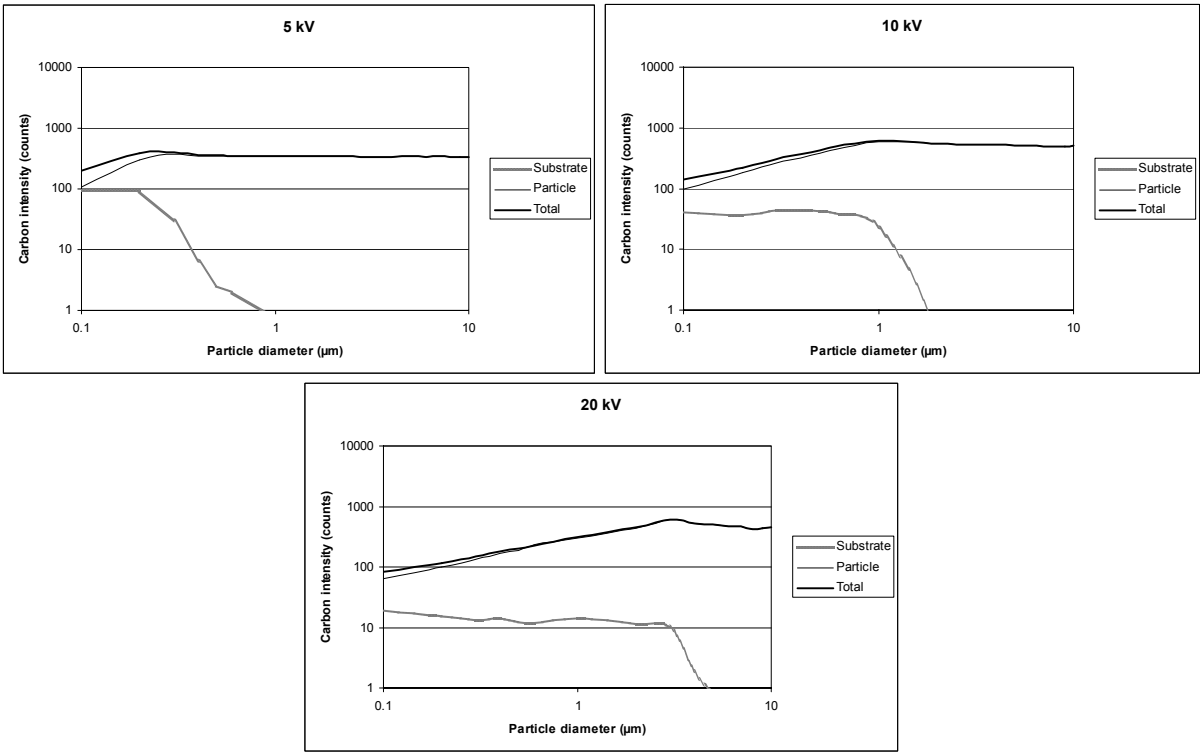

Figure 26: Calculation of the carbon intensity coming from the TEM grid layer (simulated)

It can be noticed that the substrate contribution to the carbon intensity may vary depending on the particle diameter. The overall pattern is that the curve starts high at the smallest particle diameter and gradually drops to zero at a certain, larger particle diameter. There is good agreement between the latter diameter value and the so-called Kanaya-Okayama electron penetration range R_{KO}:

$$R_{KO} = \frac{0{,}0276 \cdot A}{\rho \cdot Z^{0{,}889}} \cdot E_0^n$$

where A and Z are the average molecular weight and atomic number of the particle respectively; ρ is the particle density; E_0 is the primary electron energy; n is a constant in the range of 1.2 to 1.7. Indeed, in our case the minimum ranges (n = 1.2) are 0.91, 2.09 and 4.81 for 5 keV, 10 keV and 20 keV respectively, so these values quite closely match the particle diameters at which the substrate intensities drop to zero. This is to be explained by the fact that electrons are not expected to travel deeper into the sample than this range, so they cannot result in the production of X-rays beyond this distance (except indirectly by secondary fluorescence effects, but the so-called X-ray range is smaller than the electron range).

Although these data offer us additional information for future simulations, we still have a problem regarding the iterative quantification calculations, since it is impossible to know if the carbon intensity in a particle spectrum is coming from the substrate alone or from both the substrate *and* the particle. The solution suggested by Laskin and Cowin is to simply ignore substrate contributions to the spectrum, and assume that all carbon comes from the analyzed particle. As can be concluded from the graphs above for our specific experiment, the substrate contribution to the carbon intensity could be as high as 46%, 30% and 23% for a diameter of 0.1 µm at 5, 10 and 20 kV respectively. These contributions seem relatively high just to ignore them in the calculations. They also appear to drop to zero at a certain diameter depending on the applied voltage. Therefore, it seems impossible to determine a certain threshold intensity above which one could assume that the analyzed particles contain carbon.
Another problem cannot be overcome either: the influence of copper on the spectrum. Due to the side-scattering of primary electrons or due to secondary fluorescence, X-rays are also generated in the copper mesh of the grid or in the copper sample holder. This causes additional absorption and fluorescence effects which cannot be taken into account. High-accuracy calculations for grid samples would require precise grid geometry in the Monte Carlo simulations, which would make calculations extremely complicated. The simulations would also require the knowledge of the exact position of each analyzed particle relative to the surrounding grid structure and to the sample holder.

The study about the application of TEM grids for single particle analysis by TW-EPMA took place in the final stage of the doctoral project. Therefore, it was impossible to investigate any further possibilities to solve the problem. We are convinced that the solution will not be easy and will require complex simulations and corrections. On the other hand, some experiments with standard particles showed that ignoring the problem could result in relative errors up to 50% for carbon, depending on the diameter of the particle. Therefore, it appeared advisable not to use TEM grids, unless the analyst is sure the analyzed particles do not contain carbon (like for example, the standard NaCl particles used by Laskin and Cowin). Future developments of the quantification procedures for grid simulations might of course solve the problem, but at the time there is no real answer to the problems. TEM grids were not included in the experiments that are discussed hereafter.

It is worthwhile to mention that Windsor et al. at the National Institute of Standards and Technology (NIST) announced on their website that they have carried out experiments with self-developed boron substrates (Z=4) for particle analysis, though they have not yet published any results yet, as far as we know.[51] Boron would of course also be suitable for light element analysis for the same reasons as beryllium, with that difference that it is not as toxic. However, questions are raised when considering the brittle character of boron surfaces, so it would be very interesting to know how the researchers at NIST coped with this problem.

- **Beam damage and contamination**

Besides the direct contaminations that could be introduced during sample treatment and storage, two phenomena affect the composition of the sample during analysis by EPMA. As will be explained below, these phenomena are connected to each other and difficult to avoid without favoring another. Since the aim of EPMA is to determine the composition of the analyzed samples, it is important to assess their individual and combined effects.
The first phenomenon to be discussed here is generally known as '**beam damage**' or 'sample etching', which has been studied since long by many analysts. Glaeser defined it in 1979 as the removal of material 'by the synergistic action of electronic irradiation and certain residual gasses such as oxygen and water vapour'. This beam-induced loss of mass is indeed caused during electron irradiation, which is able to break chemical bonds, leading to the escape of volatile fragments and volatile reaction products (mostly from volatile materials of low atomic number). Especially TEM analysts had to face this problem, since they found that 20-30% of the mass of thin organic films could be lost under their electron beams. For TEM, this effect is of course quite critical, considering the limited amounts of sample to be analyzed. However, the problem is also clearly observed in conventional SEM images when the electron beam 'burns' the carbon coatings, and although analysis by EPMA could be defined as non-destructive for bulk analysis, beam damage should be taken into account when analyzing thin samples or small particles. One approach to the problem was to assume that both specimen and standards are affected in the same degree. Therefore, the problem could be dealt with in the *k*-ratio quantification schemes, since the intensities would also be affected in the same way. However, many scientists soon discovered that this assumption was not always correct, and they decided to use a method based on cryogenic cooling. In Cryogenic EPMA/SEM or TEM the samples are cooled down to low temperatures using special sample stages, and this is also the technique that we used in this study (see also previous chapter).[52] In our instrument, a stream of nitrogen gas flows through the stage, after it has been cooled down with liquid nitrogen (–193 °C).[53]

CONDITIONS	FIRST IMAGE	SECOND IMAGE
a) without cooling stage; imaging only	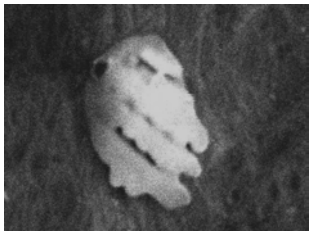	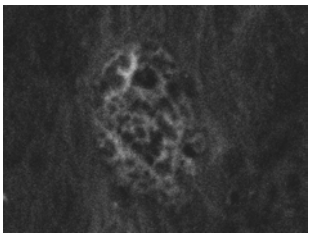
b) without cooling stage; before and after analysis	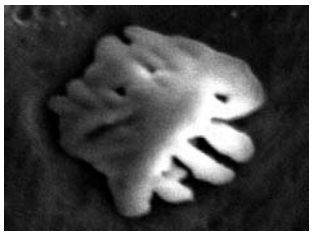	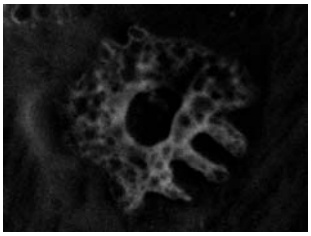
c) with cooling stage; before and after analysis	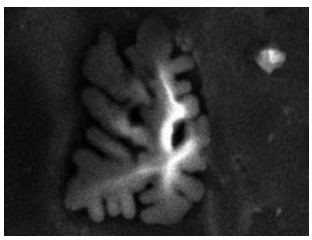	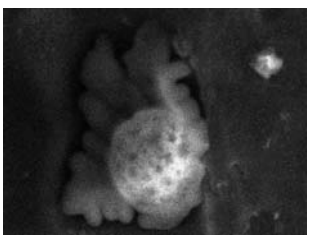

Figure 27: Images of ammonium sulfate particles before and after beam impact

As can be seen in the images above, our experience with cryo-cooling confirms the conclusions of earlier investigations by other researchers; stage-cooling by liquid nitrogen indeed substantially reduces and/or slows down the mass loss. Without the use of a cooling stage, beam damage makes the analyzed area appear relatively 'bleached' against the surrounding regions, and in case of volatile species, holes or craters can be formed. Small particles were even observed to evaporate at first impact during the initial image formation. When using a cooling stage, a sublimation or condensation process takes place during which the evaporating species are redeposited onto the substrate, undoing the formation of deep craters. However, the use of a cooling stage does not guarantee trouble-free analysis.

The second of the two phenomena influencing the composition of the analyzed samples could be described as '**beam contamination**' or the unintentional act of adding mass to the surface of the specimen during electron beam irradiation. [7,54] The earliest reference to this subject is probably untraceable, but Stewart's description from 1934 is a suitable starting point. He points out: 'In an evacuated tube in which the slightest traces of organic vapors may occur, … insulating layers are formed on surfaces subject to electron bombardment. These layers may be attributed to carbon compounds, and their formation is related to the polymerization or organic vapors …'. His analysis, as far as it went, remains unimpeachable today. The measurements that he carried out, had nothing to do with electron microscopy and were carried out at very low electron energies (200 eV), but during the following decades many practicing electron microscopists encountered the same contamination effects, especially from hydrocarbons. It must be pointed out that, although most of the contamination studies in the past focused on hydrocarbon sources, other molecules might also be causing the same effects. As (carbon) contamination layers were indeed observed on the specimen during irradiation, this did not mean that they could easily be explained, since the build-up behavior did not correspond to the other effect of beam damage to the specimen (removal behavior), even if it would be followed by redeposition. It was Ennos in 1951 who first suggested that the contamination was more related to vacuum-based contaminant sources: diffusion pump oil, vacuum grease, rubber gasket materials and unclean metal surfaces of the vacuum system. Therefore, the application of good high-vacuum practices was recommended, since (organic) molecules were found to be continuously absorbed onto the irradiated surfaces from the vapor phase. Cryoshielding was also suggested as a technique to decrease the rate of contamination build-up; in this method a so-called 'cold finger' (-80°C) is positioned near the analyzed surface to attract contaminating vapors. However, the sample surface itself was often found to be cooled down and started to act as a cold finger itself. For this reason, it appeared impossible to prevent beam damage and beam contamination at the same time, since the use of a cold stage to prevent the first phenomenon would favour contamination from the latter.

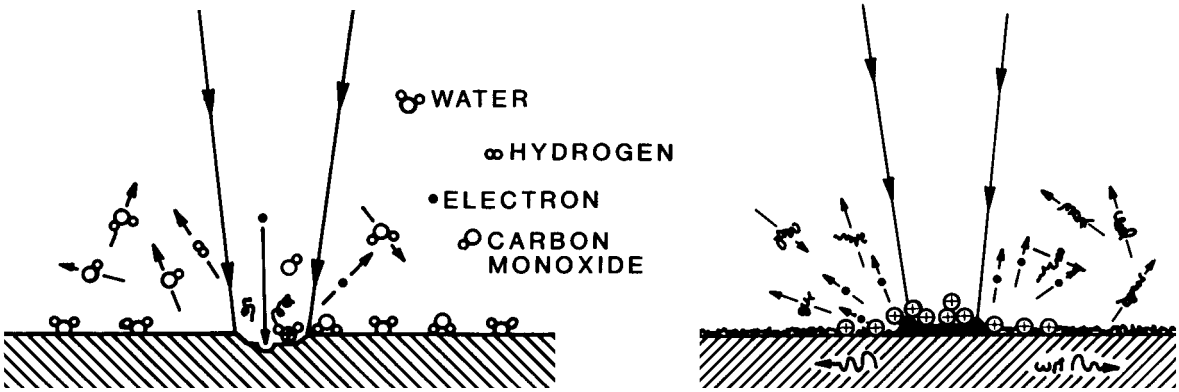

Figure 28: Beam damage (left) and contamination (right)

Research since the 1970's, when vacuum conditions were much better controlled, has enhanced the knowledge about **both effects**. The mechanism of beam *contamination* was found to consist of a mechanistic sequence: condensation of (hydrocarbon) molecules onto the surface, followed by surface diffusion, ionization, polymerization and reduction of these molecules to an immobile deposit. The main factors that determine its occurrence and magnitude are the electrical surface gradient (linked to the electron beam size and current) and the temperature gradient of the sample. The mechanism of beam *damage* consists of a similar sequence: the physisorption of potentially reactive gases (e.g. water vapour) which are 'activated' by electrons and will react with the specimen. In case of volatile specimen, the heat-up by the electron beam could of course also be enough to trigger evaporation without reactions with residual gases.
These descriptions show that the phenomena are linked to each other, making it difficult to avoid them both at the same time. A good vacuum is indeed required to get rid of the reactive gases and contaminating molecules, but a vacuum that is too high would also cause the immediate evaporation of volatile compounds in the specimen before electron impact. A cold stage would also work counterproductive for the vacuum system if it would redeposit or sublimate contamination molecules.

Besides these practical problems, we also had to face the problem of **quantification**. It would not be evident for our Monte Carlo simulations to take into account beam damage or contamination. For the mass loss effect, some researchers have found expressions for specimen heating (ΔT) in case of bulk samples as a function of the accelerating voltage V, the probe current I_p, the electron range R, the thermal conductivity λ_T of the irradiated material and the fraction f of the induced, homogeneously dissipated power that does not leave the specimen as secondary or backscattered electrons (typically 40-80%):

$$\Delta T = \frac{3 \cdot f \cdot V \cdot I_p}{2 \cdot \pi \cdot \lambda_T \cdot R}$$

However, we did not find any expressions for the heating of small particles and even if we would have, the main issue would still be how to simulate the eventual loss of mass. Processes like ionization have been studied since long, but they appear to be poorly reproducible and their effects are very difficult to predict (distortion of the particle shape and crater formation, composition changes due to reactions inside and outside of the particle, losses and sublimation, etc.). Therefore, our main conclusion was that quick and easy simulation solutions did not exist, and that we would have to concentrate on 'damage control' at the technical side of the problem. Experiments were carried out to investigate the effects of beam damage and contamination on quantification, and to find conditions for the optimal reduction of both.

As could be seen in the pictures in Figure 27, a **cooling stage** is absolutely necessary to prevent the evaporation of (semi-)volatile compounds, which are typical for atmospheric aerosols. So the first step in our study was to estimate the effect of beam damage on quantification when applying specimen cooling. Standard particles were made from some of these species, like ammonium and sodium sulfate or nitrate, but also droplets of sulfuric acid were tested. To investigate the effect of substrates on mass losses, the particles were prepared on aluminium, silicon, beryllium and silver. Our first, *qualitative* experiments showed that the process of beam damage is usually slow enough to follow as a drop in the characteristic-line intensity during analysis. This resulted in typical graphs like the following, showing the change in intensities of the elements after irradiation during consecutive periods of 20 seconds.

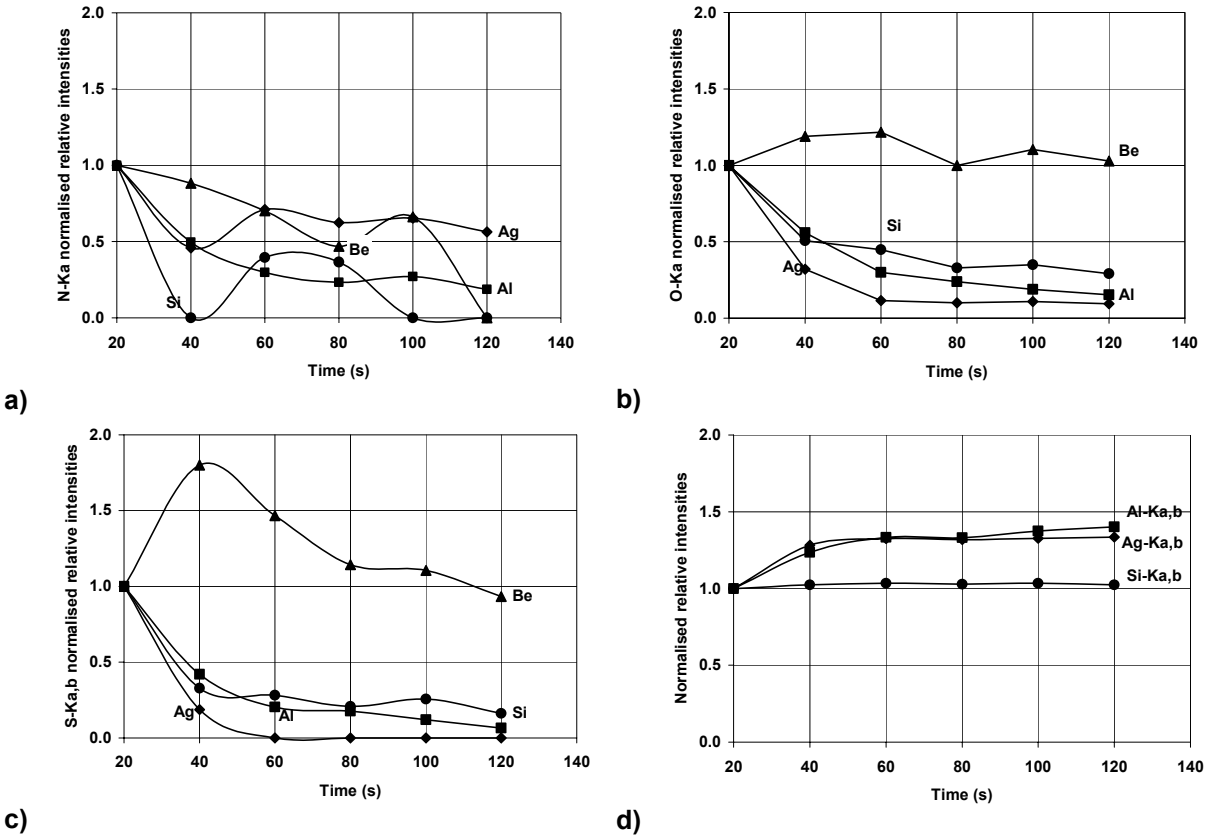

Figure 29: Intensity variation for 1µm-size $(NH_4)_2SO_4$-particles due to beam damage effects a) nitrogen, b) oxygen, c) sulphur, d) substrate

Here we only show the results for ammonium sulphate particles with a diameter of 1 µm.[39,53,55] The graphs for other sizes and beam sensitive compounds were published before in the doctoral thesis of A. Worobiec, and will therefore not be repeated here again.[56] As can be seen above, the intensities of the elements vary in time after subsequent exposure to the electron beam. The conclusion of our research about the qualitative analysis of beam sensitive compounds was that the damage effect shows different behavior depending on the compound involved, the particle diameter and the applied substrate. In our qualitative analysis (based on the X-ray intensities only), we decided that ideal behavior would correspond to stable relative intensities during irradiation. An overall order of increasing beam sensitivity could be given as follows: $NaNO_3$ < $(NH_4)_2SO_4$ < NH_4NO_3 < H_2SO_4 droplets. It was found that beam damage might not only depend on the sample temperature and on the analyzed compound, but also on the thermodynamic properties of the substrate, the backscattering coefficient of the substrate and the possible adhesive or chemical fixation of the particles to the substrate.
Comparison between the different substrates showed that beam damage is a complex phenomenon without a predictable, uniform behavior. Silicon appeared to produce the least stable intensity behavior of all substrates, maybe because its surface is quite flat and clean, so that adhesion or fixation processes have less chance to occur. On aluminium foil, big particles seemed more stable, which might be explained by a higher surface tension so that the collected particles are more spherical. Combined with its low backscattering coefficient, it appeared to be quite suitable for qualitative analysis. Beryllium was identified as the best collection substrate because, in theory, it has all the right physical and chemical properties. This was valid in the case of the sulphuric acid droplets; but somewhat less for $(NH_4)_2SO_4$ and NH_4NO_3, although the results were also very promising. Silver appeared less ideal compared to beryllium and aluminium.

The next, obvious step was of course to determine the magnitude of the beam damage effect on the *quantitative results*. For these experiments, we did not subsequently irradiate the analyzed particles, because this would not represent the real situation during analysis. The intensity variation over time gave a good indication of the substrate influence on the beam damage, but the irradiation time for particle analysis is typically 20 s. This irradiation time was set to 20 s after several considerations: 1) sufficient spectrum resolution requires some recording time, 2) the analysis time per particle should not be too long in view of automated analysis of large amounts of particles, 3) the longer the irradiation, the larger the beam damage.
Experiments were carried out with different beam sensitive compounds on different substrates under the following conditions: 10 kV accelerating voltage, 1 nA beam current, 20 s irradiation time, sample cooling at -193°C. This resulted in the graphs below (there are no data for sulphuric acid on aluminium due to the fact that we did not find any particles during analysis). The figures show the relative differences between the calculated and nominal (expected) concentrations for each of the elements of the analyzed compounds.

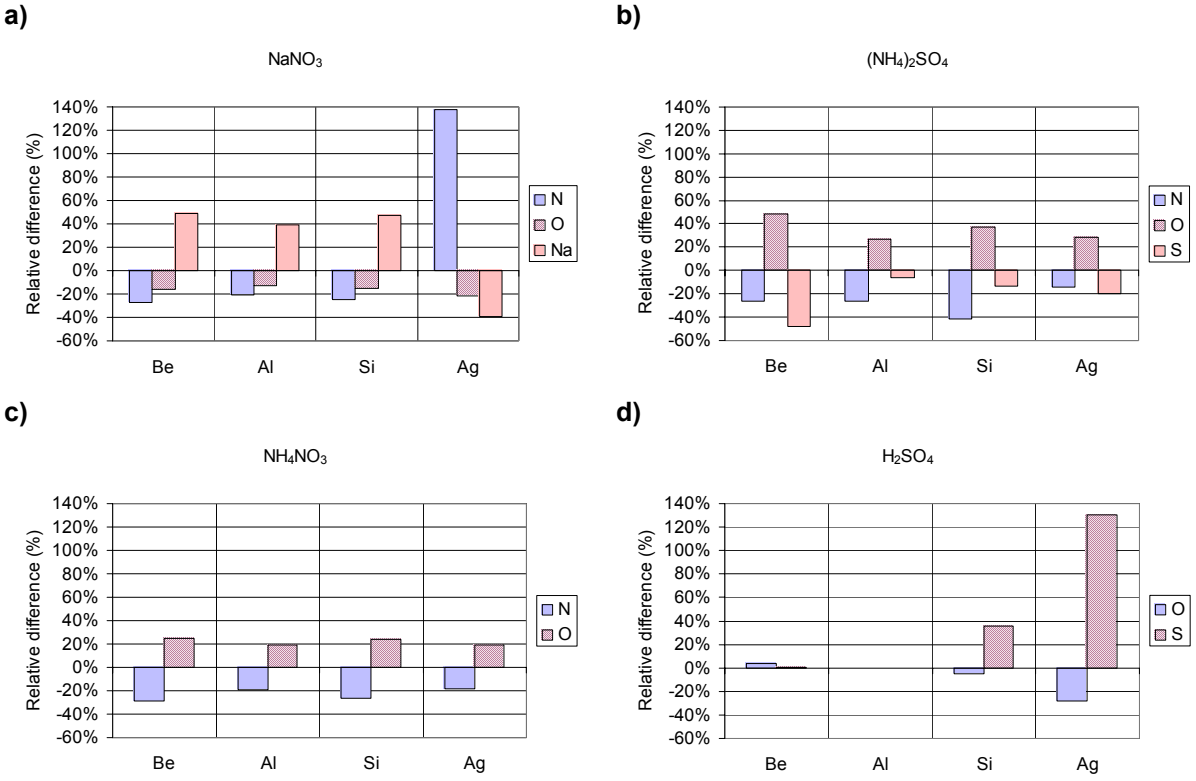

Figure 30: Relative difference from nominal concentrations for different compounds a) $NaNO_3$, b) $(NH_4)_2SO_4$, c) NH_4NO_3, d) H_2SO_4

In the graph for sulphuric acid, beryllium shows the smallest relative differences, while analysis on silver foil obviously overestimates the sulphur concentration to a high degree. The conclusion is completely different in the graphs for ammonium sulphate and nitrate, since the relative differences are smaller for silver than for beryllium. However, aluminium shows the lowest relative differences of all substrates in this quantitative comparison, which confirms its behavior in the qualitative comparison. Silicon shows quite good behavior, compared to the previous conclusions.

Having a better view now on the beam damage effects on both qualitative and quantitative analysis of several compounds, we can indeed conclude that it is a complex phenomenon. In view of *long term irradiation*, the ability of a substrate to dissipate accumulated heat and charges is very important. Therefore, the electron should be electrically and thermally conductive, which probably explains why silicon, as a semiconductor, did not score well in the qualitative analysis. A predictable property is then of course the electron backscattering, which determines how many electrons will pass through the analyzed particles, and therefore the exposure to charging and heating. In the quantitative analysis, the 20 s irradiation time is rather *short term*. This explains why the less predictable chemical and physical fixation effects might play a bigger role. Particles on aluminium clearly appeared more spherical and voluminous than on other substrates. Sulphuric acid is of course a strong reagent that can fixate itself to different substrates (especially in case of beryllium or its beryllium oxide surface).
It is very difficult to predict to what extent all these parameters affect the concentration calculations, but it is clear that evaporation losses and the deformation of the particle shape do result in relatively large errors. The overall effect on quantification results will be discussed more in detail in the 'top-down' evaluation, where we will compare our method with other methods by calculating the relative errors for different compounds (of which several are beam sensitive).

Other experiments were carried out to study sample **contamination**. We found that the subsequent irradiation of a certain spot could result in a raise in carbon intensity as high as 500 counts, which makes hydrocarbon contamination relevant. However, in case of short measurement times (20 s) the maximum raise is in the order of 10-50 counts, which could further be reduced if the cold stage is installed and turned on some time before the actual analysis and without the samples placed in the vacuum chamber. In this way, most of the residual hydrocarbons can be caught by the cold finger effect, before the sample is introduced into the machine. Of course there will still be a continuous build-up of hydrocarbons onto the sample, but we experienced that the carbon peak raise is relatively lower. Water is another contaminant that could be considered as a contaminant. All the adsorbed water on a sample will quickly freeze, increasing the oxygen concentrations during analysis. However, in some way, this could also be seen as an advantage, since the analyzed particles do contain water in their natural environment, so in fact one could say that the rapid cooling of the sample helps us to preserve the sample. As we will see in the next chapter, excess oxygen concentrations can partly be explained by the presence of water in the sample.
In literature, we found an application that is worthwhile mentioning here. Sullivan et al. report the use of a patented EVACTRON plasma device for the removal of hydrocarbons from samples in the vacuum chamber.[57] Using a radio frequency plasma, oxygen radicals are formed in a separate chamber and transported to the rest of the vacuum chamber by convection. The radicals etch away the hydrocarbons from the microscope interior through a reaction that forms CO, CO_2 and H_2O, which can be removed by the vacuum pumps. The authors claim to have successfully used the method for applications of semiconductor lithography inside electron microscopes, where even minor contaminations could cause serious defects. Whether the method is useful and effective for environmental samples was not investigated in their study.

- **Detector efficiency**

Standardless quantitative X-ray spectrometry needs accurate knowledge of the **detector efficiency function** in the analyzed range of X-ray energy.[3,58,59,60,61] A simple mathematical expression is generally used for conventional semiconductor detectors:

$$\varepsilon(E) = \exp\left(-\frac{\mu_W d_W + \mu_{Si} d_{inSi} + \mu_{Au} d_{Au} + \mu_{cont} d_{cont}}{\sin\phi}\right)\left[1 - \exp\left(-\frac{\mu_{Si} d_{acSi}}{\sin\phi}\right)\right]$$

where $\mu_W, \mu_{Si}, \mu_{con}, \mu_{ice}$ and $d_W, d_{inSi}, d_{con}, d_{ice}, d_{acSi}$ are the attenuation coefficients and the thickness of the different absorbing layers: window material (*W*), inactive (*inSi*) and active parts (*acSi*) of the Si crystal, conductive Au layer (*Au*) and window contamination (*cont*), respectively; ϕ is the angle between the plane of the detector window and the impinging X-ray beam. For low-energy X-ray detection (E<1.5 keV) the relatively thick (≈800-2500 nm) Be window of conventional Si(Li) detectors was replaced by materials having higher transmission, e.g. very thin windows produced from organic polymers (≈ 200 nm). The exact composition, structure and thickness of the polymer windows are not widely published, although these parameters are of great importance for the efficiency calculation, especially in the energy range 200 eV < *E* < 1 keV. Besides a fairly detailed description of our detector system, the manufacturer (Oxford Instruments Plc.) also provided us with transmission data for the window (which was made by Moxtec Inc.). [62,63] Although exact composition information was not supplied, literature data about comparable systems allowed us to assume that the main constituent elements of the polymer window material should be H, C, N and O. The manufacturer also indicated the presence of a silicon support grid and a thin aluminium layer for opacity. The efficiency function of the thin-window detector system had to be redefined as:

$$\varepsilon(E) = g \cdot \exp\left(-\frac{\mu_{Al} d_{Al} + \mu_{pol} d_{pol} + \mu_g d_g + \mu_{Si} d_{inSi} + \mu_{con} d_{con} + \mu_{ice} d_{ice}}{\sin\phi}\right)\left[1 - \exp\left(-\frac{\mu_{Si} d_{acSi}}{\sin\phi}\right)\right]$$

where *g* is the grid X-ray transmission (75%); $\mu_{Al}, \mu_g, \mu_{pol}$ and d_{Al}, d_g, d_{pol} are the attenuation coefficients and the thickness of the aluminium layer, silicon grid and polymer window.

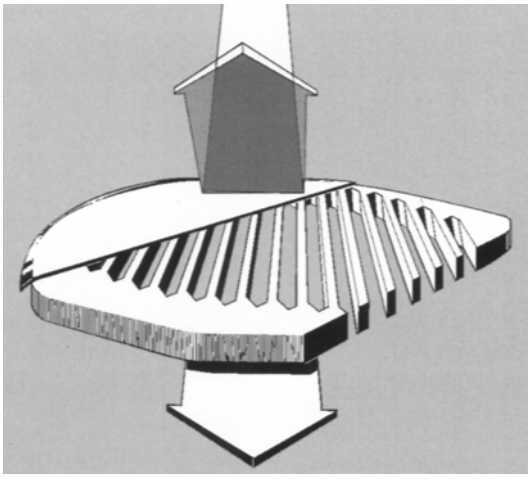

Super Atmospheric Thin Window (SATW)

Aluminium layer for opacity (~40 nm)

Polymer window (~300 nm)

Silicon grid (open area ~75%)

Figure 31: Moxtec window for Oxford Instruments EDX-detector

Our next task was to determine the exact composition of the polymer window. Procop proposed an indirect method based on the experimental determination of absorption edge parameters for C and O elements involved in the detector window.[58] Based on the discrete transmission data of the thin-window from Moxtec Inc., the weight fraction of the elements and the thickness of the absorbing layer were estimated using an iterative procedure. Taking into consideration the possible materials with different combinations of the practicable composition (such as Formvar, parylene or polyethylene), the optimal composition was found to be 8% H, 71% C, 21% O.[64] The optimized window parameters yielded the transmission function for low-*Z* elements; the calculated curve and the values given by the window producer are plotted below (right side).

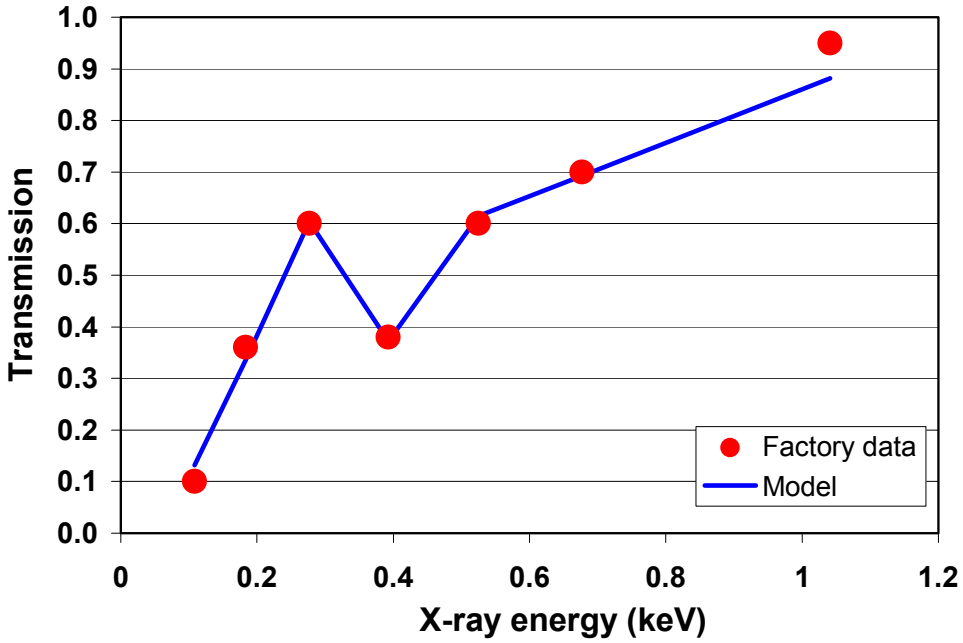

Figure 32: Transmission data for detector windows

Besides the polymer composition, another parameter in the detector efficiency function is much more difficult to estimate. The nitrogen cooled detector crystal acts as a cold finger, resulting in the formation of ice contamination on the detector window. This process of window contamination by sublimated residual gasses in the vacuum of the specimen chamber is rather unpredictable, and introduces an additional complication for our simulations.
However, we found that the process can be easily monitored by following the evolution in the spectrum quality. The formation of ice on the window of course results in the reduction of the X-ray transmission (represented by μ_{cont} and d_{cont} in the detector efficiency function) and in a clear intensity drop near the absorption edge of oxygen. So by watching the intensity behavior in the spectra from, for example, a bulk standard, it is very easy to monitor the process and even to determine the thickness of the ice layer on the detector window.
This is illustrated by the graph in, which shows recorded and simulated spectra of a calcium carbonate particle. The effect of the ice on the window can clearly be observed and simulated by our Monte Carlo routine. As explained in section 1.3 of this chapter, the parameterisation of Kirkpatrick and Weidmann was used to calculate the background continuum, and X-rays peaks were added by imposing a simple Gaussian peak shape model upon the generated characteristic intensities. Based on the simulation results, the coefficients in the detector efficiency function could be adapted, or the ice layer could be removed by using the detector 'conditioner'.

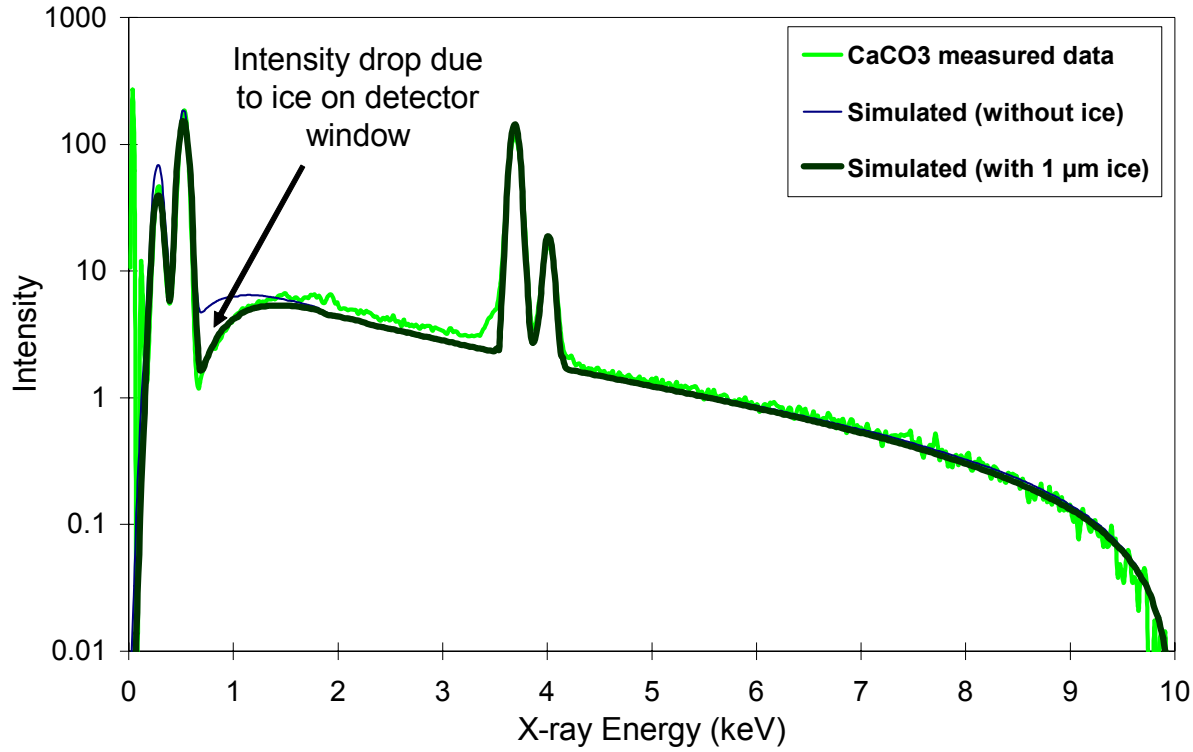

Figure 33: The effect of ice on spectra

The conditioning feature in our detector allows for a slow and temporary temperature increase near the detector window, resulting in the removal of the ice. This ice removal process requires a lot of time during which no measurements can be carried out, therefore, the first option will be preferred instead of frequent conditioning. However, it is our opinion that the regular use of a detector conditioner is essential, since the continuous build-up of ice on the detector window will eventually result in a dramatic intensity drop and inferior spectrum quality.
It is important to point out that the thin-window EDX-detector on our Jeol 6300 SEM is not equipped with a conditioner. The ice on this detector can only be removed by a special procedure in which a (freon) liquid is dropped onto the polymer window. Of course, this requires some skill and care in order not to damage the window. Moreover, the detector should best be warmed up first, which makes the procedure even more time-consuming than the conditioning feature in the detector system of our Jeol 733 EPMA. Therefore, we preferred using our EPMA for X-ray measurements in this study.

- **Spectrum evaluation**

To obtain at least semi-quantitative information on the chemical composition of each individual particle, the accurate determination of X-ray intensities is critical. The relatively poor energy resolution of energy-dispersive systems (EDS) creates problems when dealing with the proliferation of soft X-ray lines from heavier elements (L, M and N series), which are likely to interfere with the light-element X-ray peaks.[65] There are many overlaps possible, for example as much as 90 X-ray lines lie within 100 eV of the C-Kα line.[6] Similar situations exist for the other elements: Cr-Lα (573 eV) lies close to the O-Kα peak (525 eV), and Ti-Lα (452 eV) is difficult to separate from the N-Kα peak (392 eV). Coates has referred to ambiguities which can occur when M line overlaps are involved and pointed out the need for reliable data on the relative intensities of the spectral components.[66] He notes, in particular, that Mξ lines are often more intense than published data suggest. Problems may also arise from Si escape peaks, like the one associated with P-Kα at 274 eV, close to the C-Kα peak (277 eV), and that of S-Kα (at 568 eV) which interferes with the O-Kα line (523 eV).

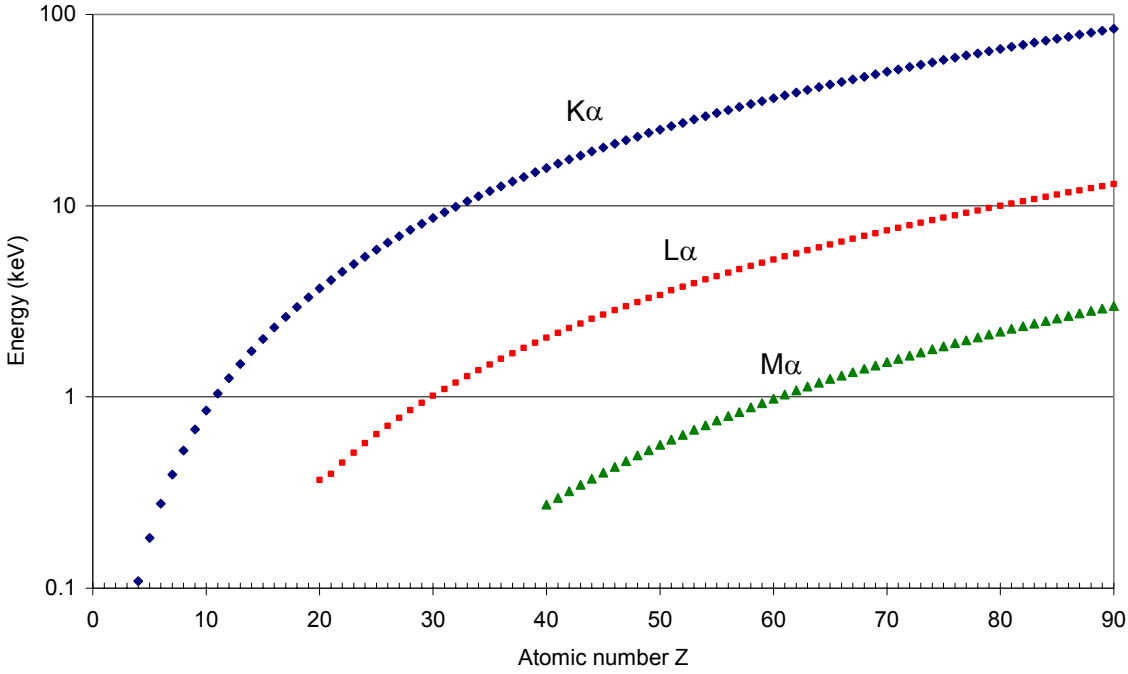

Figure 34: Characteristic X-ray line energies

The complex nature of the low-energy spectrum implies that some of the methods aiming to determine true peak intensities are not practicable. In the soft X-ray region some background subtraction methods may be prone to error. Continuum modelling has also some limitations. The prediction of the background shape is difficult in the low-energy region, because of the large absorption corrections required (also as a function of the particle geometry). The observed background is also distorted by the presence of spurious pulses produced by incomplete charge collection.[67] Mathematical filtering techniques avoid these difficulties, although curvature of the background at low energies may cause significant errors. The so-called "top-hat" filter method has been proven to be very useful in conventional computer-controlled EPMA for the on-line evaluation of spectra, usually having very poor counting statistics.[68,69] Because of the strong overlap of the characteristic lines, this method cannot be applied for thin-window EPMA spectra under 1 keV. Therefore, in this work the spectra were processed using a fitting algorithm developed by MiTAC.

AXIL, which stands for 'Analysis of X-ray spectra by Iterative Least-squares fitting', has been explained in many publications before, but a short description is appropriate. [70,71] The program employs a non-linear least-squares strategy using a modified Marquardt-algorithm to minimize the weighted sum of differences between the experimental data and a mathematical fitting function:

$$y(i) = y_{\mathrm{Cont}}(i) + \sum_{j\ \mathrm{Elements}} A_j \left[\sum_{k\ \mathrm{lines}} R_{jk} P(i, E_{jk}) \right]$$

For each fitting, a χ^2 value is determined to statistically evaluate the goodness-of-fit by comparing the experimental data and this mathematical fitting function. The fitting function itself consists of two parts describing the background continuum [$y_{\mathrm{Cont}}(i)$] and the characteristic lines [$P(i,E_{jk})$], where i is the channel number, index j runs over the line groups appearing in the spectrum, while k runs over all lines in group j, each line having a relative abundance R_{jk} and $\Sigma_k R_{jk} = 1$. A_j represents the total area of the characteristic peaks belonging to group j. $P(i,E_{jk})$ represents a peak function centred on energy E_{jk} that optionally also accounts for escape peaks. Assuming a Gaussian peak shape, the peak function can be written as:

$$P(i, E_{jk}) = G(i, E_{jk}) = \frac{Gain}{\sigma_{jk}\sqrt{2\pi}} \exp\left[-\frac{1}{2} \left(\frac{E(i) - E_{jk}}{\sigma_{jk}} \right)^2 \right]$$

where $E(i)$ is the energy of channel i, and σ_{jk} is the width of the peak with energy E_{jk}

$$E(i) = Zero + Gain \times i$$

$$\sigma_{jk} = \left[\left(\frac{Noise}{2\sqrt{2\ln 2}} \right)^2 + \varepsilon\, Fano\, E_{jk} \right]^{1/2}$$

The parameters *Zero*, *Gain*, *Noise* and *Fano* are optimized during the fitting procedure.
Peak shapes are modelled using Gaussian (G), Step (S) and Tail (T) functions, dependent on the peak energies. Tailing caused by incomplete charge collection in the detector crystal, can be taken into account using the applied fitting procedures.[72]

$$P(i, E_{jk}) = \mathrm{G}(i, E_{jk}) + f_S S(i, E_{jk}) + f_T T(i, E_{jk})$$

$$S(i, E_{jk}) = \frac{Gain}{2E_{jk}} \mathrm{erfc}\left[\frac{E(i) - E_{jk}}{\sqrt{2}\sigma} \right]$$

$$T(i, E_{jk}) = \frac{Gain}{2\gamma\sigma \exp\left[-\frac{1}{2\gamma^2} \right]} \exp\left[\frac{E(i) - E_{jk}}{\gamma\sigma} \right] \mathrm{erfc}\left[\frac{E(i) - E_{jk}}{\sqrt{2}\sigma} + \frac{1}{\sqrt{2}\gamma} \right]$$

The functions are normalized, i.e. the integral of the function over the spectrum equals unity. The parameter γ is an extra non-linear parameter, modelling the width of the tail.

In order to extend the capabilities of non-linear least-squares fitting at low energies, the procedure was optimised by Prof. Dr. Van Espen for **accurate modelling** of the characteristic X-ray peaks and the Bremsstrahlung background below 1 keV. The appropriate mass absorption coefficients were taken into account, and the parameters of the detector window, derived from our model described in a previous section, were used for modelling the continuum background and the relative abundance of the characteristic lines in the same line group. The spectral distortions caused by incomplete charge collection in the detector crystal were also modelled in the peak functions as tail and step functions. The incomplete charge collection is most pronounced at low energies, and can also cause that the energy calibration becomes non-linear in the low-energy range.[73] Therefore small deviations from the assumed linear energy calibration were allowed during the fitting procedure.
To test the optimised procedure, standard particles were prepared from *pro analysis* grade solid chemical compounds and standard reference materials. The grains were ground to microscopic size using an agate mortar. Chemical compounds showing overlapping characteristic X-ray lines under 1 keV were selected, such as $CaHPO_4$, $CaSO_4$, KCl, K_2SO_4, Fe_2O_3, $HgCl_2$, Na_2SO_4, NaF, NaCl and algae (IAEA-413). Figure 35 shows the fitting of four typical particle spectra collected by thin-window EPMA.

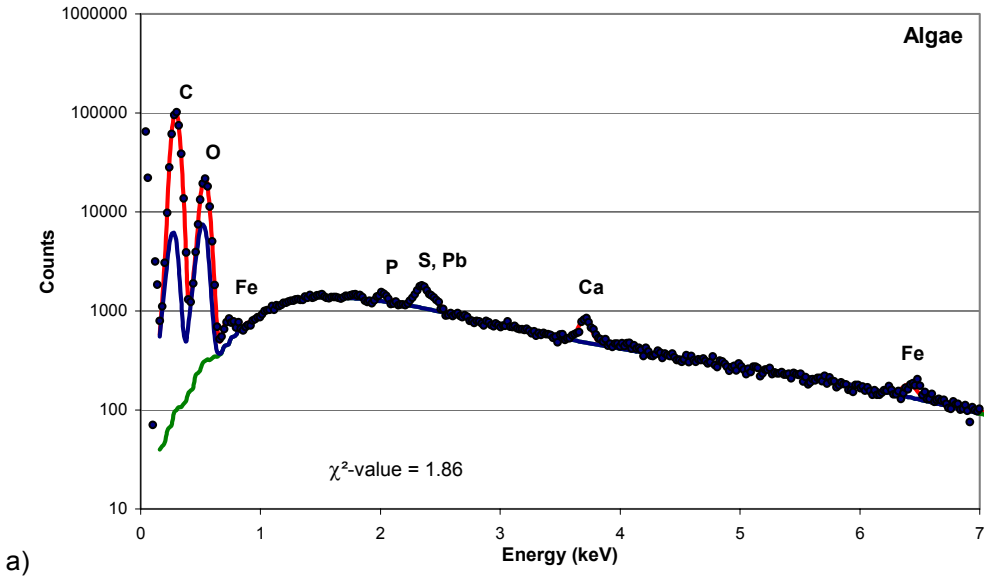

a)

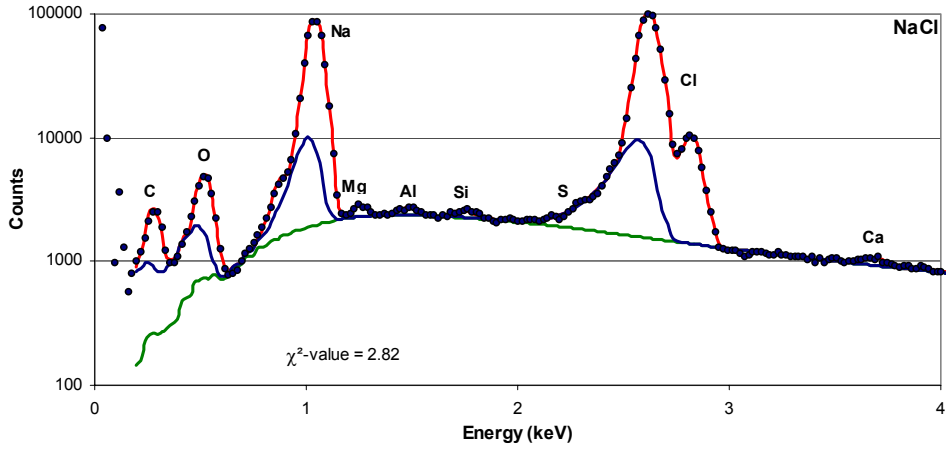

b)

Figure 35a-b: Fitted spectra of particles from compounds with typical overlap problems

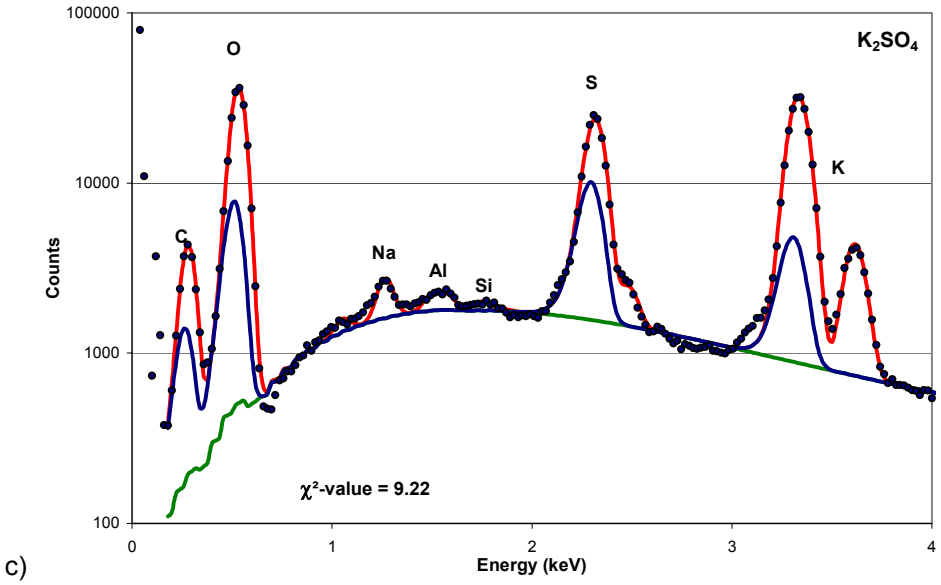

c)

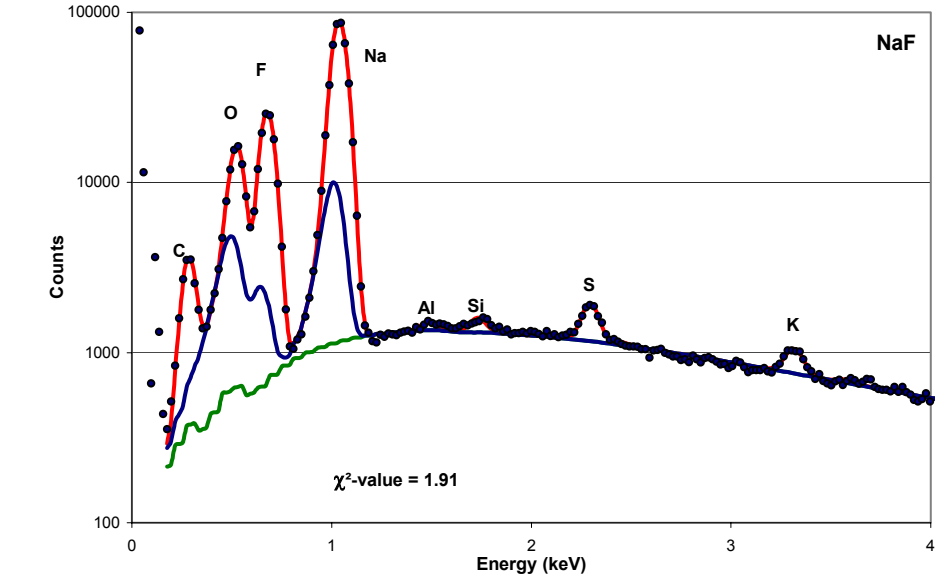

d)

Figure 33c-d: Fitted spectra of particles from compounds with typical overlap problems

The contribution of the tailing effect was found to be around 10 % of the total area of the characteristic peaks. The agreement between the fitted functions (top line) and the experimental data (dots) is good, yielding quite low χ^2 values that are below two for three of the spectra. The goodness-of-fit for the spectrum of K_2SO_4 is somewhat worse (χ^2 = 9.22) because of the small difference at the low-energy side of the K-Kα peak. The fit for this spectrum is still reasonably good, since the χ^2 values were found to be over 1000 assuming only a Gaussian peak shape.

Characteristic L lines of heavier elements can strongly overlap with K lines of C, N and O. For example, Ca-Lα at 0.341 and Ca-Ll at 0.302 keV affect the determination of the C-Kα intensity at 0.277 keV. Also, K-Ll at 0.259 keV is very close to the C-Kα line; the difference is just 18 eV. The same problems occur when Ti and N, Cr and O or Fe and F are present together in the particle. This poses a serious problem for spectrum fitting, and therefore also for our quantification method.

The non-linear least-squares fitting of the spectra is a statistical procedure, therefore it cannot resolve X-ray lines which are very close to each other. If both lines are added to the fitting model, it is possible, that the statistically best fit is not realistic, since the resulting area of one peak is a high positive number and a high negative number for the other peak. Therefore, in this case the possible solution is to include only the C, N and O K-lines in the fitting model, and then correct the intensities by subtracting the intensities of the overlapping L lines, using **L/K intensity ratios** and the corresponding K intensities. Another possibility is to regard the K and L lines for heavier elements as one group in the spectrum fitting model, using pre-set L/K ratios. From measured spectra of standard particles, which do not show strongly overlapping X-ray lines (e.g. $CaSO_4$, $CaHPO_4$, TiO_2 and Fe_2O_3), one can see that the detected L/K ratios are not constant; they are dependent on the size and the composition of the particles. It was previously illustrated that the entire X-ray spectrum can be accurately modelled by Monte Carlo simulations, in a good agreement over a wide size range (0.3–10 μm in diameter). For this reason, our Monte Carlo program was used to simulate the L/K ratios for the element range of Ca–Zn, for different particle diameters and concentrations of the element of interest. A spherical particle shape and a carbon matrix were assumed for the simulations. All of the calculations were done for a 10 kV accelerating voltage, because the routine light-element analysis of particles is normally carried out at this exciting energy.
Figure 36 shows the simulated L/K ratios for six elements, as a function of their weight fraction and particle diameter. In general, for small particle diameters, the concentration dependence of the L/K ratios is very weak. In the case of large particles, however, the ratio can show strong concentration dependence (a factor of 10 for Ti, 3.5 for Cr and 2 for Fe and Ca), while the L/K ratio of Zn is almost constant at 10 μm diameter for a wide concentration range. The behaviour of the Fe L/K ratio is quite complex, it is not a monotonic function of the particle diameter and also not a monotonic function of the Fe concentration for particles larger than 1 μm.

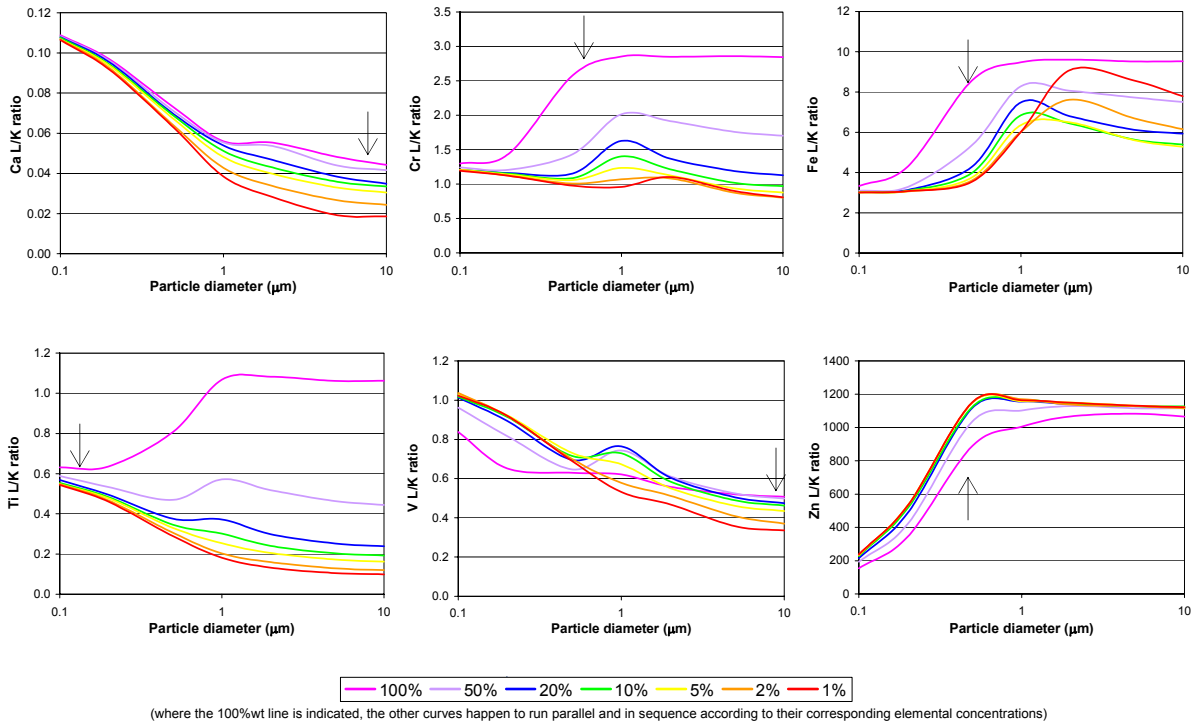

Figure 36: Calculated L/K ratios for six typical elements in a spherical carbon matrix

For a clearer understanding of the behaviour of the L/K ratios as a function of particle diameter and concentration, Figure 37 shows the simulated Fe-Lα and Fe-Kα intensities normalized to the maximum, for two values of Fe concentrations (1 and 20 wt%). The general trend for higher energy X-rays (e.g. Fe-Kα) is, that the intensity increases with particle diameter until the interaction volume is as large as the particle volume, and remains constant for higher diameters. However, for low Fe concentrations, the absorption effect of the matrix is more pronounced, therefore the intensity reaches its maximum more slowly and a decrease can be observed at higher particle diameters. Low-energy X-rays (e.g. Fe-Lα), however, are generated deeper and in a shallower region, therefore, the absorption effect becomes much more important. The intensity maximums are shifted towards the higher particle diameters. The concentration effect is similar to that observed for higher energy X-rays, but even more pronounced. The differences in particle size effect, matrix effect and absorption effect are the factors determining the behaviour of the Kα and Lα intensities themselves, which result in differences in the L/K intensity ratios for different elements.

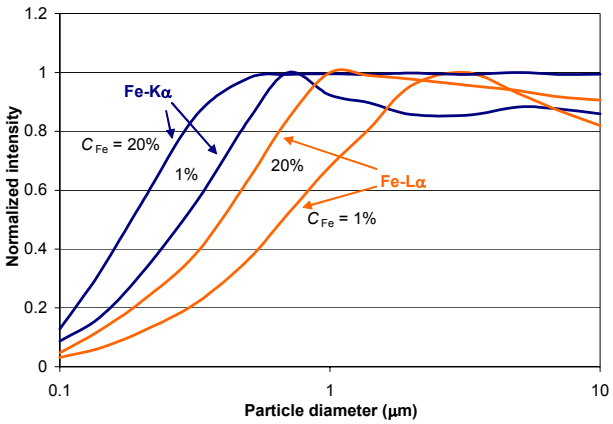

Figure 37: Simulated Fe-Lα and Fe-Kα intensities for Fe concentrations of 1 and 20 wt%

A comparison of measured and simulated Ca L/K ratios is shown in Figure 38 for $CaSO_4$ and $CaHPO_4$ particles. Although the measured data are quite scattered, reasonable agreement can be seen between the measured and simulated ratios for a wide range of particle diameters. The general trend of the measured and simulated data suggests that the simulated L/K ratios can be reliably used for the correction of the overlap of close-lying X-ray peaks.

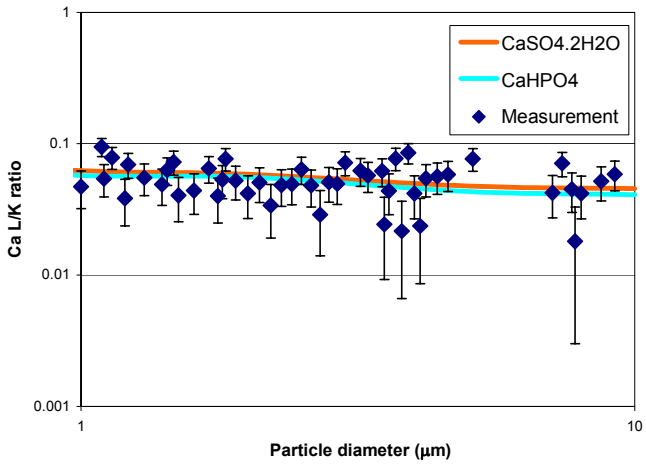

Figure 38: Ca L/K ratio for $CaSO_4$ and $CaHPO_4$ particles

The **correction procedure** for the strong peak overlaps is the following: first the X-ray intensities are determined using non-linear least-squares fitting of the spectra, with a fitting model containing only K lines below 0.6 keV. As a second step, the elemental concentrations are estimated from the calculated intensities. These estimated concentrations are then used for the simulation of L/K ratios, for the appropriate correction of the C, N and O Kα intensities. The final concentration values are obtained from the corrected intensities in a second run on our Monte Carlo simulator. The correction of the intensities can be done by simple subtraction or by the spectrum-fitting program itself, regarding the K and L intensities as one group, using the simulated L/K ratios iteratively.
As an example, Table 2 shows the comparison of the nominal (C_n) and calculated (C_c) average concentrations for K_2CrO_4 and $CaCO_3$, calculated with and without taking into account the strong spectral overlaps using the simulated L/K ratios. The sources of the standard deviation of the average calculated concentration (σ_c) are the fluctuations in the shape and size parameters of the particles. The relative differences in averages between the nominal and calculated concentrations, $\Delta = |C_c - C_n| / C_c$, are shown in the last column of the table.

Table 2: Evaluation of peak overlap corrections

		without corrections			with peak overlap corrections		
K_2CrO_4	C_n (in %)	C_c (in %)	σ_c	Δ (in %)	C_c (in %)	σ_c	Δ (in %)
C	0.0	2.5	0.3	---	0.0	0.0	---
O	26.9	35.4	3.7	31.6	28.8	5.6	7.1
Al	0.0	0.3	0.02	---	0.3	0.02	---
Si	0.0	0.1	0.01	---	0.1	0.01	---
K	43.9	37.4	2.4	13.6	42.9	3.2	2.3
Cr	29.2	24.4	1.6	16.4	27.8	2.3	4.8
$CaCO_3$	C_n (in %)	C_c (in %)	σ_c	Δ (in %)	C_c (in %)	σ_c	Δ (in %)
C	12.0	12.6	1.0	5.0	12.0	1.1	0.0
O	48.0	49.2	3.0	2.5	49.9	2.9	4.0
Ca	40.0	37.5	3.6	6.3	38.1	3.6	4.8

In the case of K_2CrO_4, the total C-K intensity was regarded as K-Ll, since C is not present in the particle. The O-Kα intensities were corrected using the simulated L/K ratios and the Kα intensities of Cr. The improvement of the concentration calculation is significant. Without the corrections, all of the Δ values were above 10%, with the worst value for O being above 30%. By taking into account the spectral overlaps, the Δ values became less than 10% for all of the elements present in the particles.
For $CaCO_3$, the improvement is less striking, but still significant. For particles containing heavier elements having X-ray lines overlapping with K lines of low-*Z* elements at low concentrations, the intensities obtained without peak-overlap correction can be used for the quantification; the contribution of the L or M lines to the low-*Z* element intensities can be neglected in this case.

So, as a **summary** or **conclusion**, we could say that we managed 1) to extend the capabilities for non-linear least squares fitting at low energies, 2) to simulate L/K intensity ratios for elements Ca–Zn, 3) to take into account strong spectral overlaps under 1 keV. Using the improved least-squares procedure for the fitting of typical particle spectra, the χ^2-values for evaluating the 'goodness of fit' are indeed found to be sufficiently low, including the X-ray lines below 1 keV. The peak overlap correction based on simulated L/K ratios improves the calculated concentrations significantly. The proposed correction method is able to handle the strong spectral overlap between L lines of heavier elements and light-element K lines, despite the relatively poor energy resolution of the currently used semiconductor detectors. Despite the successful achievements, we should point out that some more work could be done to improve the quantification procedure even more.

As was explained in the first chapter, future applications of microcalorimeter detectors could simplify the handling of the energy-dispersive X-ray spectra in the low-energy range, since their energy resolution is comparable to that of wavelength-dispersive systems. In the meantime, however, we have to manage with all the means that we have to our disposal.

Although the modified version of WinAxil showed to be quite successful, the fact that the fitting of the Bremsstrahlung background is rather complex and requires manual iterations by the user, could be seen as a disadvantage. Therefore, we preferred another version of Axil, in which only a purely mathematical type of background fitting can be selected, but in which tailing corrections are also included.[71] The selection of a correct model for the continuum also requires some skill and takes some time, but the procedure as a whole is less complex. However, if the WinAxil version with the modified Bremsstrahlung model would be improved and made easier to handle, it would certainly add some more accuracy to the fitting.

The same comment could of course be made about the Monte Carlo corrections using L/K-ratios. First of all, the applied correction procedure was only used in a single run, while in fact an additional iteration loop should be introduced in the quantification algorithm. The selected L/K-ratio is of course dependent on the composition of the sample, which is also the unknown to be determined. After the first correction, new concentrations are determined which could be used to re-evaluate the overlap correction using another L/K-ratio. A second shortcoming is the fact that our peak overlap correction procedure cannot be performed automatically. However, since many overlaps are possible between peaks from a variety of elements, it would be an immense task to develop a database containing the different L/K-ratios for all of these overlaps and for different concentrations, matrices and particle sizes. Therefore, an additional routine could be developed to incorporate the correction procedure, i.e. calculating the L/K-ratio for a given particle size and estimated elemental concentrations. However, both of the suggestions above to obtain automated and iterative peak overlap corrections would require substantially more processing time, which is the reason why we did not implement them.

- **Physical functions and expressions in the simulation procedure**

The main motivation for Hovington et al. to develop the complex simulation CASINO code was the lack of models that describe the electron-solid interactions and to generate all possible electron and X-ray signals in the low-energy range $0.1 < E < 15$ keV.[34] With the arrival of FEG-SEM and energy-dispersive X-ray detectors for low-energy signals, there was great demand for such models, also within MiTAC (see previous chapter). The freely available CASINO routines were adapted in our institute to enable it to model different particle shapes, as was also explained before. CASINO provides its users with many options for selecting physical functions or expressions that are used in the simulations, as shown in the table below.

Table 3: Available functions and expressions in CASINO

	AVAILABLE MODEL	*INFO*
Elastic cross section	Rutherford (1911)	Limited to high-E
	Mott (1949)	Also low-E
	Mott: Gauvin and Drouin (1993)	Parametrization
	Mott: Drouin et al. (1997)	Experimental
Ionization cross section	Gryzinski (1965)	
	Powell (1976)	
	Casnati (1982)	
	Jakoby (1987)	
	Pouchou and Pichoire (1991)	
	Gauvin (1993)	
Stopping Power	Bethe (1933)	Limited to high-E
	Joy and Luo (1989)	Extended to low-E
	Hovington et al. (1997)	Experimental
Random number generator	Press et al. (1992)	Period 2^{62}, fast
	Marsaglia and Zaman (1994)	Period 2^{125}, slow
Mass absorption coefficients	Henke and Ebisu (1974)	Low-E
	Heinrich (1986)	High-E

The well-known critical parameters in regard of low-energy simulations are of course the stopping power and the energy loss. The Bethe (1930) function for the stopping power was corrected by Joy and Luo (1989) to extend the energy range, since they noted that at low beam energies the energy loss goes through a peak, decreases and even becomes negative, which is physically unrealistic.[74,75]

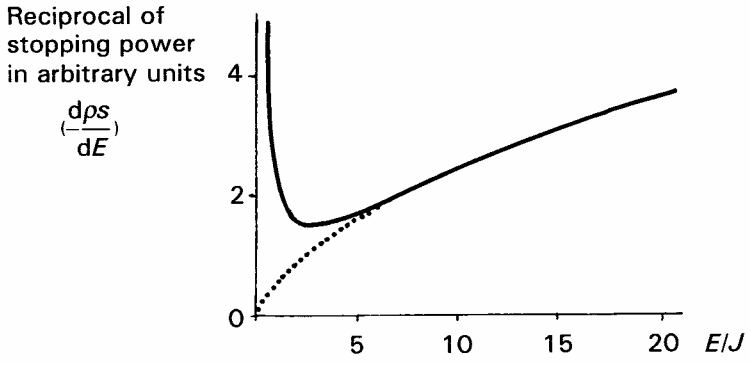

Figure 39: Comparison of energy loss expressions at low energy (Bethe ···· vs. Joy-Luo —)[3]

Another critical aspect of the simulations is the elastic cross section. Although the Rutherford (1911) expression is accurate for high-energy interactions, it fails at low energies because it is based on the first Born approximation, which is not valid < 10 keV.[76] The Rutherford theory should then be replaced by the Mott theory, as worked out by Czyzewski et al. (1990).[77]

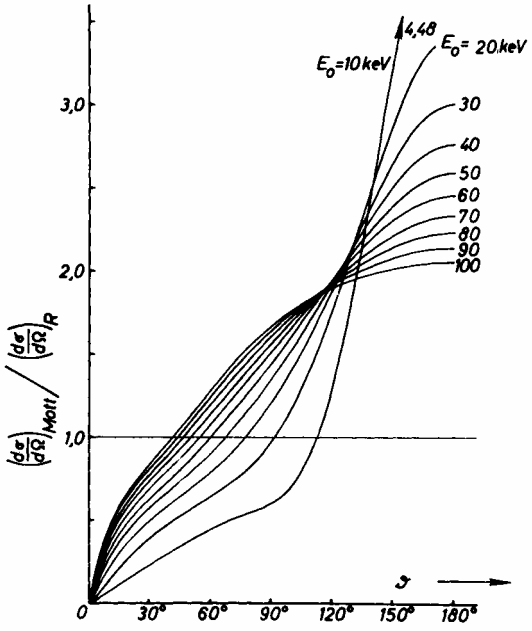

Figure 40: Ratio of Mott to Rutherford elastic scattering cross section (gold, bulk) [4,7]

Mass absorption coefficients also play an important role in the simulations, since they determine to a high degree the absorption behaviour during the interactions. CASINO uses the coefficient databases by Goldstein, modified by Pouchou and Pichoir (1991), containing the commonly used MACs by Henke and Ebisu.[3,78,79] One could discuss the validity of certain MACs, certainly for low-Z elements, but so far we have no knowledge of any better dataset. The sets by Heinrich and Henke and Ebisu are generally accepted as the most comprehensive so far.[6] If in the future it is advisable to use another set of values, it will be relatively easy to integrate it into CASINO.

With simulations programs, it is always important to check the basics behind the models. In our case, we adapted a relatively easy software package which was made public to the scientific world. The developers (Hovington, Drouin and Gauvin) have a website and forum on which recent updates, bug-fixes and developments are published, so that end-users can make the necessary changes in their own software. This partially guarantees a critical survey of the applied physics, with possibilities to keep our iterative model up-to-date.

3.2 Top-down evaluation and conclusions

After discussing all of the different uncertainties above, it is now time to see how good/bad the final result actually is. Suitable validity for a complete quantitative analytical procedure can be demonstrated by relative error distribution histograms for the analysis of standard particles of several chemical compounds. For testing our standardless iterative Monte Carlo quantification method, standard particles were prepared from pro analysis grade solid chemical compounds. The quantification method was evaluated by comparing the weight concentrations obtained from the measurements and calculations (C_c) with their nominal weight concentrations *(C_n)*. At least 10 independent analyses were performed for several types of standard particles (e.g. $CaCO_3$, KNO_3, SiO_2, NaCl, $CaSO_4.2H_2O$, $BaSO_4$, Fe_2O_3, $(NH_4)_2SO_4$ and NH_4NO_3) with their diameters varying between 0.5 and 5 μm. The results were summarized as a histogram of relative errors, expressed as: $\Delta = (C_c - C_n)/C_n$.

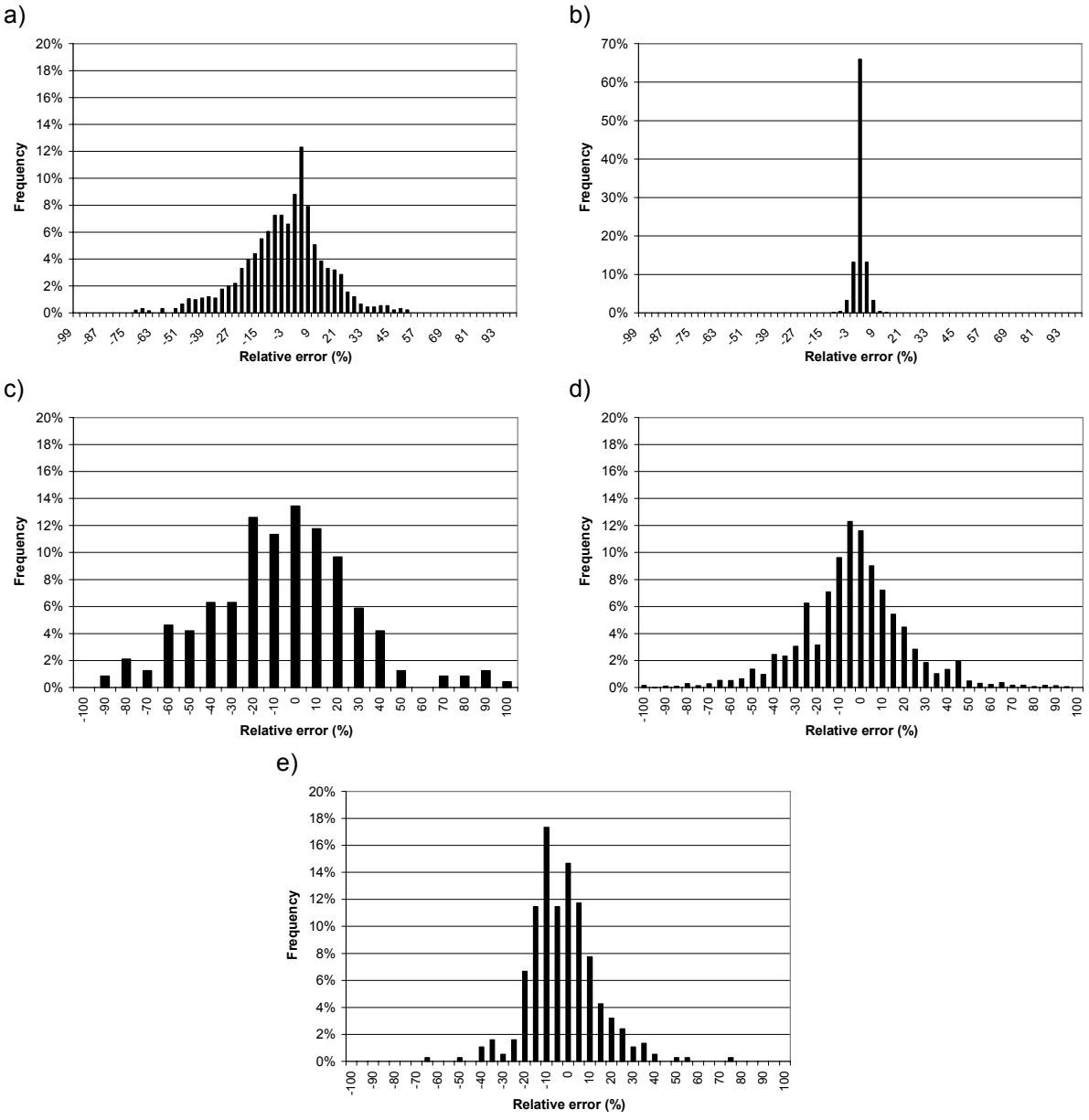

Figure 41: Relative error distributions for different quantification methods

It is also possible to compare the histograms of different methods in order to evaluate which procedures provide more accurate results. Our method was compared with a selection of other methods reported in literature. Figure 41 shows the comparison of the error distributions obtained for a) a classical bulk-standards *ZAF* method without particle corrections applied to particles, b) a standard particle-*ZAF* method applied to particles, c) a bulk-standards method without particle corrections applied to particles, d) a first-principles standardless method applied to bulk samples, e) our reverse Monte Carlo method for particles including light elements.

The first two graphs are based on data reported by Armstrong in 1982 and 1991.[21] He analyzed a large number of olivine particles, together with a pellet of the same material which he used as a bulk standard. He applied both a classical *ZAF* method and his own particle-*ZAF* method to demonstrate the importance of particle corrections. The difference between graphs a) and b) is quite obvious: the particle-*ZAF* method results in a very sharp peak of almost the entire set of analyses faling within ±10%, while the classical *ZAF* shows a bigger spread (±30%) due to the lack of particle corrections. It is important to point out that the reported experiment is not representative for real-life measurements of environmental particles. When we take samples of atmospheric particles, we do not have any pellets of the analyzed compounds at our disposal for use as bulk standards. In fact, we are not supposed to know in advance which compounds are present, so in some way the results reported by Armstrong do not tell us anything about the accuracy of particle-*ZAF* for environmental samples. We did not find any reports in literature about particle-*ZAF* experiments using bulk standard of different compounds than the analyzed standard particles, so we cannot determine the accuracy of the method under such conditions. However, Armstrong did clearly demonstrate that particle corrections do make sense! Laskin and Cowin reported the analysis of particles using a recent, commercial bulk-standard method without particle corrections in 2001.[50] Graph c) shows that 95% of the analyses lies in the ±50% interval, which is even worse than for the classical ZAF method in graph a). However, we must take into account our remark about the standard pellets, since Laskin and Cowin used 'real' bulk standards of materials that were not of the same composition as their samples. Laskin and Cowin analyzed their particles on TEM grids, which also explains the larger interval. In 1999, Newbury reported results from a method for the standardless analysis of bulk samples.[80] In graph d) we find the results of a first-principles method, in which the physical equations for electron-excited X-ray generation in the target, and X-ray absorption in the target and in other components of the spectrometer are used to predict the intensity from a pure element standard for each constituent under the analytical conditions in use (beam energy, beam incidence and X-ray take-off angles and detector solid angles). The sources of the relatively large relative error (95% of the analyses lies in the ±50% interval) are the uncertainties in the physical parameters (ionization cross section, mass absorption coefficients, fluorescence yield, detector parameters) and the fact that the sum of the concentrations must be forced to 100%. When light elements are not analyzed directly, i.e. they are not 'visible' and they are only taken into account based on stoichiometry, this normalization can introduce large errors.

The distribution of errors for the reverse Monte Carlo quantification for particle analysis in graph e) shows that semi-quantitative analysis is possible for a wide range of chemicals. The analytical precision of the method is within 5% relative, which is due to systematic errors for some of the compounds included (crystal water content can be different from the nominal value for hygroscopic particles, statistical error of the X-ray intensity determination originated from spectrum fitting procedure). The analytical accuracy is relatively high (95% of the analyses fall in the interval of ±30% relative error), taking into account the fact that also beam sensitive particles were included in the experiment. Over the past years a broad range of different compounds were analyzed, all with similar results.

As can be seen in the graphs, the performance of the reverse Monte Carlo method is superior to that of other first-principles standardless method, even though particles are analyzed using much worse counting statistics (10-20 s counting time vs. 100-500 s). It is also far better than the bulk-standard methods without particle corrections, which again indicates the importance of those corrections. Our conclusion that Monte Carlo simulations including geometric and matrix effects indeed provide quite accurate results for semi-quantitative particle analysis, was confirmed by other authors.[42] As all the elements except hydrogen can be detected, the normalization of the concentrations to 100 % is supported, so in this way the Monte Carlo method is even better than the particle-ZAF method reported by Armstrong. However, the accuracy of both methods is hard to compare, since we did not find any data that could confirm the performance of the particle-ZAF method using other bulk standards than pellets of the same composition as the samples.

References

[1] Castaign, R., *Applications de sondes électroniques à une methode d'analyse ponctuelle chimique et cristallographique*, Ph.D. thesis, Office National d'Études et Recherches Aerospatiales (1951)

[2] Grillon F. and J. Philibert, *The legacy of Raimond Castaign*, Mikrochim. Acta, 138, 99-104 (2002)

[3] Goldstein, J.I., D.E. Newbury, P. Echlin, D.C. Joy, A.D. Romig Jr., C.E. Lyman, C. Fiorgi and E. Lifshin, *Scanning Electron Microscopy and X-ray Microanalysis*, Plenum, New York (1992)

[4] Reimer, L., *Scanning Electron Microscopy: Physics of Image Formation and Microanalysis*, Springer, Berlin (1985)

[5] Lee, R.L., *Scanning Electron Microscopy and X-ray Microanalysis*, Prentice Hall, New Jersy (1993)

[6] Scott, V.D., G. Love and S.J.B. Reed, *Quantitative Electron-Probe Microanalysis*, Ellis Horwood, New York (1995)

[7] Joy, D.C., A.D. Romig Jr., J.I. Goldstein, *Principles of Analytical Electron Microscopy*, Plenum, New York (1986)

[8] Armstrong, J., *Quantitative electron microprobe analysis of airborne particulate material*, Ph.D. thesis, Arizona State University (1978)

[9] Small, J.A., D.E. Newbury and J.T. Armstrong in R. Van Grieken and A.A. Markowicz, *Handbook of X-Ray Spectrometry, Methods and Techniques*, Marcel Dekker, New York (2003)

[10] Packwood, R.H., and J.D. Brown, *A Gaussian expression to describe $\phi(\rho z)$ curves for quantitative electron probe microanalysis*, X-ray Spectrom., 10, 138-146 (1981)

[11] Brown, J.D., and R.H. Packwood, *Quantitative electron probe microalanysis using Gaussian $\phi(\rho z)$ curves*, X-ray Spectrom., 11, 187-193 (1982)

[12] Staub, P.-F., *IntriX: a numerical model for electron probe analysis at high depth resolution, Part I: theoretical description*, X-ray Spectrom., 27, 43-57 (1985)

[13] Bastin, G.F., F.J.J. van Loo and H.J.M. Heiligers, *Evaluation of the use of Gaussian curves in quantitative electron probe microanalysis: a new optimization*, X-ray Spectrom., 13, 91-97 (1984)

[14] Brown, J.D., *The application of depth distribution curves to quantitative electron probe microanalysis*, J. Anal. At. Spectrom., 14, 475478 (1999)

[15] Love, G., and V. Scott, *A critical appraisal of some recent correction procedures for quantitative electron-probe microanalysis*, J. Phys. D.: Appl. Phys., 13, 995-1004 (1980)

[16] Wernisch, J., *Quantitative electron microprobe analysis without standard samples*, X-ray Spectrom., 14, 109-119 (1985)

[17] Small, J.A. in R. Van Grieken and A.A. Markowicz, *Handbook of X-Ray Spectrometry, Methods and Techniques*, Marcel Dekker, New York (1993)

[18] Trincavelli, J., and R. Van Grieken, *Peak-to-bckground method for standardless electron microprobe analysis of particles*, X-ray Spectrom., 23, 254-260 (1994)

[19] Labár, J., and Sz. Török, *A peak-to-background method for electron microprobe analysis of particles applied to individual small particles*, X-ray Spectrom., 21, 183-190 (1992)

[20] Armstrong, J.T., and P.R. Buseck, *A general characteristic fluorescence correction for the quantitative electron microbeam analysis of thick specimens, thin films and particles*, X-ray Spectrom., 14, 172-182 (1985)

[21] Armstrong, J.T. in K.F.J. Heinrich and D.E. Newbury, *Electron probe quantitation*, Plenum, New York (1991)

[22] Armstrong, J.T., *CITZAF: a package of correction programs for the quantitative electron microbeam X-ray analysis of thick polished materials, thin films, and particles*, Microbeam Anal., 4, 177-200 (1995)
[23] Storms, H.M., K.H. Janssens, Sz.B. Török and R. Van Grieken, *Evaluation of the Armstrong-Buseck Correction for automated electron probe X-ray microanalysis of particles*, X-ray Spectrom., 18, 45-52 (1989)
[24] Van Borm, W.A., and F.C. Adams, *Standardless ZAF correction for semi-quantitative electron probe microanalysis of microscopical particles*, X-ray Spectrom., 20, 51-62 (1991)
[25] Trincavelli, J., G. Castellano and J.A. Riveros, *Model for the Bremsstrahlung spectrum in EPMA, Application to standardless quantification*, X-ray Spectrom., 27, 81-86 (1998)
[26] Zreiba, N.A., and T.F. Kelly, *X-ray depth distribution function for thin spheres*, X-ray Spectrom., 19, 275-283 (1990)
[27] Press, W.H., S.A. Teukolsky, W.T. Vetterling and B.P. Flannery, *Numerical recipes in C*, Cambridge University, Cambridge (1992)
[28] Joy, D.C., *An introduction to Monte Carlo simulations*, Scanning, 5, 329-337 (1991)
[29] Joy, D.C., *A database on electron-solid interactions*, Scanning, 17, 270-275 (1995)
[30] Lankosz, M., *Monte Carlo simulation of the matrix and geometrical effects in X-ray microfluorescence analysis of individual particles*, X-ray Spectrom., 21, 11-16 (1992)
[31] Llovet, X., E. Valovirta and E. Heikinheimo, *Monte Carlo simulation of secondary fluorescence in small particles and at phase boundaries*, Mikrochim. Acta, 132, 205-212 (2000)
[32] Castellano, G., S. Segui and J. Trincavelli, *Ionization depth distribution in EPMA: improvement of the random walk model*, X-ray Spectrom., 27, 293-298 (1998)
[33] Chan, A., and J.D. Brown, *Modifications to a multiple scattering Monte Carlo model to predict X-ray generation curves*, X-ray Spectrom., 26, 275-278 (1997)
[34] Hovington, P., D. Drouin and R. Gauvin, *CASINO: a new Monte Carlo code in C language for electron bam interactions – Part I: Description of the program*, Scanning, 19, 20-38 (1997)
[35] Drouin, D., P. Hovington and R. Gauvin, *CASINO: a new Monte Carlo code in C language for electron bam interactions – Part II: Tabulated values of the Mott cross section*, Scanning, 19, 20-38 (1997)
[36] Hovington, P., D. Drouin, R. Gauvin, D.C. Joy and N. Evans, *CASINO: a new Monte Carlo code in C language for electron bam interactions – Part III:stopping power at low energies*, Scanning, 19, 29-35 (1997)
[37] Gauvin, R., P. Hovington and D. Drouin, *Quantification of spherical inclusions in the scanning electron microscope using Monte Carlo simulations*, Scanning, 17, 202-219 (1995)
[38] Browning, R., T.Z. Li, B. Chul, Jun Ye, R.F.W. Pease, Z. Czy´zewski and D.C. Joy, *Emprical forms for the electron/atom elastic scattering cross sections from 0.1 to 30 keV*, J. Appl. Phys., 76, 20162022 (1994)
[39] Osán, J., I. Szalóki, C.-U. Ro and R. Van Grieken, *Light element analysis of individual microparticles using thin-window EPMA*, Mikrochim. Acta, 132, 349-355 (2000)
[40] Szalóki, I., J. Osán, C.-U. Ro and R. Van Grieken, *Quantitative characterization of individual aerosol particles by thin-window electron probe microanalysis combined with iterative simulation*, Spectrochim. Acta B, 55, 1017-1030 (2000)
[41] Ro, C.-U., J. Osán, I. Szalóki, J. de Hoog, A. Worobiec and R. Van Grieken, *A Monte Carlo program for quantitative electron-induced X-ray analysis of individual particles*, Anal. Chem., 75, 851-859 (2003)

[42] Li, Y., X. Liu, S. Dong, P. Van Espen and F. Adams, *Investigation on the geometric and matrix effects and quantitative determination of K, Cl and S atomic fraction for biomass burning particles by Monte Carlo simulaton*, Anal. Chim. Acta, 459, 93-106 (2002)
[43] Ro, C.-U., J. Osán and R. Van Grieken, *Determination of low-Z elements in individual environmental particles using windowless EPMA*, Anal. Chem., 71, 1521-1528 (1999)
[44] Wätjen, U., M. Kriews and W. Dannecker, *Status report: preparing an ambient aerosol filter reference material for elemental analysis*, Fresenius J. Anal. Chem., 345, 261-264 (1993)
[45] Berner, A., I. Levin, L. Klinger and D.G. Brandon, *Determination of the mean size of submicron particles by electron probe microanalysis*, X-ray Spectrom., 24, 13-18 (1995)
[46] Mitchell, J.P., *Particle standards: their development and application*, KONA Powder and Particle, 18, 3-14 (2002)
[47] Ro, C.-U., S. Hoornaert and R. Van Grieken, *Assessment of homogeneity of candidate reference material at the nanogram level and investigation on representativeness of single particle analysis using electron probe X-ray microanalysis*, Anal. Chim. Acta, 389, 151-160 (1999)
[48] Raeymakers, B., *Characterization of particles by automated electron probe microanalysis*, Ph.D. Theis, University of Antwerp (1986)
[49] Kramers H.A., *On the theory of X-ray absorption and of the continuous X-ray spectrum*, Philos. Mag., 46, 836-871 (1923)
[50] Laskin, A., and J.P. Cowin, *Automated single-particle SEM/EDX analysis of submicrometer particles down to 0.1 μm*, Anal. Chem., 73, 1023-1029 (2001)
[51] Windsor, E.S., D.E. Newbury and J.D. Kessler, *New boron substrates for particle microanalysis*, www.cstl.nist.gov/div837/Division/techac/2000/BoronSubstrateEPMA.htm
[52] Gregory, C.L., H.A. Nullens, R.H. Gijbels, P.J. Van Espen, I. Geuens, R. De Keyzer, *Automated particle analysis of populations of silver halide microcrystals by electron probe microanalysis under cryogenic conditions*, Anal. Chem., 70, 2551-2559 (1998)
[53] Worobiec, A., J. de Hoog, J. Osán, I. Salóki, C.-U. Ro and R. Van Grieken, *Thermal stability of beam sensitive atmospheric particles in electron probe microanalysis at liquid nitrogen temperature*, Spectrochim. Acta B, 58, 479-496 (2003)
[54] Wendt, M., The *role of contamination layers in electron probe microanalysis*, Kristall und Technik, 15, 1367-1375 (1980)
[55] Száloki, I., J. Osán, A. Worobiec, J. de Hoog and R. Van Grieken, *Optimisation of experimental conditions of thin-window EPMA for light element analysis of individual environmental particles*, X-ray Spectrom., 30, 143-155, 2001
[56] Worobiec A., *Optimization and application of different electron probe X-ray microanalysis techniques for the chemical characterization of individual environmental particles*, Ph.D. thesis, University of Antwerp (2004)
[57] Sullivan, N., T. Mai , S. Bowdoin and R. Vane, *A study of the effectiveness of the removal of hydrocarbon contamination by oxidative cleaning inside the SEM*, Microscopy and Microanalysis, 8-S2, 720 (2002)
[58] Procop, M., *Estimation of absorbing layer thicknesses for an Si-Li detector*, X-ray Spectrom., 28, 33-40 (1999)
[59] Schole, F., and G. Ulm, *Characterization of a windowless Si(Li) detector in the photon energy range 0.1-5 keV*, Nucl. Instr. Meth. Phys. Res., 339, 49-54 (1994)
[60] Garg, M.L., Jasbir Sigh, H.R. Verma and P.N. Trehan, *A modified theoretical model for the efficiency calculations of a Si(Li) detector)*, X-ray Spectrom., 16, 3-6 (1987)
[61] Hovington, P., G. L'Espérance, E. Baril and M. Rigaud, *Monitoring the performance of energy dispersive spectrometer detectors at low energy*, Scanning, 17, 136-139 (1995)

[62] Oxford Instruments Plc., *Instrumentaion for EDS*, Oxfordshire, UK (1999)
[63] Moxtek Inc., *Datasheet: ultra-thin soft X-ray window*, Utah, USA (1996)
[64] Osán, J., J. de Hoog, P. Van Espen, I. Szalóki, C.-U. Ro and R. Van Grieken, *Evaluation of energy-dispersive x-ray spectra of low-Z elements from electron-probe microanalysis of individual particles.,* X-Ray Spectrom., 30, 419-426 (2001)
[65] Duncumb, P., and P.J. Stratham, *Benefits of X-ray spectrum simulation at low energies*, Mikrochim. Acta, 138, 249-258 (2002)
[66] Coates, D.G., in P. Brederoo and V.E. Cosslett, *Electron Microscopy, Vol. 3, Analysis,* Electron Microscopy Foundation, Leiden (1980)
[67] Statham, P.J., in P. Brederoo and V.E. Cosslett, *Electron Microscopy, Vol. 3, Analysis,* Electron Microscopy Foundation, Leiden (1980)
[68] Van Espen, P., in R.E. Van Grieken and A.A. Markowicz, *Handbook of X-Ray Spectrometry, Methods and Techniques*, Marcel Dekker, New York (1993)
[69] Small, J.A., *The detection of low-intensity peaks in energy dispersive X-ray spectra from particles*, Scanning, 20**,** 92-98 (1998)
[70] Van Espen, P., K. Janssens and J. Nobels, *AXIL-PC, software for the analysis of complex X-ray spectra*, Chemom. Intell. Lab. Sys., 1, 109- 114 (1987)
[71] Vekemans, B., K. Janssens, L. Vincze, F. Adams and P. Van Espen, *Analysis of X-ray spectra by iterative least squares (AXIL): new developments*, X-Ray Spectrom., 23, 278-285 (1994)
[72] Van Espen, P., and P. Lemberge, *ED-XRF spectrum evaluation and quantitative analysis using multivariate and nonlinear techniques*, *Adv*. X-Ray Anal., 43, 560–569 (2000)
[73] Joy, D.C., C.S. Joy and R.D. Bunn, *Measuring the performance of scanning electron microscope detectors*, Scanning, 18, 533-538 (1996)
[74] Bethhe, H.A., *Zur Theorie des Durchgangs schneller Korpuskularstrahlen durch Materie*, Ann. Phys., 5, 325-400 (1930)
[75] Joy, D.C., and S. Luo, *An empirical stopping power relationship for low-energy electrons*, Scanning, 11, 176-180 (1989)
[76] Rutherford, E., *Elastic cross-section*, Phil. Mag., 21, 669-680 (1911)
[77] Czyzewski, Z., D.O. MacCullum, A. Romig and D.C. Joy, *Calculations of Mott scattering cross section*, J. Appl. Phys., 68, 7, 3066-3072 (1990)
[78] Pouchou, J.-L., and F. Pichoir in K.F.J. Heinrich and D.E. Newbury, *Electron probe quantification*, Plenum, New York (1991)
[79] Henke, B.L., and E.S. Ebisu, *Advances in X-ray analysis*, Plenum, New York (1974)
[80] Newbury, D.E., *Measures for spectral quality in low-voltage X-ray microanalysis*, Scanning, 22, 345-351 (2000)